



University of Concepción

Department of Electrical Engineering

Doctorate in Engineering Sciences with a major in Electrical Engineering

César Gallardo Sánchez

**DEVELOPMENT OF DESIGN TECHNIQUES TO  
OPTIMIZE THE PERFORMANCE OF SYNCHRONOUS  
RELUCTANCE MACHINES WITH ANISOTROPIC  
ROTOR STRUCTURE**

Thesis for the degree of Doctor of Science at the  
University of Concepcion, Concepción, Chile  
cgallardos@udec.cl

**Supervisor:** Professor Juan A. Tapia Ladino  
Department of Electrical Engineering  
University of Concepción, Concepción  
Chile

Professor Michele Degano  
Department of Electrical and Electronic Engineering  
University of Nottingham, Nottingham  
United Kingdom

January, 2024

© 2023 by [César Gallardo Sánchez](#) is licensed under [CC BY 4.0](#)



## Abstract

César Gallardo Sánchez

Title: *“Development of Design Techniques to optimize the performance of Synchronous Reluctance Machines with Anisotropic Rotor Structure”*

Concepción 2024

82 pages

This thesis provides a comprehensive understanding of Synchronous Reluctance Machines (SynRM), addressing both the fundamental principles of operation and the development of various design techniques. To expedite the sizing stage, a precise analytical model was developed which combines two methods: to calculate the air-gap flux density and average torque, the magnetic potential of the rotor and stator were used, and the torque ripple was calculated using the energy stored in the air-gap. This model is extended to machines with multiple flux barriers. Comparisons with the Finite Element Analysis (FEA) yield promising results, both in terms of air-gap flux density and electromagnetic torque. However, a harmonic analysis reveals that the analytical model tends to overestimate the air-gap flux density and torque due to underlying assumptions made during its development. Despite this, the model offers valuable capabilities, including the ability to extract machine parameters in the  $d-q$  reference frame, facilitating a preliminary control strategy analysis.

In pursuit of further enhancing SynRM performance, an asymmetric rotor topology was introduced. This feature achieves a significant reduction in torque ripple and an increase in maximum internal power factor. While both designs exhibit similar efficiency, the asymmetric design excels by offering a wider constant power speed range (CPSR). Simultaneously, a comprehensive study on discrete skew methodology was conducted. The proposed method provides deeper understandings into the impact of skew angle on torque ripple. This method introduces an indicator to assess the potential reduction achievable by selecting various skew steps and angles. Validation through FEA in both two and three dimensions reinforces its applicability.

These techniques were used to design two SynRMs using the same stator with two different rotor topologies, one symmetrical and the other asymmetrical. The design was carried out by optimization using a multi-objective genetic algorithm (MOGA), coupled with the techniques developed throughout the thesis. The preliminary results highlight the superiority of the asymmetric design in terms of performance indices. However, it is worth noting a significant reduction in these indices when skew is applied, underscoring the importance of design choices. These two rotor topologies were manufactured to validate the improvement through experimental measurements.

**Keywords:** analytical model, asymmetric rotor, design guidelines, electromagnetic torque, finite element analysis, step skew, saliency ratio, synchronous reluctance machine, tolerances.

## Acknowledgements

I would like to express my gratitude to my supervisors, Professor *Juan A. Tapia*, and Professor *Michele Degano*, for giving me the opportunity to work on this project. I have been collaborating with them since 2019, and I thank them for their support and guidance on some difficult tasks over these years.

I also want to thank the *LEME staff* for their valuable support, including *Carlos Madariaga* for his results discussions and invaluable help with reading and correcting my grammar in several papers.

I would like to offer my acknowledgements to the **PEMC group at The University of Nottingham** for their warm welcome at the time I stay there during my internship.

I am grateful to my *parents* and *family* for their love and sacrifice to support my education. I also appreciate the support of our friends here and at home.

I would like to express my love and gratitude to my wife, *Yenisley*, for her infinite support and patience during these challenging years. It was difficult being apart, but her courage and responsibility taught me how to be a better professional. I love you.

Lately, I would like to express my thanks to the **Agencia Nacional de Investigación y Desarrollo (ANID)** and the University of Concepcion for provided financial support for my studies in part by grant ANID-PFCHA/Doctorado Nacional/2020-21200527, project FONDECYT REGULAR 1230670, project FONDEF ID21I10099 and the Fondo de Internacionalización UCO 1866.

## CONTENTS

ABSTRACT .....	II
ACKNOWLEDGEMENTS .....	III
LIST OF FIGURES .....	VI
LIST OF TABLES.....	X
NOMENCLATURE AND ACRONYMS .....	XI
INTRODUCTION.....	1
I.    HYPOTHESIS.....	1
II.   OBJECTIVES.....	2
III.  OUTLINE OF THE DOCTORAL DISSERTATION .....	2
IV.  CONTRIBUTIONS OF THE DOCTORAL DISSERTATION .....	3
V.   LIST OF PUBLICATIONS AND FUNDINGS.....	3
CHAPTER I: SYNCHRONOUS RELUCTANCE MACHINE: AN OVERVIEW.....	5
1.1. OPERATING PRINCIPLE .....	5
1.2. ELECTROMAGNETIC TORQUE .....	6
1.3. INTERNAL POWER FACTOR AND POWER FACTOR .....	8
1.4. CONTROL STRATEGY .....	9
1.5. INFLUENCE OF SATURATION AND CROSS-COUPLING EFFECT .....	11
1.6. EFFICIENCY .....	13
1.7. DESIGN TECHNIQUES. MACHINE PERFORMANCE IMPROVEMENT .....	15
1.7.1. Analytical models vs. Finite elements methods .....	15
1.7.2. Rotor structure optimization employing asymmetries .....	16
1.7.3. Rotor skewing.....	17
1.8. SUMMARY .....	19
CHAPTER II: ACCURATE ANALYTICAL MODEL FOR SYNCHRONOUS RELUCTANCE MACHINE ..	20
2.1. MAIN ASSUMPTIONS .....	20
2.2. AIR-GAP FLUX DENSITY CALCULATION .....	21
2.3. TORQUE CALCULATION.....	24
2.4. EXTENSION OF THE METHOD TO MACHINES WITH A LARGER NUMBER OF FLUX BARRIERS PER POLE .....	28
2.5. PARAMETERS ON THE D-Q REFERENCE FRAME.....	32
2.6. SUMMARY .....	34
CHAPTER III: ROTOR ASYMMETRIC IMPACT ON SYNCHRONOUS RELUCTANCE MACHINE PERFORMANCE.....	35

<b>3.1. MODELLING OF THE SYNRRMS UNDER ANALYSIS .....</b>	<b>35</b>
3.1.1. Sizing method.....	35
3.1.2. Optimization process.....	36
3.1.3. Optimum Designs .....	38
<b>3.2. RESULTS ANALYSIS .....</b>	<b>39</b>
3.2.1. Saliency ratio.....	39
3.2.2. Maximum internal power factor .....	40
3.2.3. Electromagnetic torque.....	40
3.2.4. Torque ripple .....	41
3.2.5. Additional discussion on efficiency and CPSR .....	42
3.2.6. Sensitive analysis .....	44
<b>3.3. SUMMARY .....</b>	<b>45</b>
<b>CHAPTER IV: A METHOD TO DETERMINE THE TORQUE RIPPLE HARMONIC REDUCTION IN SKEWED SYNCHRONOUS RELUCTANCE MACHINES .....</b>	<b>46</b>
<b>4.1. SELECTED MACHINES.....</b>	<b>46</b>
<b>4.2. ANALYTICAL METHOD DERIVATION FOR DISCRETE SKEWING.....</b>	<b>47</b>
<b>4.3. FINITE ELEMENT VALIDATION: RESULTS AND DISCUSSION .....</b>	<b>49</b>
4.3.1. FEA evaluation original designs (skewless machines) .....	50
4.3.2. Evaluation of torque ripple reduction by means of two-step discrete skew .....	51
4.3.3. Evaluation of torque ripple reduction by means of three-step discrete skew .....	52
4.4.4. Evaluation of torque ripple reduction by means of four-step discrete skew.....	54
<b>4.4. COMPARISON, ANALYSIS, AND RECOMMENDATIONS .....</b>	<b>56</b>
<b>4.5. SUMMARY .....</b>	<b>58</b>
<b>CHAPTER V: PROPOSED DESIGN OF A SYNCHRONOUS RELUCTANCE MACHINE.....</b>	<b>59</b>
<b>5.1. SET-UP OF THE OPTIMIZATION PROCESS .....</b>	<b>59</b>
<b>5.2. RESULTS FROM THE OPTIMIZATION PROCESS .....</b>	<b>61</b>
<b>5.3. STRUCTURAL ANALYSIS .....</b>	<b>63</b>
<b>5.4. OPTIMAL DESIGN ADJUSTMENT.....</b>	<b>64</b>
<b>5.5. IMPACT OF ROTOR SKEWING ON THE PERFORMANCE OF THE MACHINE .....</b>	<b>75</b>
<b>5.6. MANUFACTURED PROTOTYPE .....</b>	<b>77</b>
<b>5.7. SUMMARY .....</b>	<b>78</b>
<b>6. CONCLUSIONS AND FUTURE WORK.....</b>	<b>80</b>
<b>6.1. CONCLUSION .....</b>	<b>80</b>
<b>6.2. FUTURE WORK.....</b>	<b>81</b>
<b>REFERENCES .....</b>	<b>82</b>

## List of Figures

- Figure 1.1.** Sketch representation of the reluctance principle. (a) isotropic object; (b) anisotropic object.
- Figure 1.2.** Sketch of a recent geometry for a 4-pole SynRM.
- Figure 1.3.** Phasor diagram for a SynRM at steady-state considering losses.
- Figure 1.4.** Influence of the current and load angle on the electromagnetic torque for a SynRM. (a) current angle vs. electromagnetic torque; (b) load angle vs. electromagnetic torque.
- Figure 1.5.** Influence of the current and load angle on the IPF for a SynRM. (a) current angle vs. power factor; (b) load angle vs. power factor.
- Figure 1.6.** Maximum power factor for a SynRM for different values of saliency ratio.
- Figure 1.7.** Behavior of the power factors in a six pole-three flux barriers SynRM analyzed through FEA.
- Figure 1.8.** Machine operating points under vector control techniques.
- Figure 1.9.** Influence of the current and the current angle on the machine inductances in a SynRM. (a) material with infinite permeability; (b) behavior of the material according to B-H curve; (c) M350-50A B-H curve; (d) mean flux density in the machine, six points were considered: barrier carrier, radial bridge, two points in the stator yoke and two in the teeth. The analysis was carried out in FEA.
- Figure 1.10.** Core loss distribution in a 6-pole SynRM for low speed and 5 A/mm<sup>2</sup>.
- Figure 1.11.** Influence of the current and load angles on the efficiency in a SynRM. (a) current angle vs. efficiency; (b) load angle vs. efficiency.
- Figure 1.12.** 3D sketch of different types of skew. (a) reference skewless rotor; (b) continuous skew; (c) discrete skew, also mentioned as step skew.
- Figure 2.1.** Sketch of a general rotor geometry for a SynRM.
- Figure 2.2.** Stator and rotor magnetic potential in the air-gap.
- Figure 2.3.** Flux barrier geometry and rotor magnetic potential in a rotor pole.
- Figure 2.4.** Magnetic potential and air-gap flux density without slotting effect for  $\theta_m = 0$ . (a) stator and rotor magnetic potential; (b) air-gap flux density.
- Figure 2.5.** Air-gap flux density with slotting effect for  $\theta_m = 0$ . (a) air-gap flux density waveform; (b) harmonic distribution of the air-gap flux density.
- Figure 2.6.** Electromagnetic torque waveform for two torque ripple periods with slotting effect. (a) torque waveform; (b) torque harmonic components.
- Figure 2.7.** Harmonic torque analysis when considering slotting effect for two torque ripple periods.
- Figure 2.8.** Electromagnetic torque waveform for two torque ripple periods with slotting effect. (a) torque waveform; (b) torque harmonic components.
- Figure 2.9.** Analytical method workflow.
- Figure 2.10.** Air-gap flux density waveform for  $\theta_m = 0$  for different rotor configuration and the harmonic components. (a, f) two barriers per pole; (b, g) three barriers per pole; (c, h) four barriers per pole; (d, i) five barriers per pole; (e, j) six barriers per pole torque ripple periods.
- Figure 2.11.** Electromagnetic torque waveform for different rotor configuration and the harmonic components. (a, f) two barriers per pole; (b, g) three barriers per pole; (c, h) four barriers per pole; (d, i) five barriers per pole; (e, j) six barriers per pole torque ripple periods.
- Figure 2.12.** Winding function for a four pole SynRM.
- Figure 2.13.** Flux linkage for a four pole SynRM. (a) flux linkage for the *abc* reference frame; (b) flux linkage for the *d-q* reference frame.
- Figure 3.1.** Machine topology. a) stator and rotor; b) rotor parametrization.
- Figure 3.2.** Optimization process workflow.
- Figure 3.3.** Designs obtained from the optimization process for a 4-pole machine with two flux barriers per pole. The current was fixed to ~10 A/mm<sup>2</sup> and the current angle was defined in the

optimization algorithm for MTPA. (a) symmetric design; (b) asymmetric design. The selected designs are highlighted on the figure.

- Figure 3.4.** Saliency ratio as a function of the current density and the current angle. (a) symmetric design counter-clockwise; (b) asymmetric design counter-clockwise; (c) symmetric design clockwise; (b) asymmetric design clockwise.
- Figure 3.5.** Internal power factor as a function of the current density and the current angle. (a) symmetric design counter-clockwise; (b) asymmetric design counter-clockwise; (c) symmetric design clockwise; (b) asymmetric design clockwise.
- Figure 3.6.** Electromagnetic torque as a function of the current density and the current angle. MTPA trajectory is highlighted in red. (a) symmetric design counter-clockwise; (b) asymmetric design counter-clockwise; (c) symmetric design clockwise; (b) asymmetric design clockwise.
- Figure 3.7.** Torque ripple as a function of the current density and the current angle. MTPA trajectory is highlighted in red. (a) symmetric design counter-clockwise; (b) asymmetric design counter-clockwise; (c) symmetric design clockwise; (b) asymmetric design clockwise.
- Figure 3.8.** Electromagnetic torque and power factor as a function of the current density and the current angle for counter-clockwise rotation. (a) asymmetric design; (b) symmetric design.
- Figure 3.9.** Efficiency map when the machine is operated a MTPA for a maximum current density of 5 A/mm<sup>2</sup> for counter-clockwise rotation. (a) symmetric design; (b) asymmetric design.
- Figure 3.10.** Percentage of contribution of each term to the global variance. Influence of barriers position and opening on torque ripple for both designs.
- Figure 4.1.** 3D sketches of (a) four-pole synchronous reluctance motor with two barriers per pole; (b) six-pole synchronous reluctance motor with two barriers per pole. Three-phase stator windings are highlighted in red, green, and blue, corresponding to each phase. Rotor in both machines is shown as an exploded view.
- Figure 4.2.** Schematics of the proposed methodology to calculate the skew angle  $\theta_{skew}$  to mitigate a selected harmonic of order  $w$ . 2 step and 3-step discrete skew are presented, although the method can be used for any number of slides.
- Figure 4.3.** Electromagnetic torque waveform and spectrum of skewless reference machine; (a) torque waveform of 4-pole machine with two barriers per pole; (b) torque spatial harmonic content of 4-pole machine with two barriers per pole; (c) torque waveform of 6-pole machine with two barriers per pole; (d) torque spatial harmonic content of 6-pole machine with two barriers per pole. Additionally, 2D and 3D simulation results are compared.
- Figure 4.4.** Comparison of electromagnetic torque waveform and harmonic content of skewless machine vs 2-step skewed machine; (a) torque waveform of 4-pole machine with two barriers per pole; (b) torque spatial harmonic content of 4-pole machine with two barriers per pole; (c) torque waveform of 6-pole machine with two barriers per pole; (d) torque spatial harmonic content of 6-pole machine with two barriers per pole. 2D and 3D simulation results are compared.
- Figure 4.5.** Comparison of electromagnetic torque waveform and harmonic content of skewless machine vs 3-step skewed machine; (a) torque waveform of 4-pole machine with two barriers per pole; (b) torque spatial harmonic content of 4-pole machine with two barriers per pole; (c) torque waveform of 6-pole machine with two barriers per pole; (d) torque spatial harmonic content of 6-pole machine with two barriers per pole. 2D and 3D simulation results are compared.
- Figure 4.6.** Comparison of electromagnetic torque waveform and harmonic content of skewless machine vs 4-step skewed machine; (a) torque waveform of 4-pole machine with two barriers per pole; (b) torque spatial harmonic content of 4-pole machine with two barriers per pole; (c) torque waveform of 6-pole machine with two barriers per pole; (d) torque spatial harmonic content of 6-pole machine with two barriers per pole. 2D and 3D simulation results are compared.



- Figure 4.7.** Flux density distribution in a 6-pole machine with two barriers per pole for  $J=10$  A/mm<sup>2</sup> and  $\theta_{r,e}=0$ . (a) skewless machine; (b) 2-step skew machine; (c) 3-step skew machine; (d) 4-step skew machine.
- Figure 5.1.** Sketch of the rotor of a SynRM with three flux barriers per pole. The parameters subject to optimization are properly defined on both sides of the  $q$ -axis of the rotor.
- Figure 5.2.** Designs obtained from the optimization process for a 4-pole machine with three flux barriers per pole. The current was fixed to  $\sim 20$  A/mm<sup>2</sup> and the current angle was defined in the optimization algorithm for MTPA. (a) symmetric design; (b) asymmetric design. The selected designs are highlighted on the figure.
- Figure 5.3.** Designs obtained from the optimization process for a 6-pole machine with three flux barriers per pole. The current was fixed to  $\sim 20$  A/mm<sup>2</sup> and the current angle was defined in the optimization algorithm for MTPA. (a) symmetric design; (b) asymmetric design. The selected designs are highlighted on the figure.
- Figure 5.4.** Behavior of the average torque and torque ripple in the symmetrical design for different radii of the duct located in the first rotor island when  $\alpha_i^e = 60^\circ$  elect. degree. (a) average torque; (b) torque ripple.
- Figure 5.5.** Behavior of the average torque and torque ripple in the symmetrical design for different radii of the duct located in the first rotor island when  $\alpha_i^e = 60^\circ$  elect. degree. (a) average torque; (b) torque ripple.
- Figure 5.6.** Von Mises stress distribution for the optimal designs at 10,000 rpm. (a) symmetric design; (b) asymmetric design. Graphical results are magnified  $\times 10$  for easy viewing.
- Figure 5.7.** Total deformation distribution for the optimal designs at 10,000 rpm. (a) symmetric design; (b) asymmetric design. Graphical results are magnified  $\times 10$  for easy viewing.
- Figure 5.8.** Saliency ratio for the symmetric and asymmetric design. (a) symmetric design counter-clockwise rotation; (b) asymmetric design counter-clockwise rotation; (c) symmetric design clockwise rotation; (b) asymmetric design clockwise rotation.
- Figure 5.9.** Internal power factor for the symmetric and asymmetric design. (a) symmetric design counter-clockwise rotation; (b) asymmetric design counter-clockwise rotation; (c) symmetric design clockwise rotation; (b) asymmetric design clockwise rotation.
- Figure 5.10.** Torque ripple for the symmetric and asymmetric design. (a) symmetric design counter-clockwise rotation; (b) asymmetric design counter-clockwise rotation; (c) symmetric design clockwise rotation; (b) asymmetric design clockwise rotation.
- Figure 5.11.** Mean torque for the symmetric and asymmetric design. (a) symmetric design counter-clockwise rotation; (b) asymmetric design counter-clockwise rotation; (c) symmetric design clockwise rotation; (b) asymmetric design clockwise rotation.
- Figure 5.12.** Harmonic components of the electromagnetic torque for the optimum symmetric and asymmetric design counter-clockwise rotation; (a) current density 5 A/mm<sup>2</sup>; (b) current density 7.5 A/mm<sup>2</sup>; (c) current density 10 A/mm<sup>2</sup>; (d) current density 12.5 A/mm<sup>2</sup>; (e) current density 15 A/mm<sup>2</sup>.
- Figure 5.13.** Harmonic components of the electromagnetic torque for the optimum symmetric and asymmetric design clockwise rotation; (a) current density 5 A/mm<sup>2</sup>; (b) current density 7.5 A/mm<sup>2</sup>; (c) current density 10 A/mm<sup>2</sup>; (d) current density 12.5 A/mm<sup>2</sup>; (e) current density 15 A/mm<sup>2</sup>.
- Figure 5.14.** Harmonic components of the electromagnetic torque for the optimum symmetric and asymmetric design applying four step skew and counter-clockwise rotation; (a) current density 5 A/mm<sup>2</sup>; (b) current density 7.5 A/mm<sup>2</sup>; (c) current density 10 A/mm<sup>2</sup>; (d) current density 12.5 A/mm<sup>2</sup>; (e) current density 15 A/mm<sup>2</sup>.
- Figure 5.15.** Harmonic components of the electromagnetic torque for the optimum symmetric and asymmetric design applying four step skew and clockwise rotation; (a) current density 5

A/mm<sup>2</sup>; (b) current density 7.5 A/mm<sup>2</sup>; (c) current density 10 A/mm<sup>2</sup>; (d) current density 12.5 A/mm<sup>2</sup>; (e) current density 15 A/mm<sup>2</sup>.

- Figure 5.16.** Saliency ratio for the symmetric and asymmetric design with four step skew is applied. (a) symmetric design counter-clockwise rotation; (b) asymmetric design counter-clockwise rotation; (c) symmetric design clockwise rotation; (b) asymmetric design clockwise rotation.
- Figure 5.17.** Internal power factor for the symmetric and asymmetric design with four step skew is applied. (a) symmetric design counter-clockwise rotation; (b) asymmetric design counter-clockwise rotation; (c) symmetric design clockwise rotation; (b) asymmetric design clockwise rotation.
- Figure 5.18.** Torque ripple for the symmetric and asymmetric design with four step skew is applied. (a) symmetric design counter-clockwise rotation; (b) asymmetric design counter-clockwise rotation; (c) symmetric design clockwise rotation; (b) asymmetric design clockwise rotation.
- Figure 5.19.** Mean torque for the symmetric and asymmetric design with four step skew is applied. (a) symmetric design counter-clockwise rotation; (b) asymmetric design counter-clockwise rotation; (c) symmetric design clockwise rotation; (b) asymmetric design clockwise rotation.
- Figure 5.20.** Superposition of the contour curves of the main performance indices over a certain range of current density and current angle with counter-clockwise rotation. Two operating points were defined for MTPA for 7.5 A/mm<sup>2</sup> and 10 A/mm<sup>2</sup>. (a) symmetric design; (b) asymmetric design.
- Figure 5.21.** Superposition of the contour curves of the main performance indices over a certain range of current density and current angle with clockwise rotation. Two operating points were defined for MTPA for 7.5 A/mm<sup>2</sup> and 10 A/mm<sup>2</sup>. (a) symmetric design; (b) asymmetric design.
- Figure 5.22.** Symmetric and asymmetric design electromagnetic torque waveform for MTPA when the current density is 7.5 A/mm<sup>2</sup> and 10 A/mm<sup>2</sup> and the machine rotated counter-clockwise. (a) skewless designs; (b) 5-step skew designs.
- Figure 5.23.** Magnetic flux density distribution for the optimal designs for MTPA at 7.5 A/mm<sup>2</sup>. (a) symmetric design counter-clockwise rotation; (b) asymmetric design counter-clockwise rotation.
- Figure 5.24.** Magnetic flux density distribution for the optimal design for MTPA at 10 A/mm<sup>2</sup>. (a) symmetric design counter-clockwise rotation; (b) asymmetric design counter-clockwise rotation.
- Figure 5.25.** Performance indices for the symmetric design for MTPA for different current density levels. (a) current angle; (b) saliency ratio; (c) maximum internal power factor; (d) average torque; (e) torque ripple; (f) efficiency.
- Figure 5.26.** Performance indices for the asymmetric design for MTPA for different current density levels. (a) current angle; (b) saliency ratio; (c) maximum internal power factor; (d) average torque; (e) torque ripple; (f) efficiency.
- Figure 5.27.** CPSR performance for the symmetric and asymmetric design for maximum current density of 10A/mm<sup>2</sup>. (a) torque vs. speed for the symmetric design; (b) power vs. speed for the symmetric design; (c) torque vs. speed for the asymmetric design; (d) power vs. speed for the asymmetric design.
- Figure 5.28.** Efficiency map when the machine is operated a MTPA for a maximum current density of 10A/mm<sup>2</sup>. (a) skewless symmetric design; (b) skewless asymmetric design; (c) 5-step skew symmetric design; (d) 5-step skew asymmetric design.
- Figure 5.29.** Exploded view of the motor assembly. (a) asymmetric rotor; (b) asymmetric rotor; (c) stator lamination and winding assembled in the housing (jacket water); (d) shaft.

## List of tables

<b>Table 1.1.</b>	Output parameters for a case study 6-pole SynRM through FEA.
<b>Table 2.1.</b>	Machine main parameters.
<b>Table 2.2.</b>	Average torque and torque ripple values for harmonic analysis.
<b>Table 2.3.</b>	Average torque and torque ripple for different rotor configurations.
<b>Table 2.4.</b>	Mean torque comparison between FEM and AM.
<b>Table 3.1.</b>	Design parameters
<b>Table 3.2.</b>	Input variables range.
<b>Table 3.3.</b>	Geometric values for optimal symmetrical and asymmetrical designs.
<b>Table 3.4.</b>	Performance indices for the operating points defined in Figure 3.8 and Figure 3.9 for the symmetrical and asymmetrical designs when the machine rotated counter-clockwise.
<b>Table 4.1.</b>	Main data of the selected machines.
<b>Table 4.2.</b>	Skew angle to reduce a specific electromagnetic torque harmonic order by discrete skew.
<b>Table 4.3.</b>	Torque ripple harmonic component reduction as a result of 2-step skewing. 3D results are considered, and relevant harmonic components are analyzed.
<b>Table 4.4.</b>	Average torque and torque ripple comparison when applying 2-step skewing, by means of 2D and 3D FEA simulations.
<b>Table 4.5.</b>	Torque ripple harmonic component reduction as a result of 3-step skewing. 3D results are considered and relevant harmonic components are analyzed.
<b>Table 4.6.</b>	Average torque and torque ripple comparison when applying 3-step skewing, by means of 2D and 3D FEA simulations.
<b>Table 4.7.</b>	Torque ripple harmonic component reduction as a result of 3-step skewing. 3D results are considered and relevant harmonic components are analyzed.
<b>Table 4.8.</b>	Average torque and torque ripple comparison when applying 4-step skewing, by means of 2D and 3D FEA simulations.
<b>Table 5.1.</b>	Main data of the machine subject to optimization.
<b>Table 5.2.</b>	Objective function for the optimization process.
<b>Table 5.3.</b>	Input variables range for the optimization process for 4-pole and 6-pole SynRM.
<b>Table 5.4.</b>	Skew angle to reduce a specific harmonic component of the electromagnetic torque.
<b>Table 5.5.</b>	Value of the mitigation factor when the first harmonic component is selected to reduce ( $w = 6$ ).
<b>Table 5.6.</b>	Value of the mitigation factor when the second harmonic component is selected to reduce ( $w = 12$ ).
<b>Table 5.7.</b>	Value of the mitigation factor when the third harmonic component is selected to reduce ( $w = 18$ ).
<b>Table 5.8.</b>	Performance indices for the operating points defined in Figure 6.20 for the symmetrical and asymmetrical designs when the machine rotated counter-clockwise.
<b>Table 5.9.</b>	Performance indices for the operating points defined in Figure 6.21 for the symmetrical and asymmetrical designs when the machine rotated clockwise.

## Nomenclature and acronyms

### *Latin alphabet*

$B_g$	Flux density in the air-gap
$b_{ss}$	Slot opening
$b_t$	Tooth width
$D_{ri}$	Rotor inner diameter
$D_{ro}$	Rotor outer diameter
$D_{si}$	Stator inner diameter
$D_{so}$	Stator outer diameter
$g$	Air-gap length
$g_r$	Air-gap function
$h_t$	Tooth height
$i_d$	$d$ -axis current
$i_q$	$q$ -axis current
$I_{rms}$	Supply current
$i_s$	Stator current
$J$	Current Density
$k_{air}$	Insulation ratio
$K_p$	Ratio between the barrier angles
$k_{rs,v}$	Skew mitigation factor for harmonic $v$
$K_s$	Electric loading
$k_w$	Winding factor
$K_w$	Ratio between the barrier opening angles
$l_{axial}$	Axial length
$L_{aa}$	$a$ -phase self-inductance
$L_{ac}$	$a$ -phase and $c$ -phase mutual-inductance
$L_{ab}$	$a$ -phase and $b$ -phase mutual-inductance
$L_{bb}$	$b$ -phase self-inductance
$L_{ba}$	$b$ -phase and $a$ -phase mutual-inductance
$L_{bc}$	$b$ -phase and $c$ -phase mutual-inductance
$L_{cc}$	$c$ -phase self-inductance
$L_{ca}$	$c$ -phase and $a$ -phase mutual-inductance
$L_{cb}$	$c$ -phase and $b$ -phase mutual-inductance
$L_d$	$d$ -axis self-inductance
$L_q$	$q$ -axis self-inductance
$L_{dq}$	$d$ -axis and $q$ -axis mutual-inductance
$L_{qd}$	$q$ -axis and $d$ -axis mutual-inductance
$l_{st}$	Stack length
$m$	Number of phases
$N_i$	Winding Function for " $i$ " phase
$N_s$	Turns per slot
$N_t$	Turns per pole per phase
$P$	Air-gap permeance
$p$	Pole pair
$P_{cu}$	Joule losses
$P_{edd+hys+add}$	Core losses (eddy-current, hysteresis and additional)
$q$	Number of slots

$R$	Air-gap radius
$\mathcal{R}_b$	Reluctance
$R_s$	Stator resistance
$T_{\text{avg}}$	Mean torque
$T_{\text{em}}$	Electromagnetic torque
$T_{\text{rp}}$	Torque ripple
$U_s$	Stator magnetic potential
$U_r$	Rotor magnetic potential
$v_d$	$d$ -axis voltage
$v_q$	$q$ -axis voltage
$v_s$	Stator voltage
$W_b$	Energy stored in the flux barrier
$W_g$	Energy stored in the air-gap
$W_m$	Magnetic energy

### ***Greek alphabet***

$\alpha_i^e$	Current angle
$\delta$	Load angle
$\theta_s$	Position along the stator periphery
$\theta_{\text{skew}}$	Skew angle
$\theta_m$	Rotor periphery
$\theta_r$	Rotor position
$\theta_s$	Stator periphery
$\lambda_d$	$d$ -axis flux linkage
$\lambda_q$	$q$ -axis flux linkage
$\lambda_i$	Flux linkage for “ $i$ ” phase
$\mu_0$	Air permeability
$\xi$	Saliency ratio
$\tau_p$	Polar pitch
$\tau_s$	Slot pitch
$\emptyset_b$	Magnetic flux
$\omega$	Electrical speed

### ***Abbreviations***

2D	Two-dimensional
3D	Three-dimensional
AM	Analytical Model
CF	Constant Flux
CPSR	Constant Power Speed Region
DC	Direct Current Machine
FEA	Finite Element Analysis
FEM	Finite Element Method
FW	Flux Weakening
IPF	Internal Power Factor
IPF <sub>max</sub>	Maximum Internal Power Factor
IM	Inductor Machine
IPM	Interior Permanent Magnet Machine
MMF	Magnetic Motive Force
MOGA	Multi-Objective Genetic Algorithm
MTPA	Maximum Torque per Ampere
MTPV	Maximum Torque per Volt

PM	Permanent Magnet
PMa-SynRM	Permanent Magnet assisted Synchronous Reluctance Machine
PMSM	Permanent Magnet Synchronous Machine
SRM	Swishes Reluctance Machine
SynRM	Synchronous Reluctance Machine

## Introduction

Interest in Synchronous Reluctance Machines (SynRMs) is growing due to their many advantages over other machine types. SynRMs are single-excited machines that offer acceptable torque density [1], [2], high efficiency [3], [4], high-speed suitability [5], [6], fault tolerance capability [7], [8], and low cost [9], [10]. This makes them a promising alternative to induction machines (IM) [10] and permanent magnet synchronous machines (PMSM) [9], [10]. The absence of rotor windings or rotor cage in SynRMs eliminates rotor ohmic losses, leading to lower temperature and higher efficiency compared to IMs [11]. In addition, the absence of permanent magnets (PMs) simplifies the manufacturing process and reduces the cost compared to PMSMs.

SynRMs are used in various applications and are emerging as a substitute for induction motors in industry. However, their use is also beginning to be studied in the field of vehicle electrification. Nevertheless, these comparative advantages come at the cost of two critical drawbacks: high torque ripple [12], [13] and low power factor [9], [13]. One of the main contributors for the large torque ripple in SynRM is the interaction of spatial harmonics of the magnetic motive force (MMF) generated by stator currents and rotor geometry [14]. High torque ripple can lead to undesired mechanical vibrations and potential acoustic noise, as well as impact the current harmonics. Moreover, in high-performance applications, low torque ripple is strictly required [15] and, consequently, different techniques have been developed to reduce its magnitude as much as possible such as: (i) modify and optimize the winding configuration [15], [16], and (ii) optimize the rotor structure, in terms of geometry and dimensions [17], [18]; i.e.: using skewed rotor, adopting two different flux-barrier geometries in the same lamination and asymmetries rotor structures.

Despite these two drawbacks, SynRMs have continued to attract interest for two main reasons: (i) the increasing cost of rare earth permanent magnets and (ii) the increasing demand for high-efficiency motors. However, considering the main requirements of different applications, these machines topology are under intense research and development work at the moment. This work aims to further the research and development of SynRM by developing new design techniques. The work will focus on modifying the rotor structure by incorporating asymmetrical flux barriers and see how these modify the performance of the machine. Other modifications to the rotor were also evaluated to reduce the torque ripple, such as a detailed skew technique. An accurate analytical model will be developed for a fast-sizing stage which incorporate the slotting effect in the torque waveform. The studies carried out will serve as design guidelines for SynRM, reducing design times and improving machine performance.

### I. Hypothesis

The hypothesis that was tested during this doctoral thesis is:

*An asymmetric rotor structure, which features a different position of the flux barriers relative to the rotor's  $q$ -axis, in a Synchronous Reluctance Machine can increase magnetic anisotropy in the rotor structure. This improvement enables an increase in saliency ratio, power factor, efficiency, and average torque, while also reducing torque ripple in the machine operation.*

## II. Objectives

### *General objective:*

- ❖ Enhance the performance of Synchronous Reluctance Machines through the development of design techniques and guidelines focused on increasing rotor anisotropy.

### *Specific objectives:*

1. Develop and validate an accurate analytical model for Synchronous Reluctance Machines.
2. Investigate the impact of rotor asymmetries on the performance of Synchronous Reluctance Machines
3. Analyze and compare the performance of Synchronous Reluctance Machines with enhanced rotor anisotropy by including asymmetries against traditional designs under various operating conditions.
4. Validate the practical feasibility of the optimized Synchronous Reluctance Machines designs with rotor asymmetries through Finite Element Analysis and experimental testing and validation.

## III. Outline of the doctoral dissertation

This doctoral dissertation focuses on the different design techniques for SynRM we put some efforts in apply some asymmetric features on the rotor structure.

- **Chapter I** provides a brief overview of the basic theory, development history, model, vector diagram, and main characteristics of the SynRM. The non-linear behavior is also discussed. The chapter concludes by discussing the different design technique to improve the performance of SynRM.

- **Chapter II** presents the linear analytical model of SynRM with multiples flux barriers per rotor pole and the slotting effect is take into account. This model is based on equivalent lumped-parameter magnetic network and aims to compute stator and rotor magnetic potential, air-gap flux density and electromagnetic torque.

- **Chapter III** explores the benefits of asymmetrical rotor geometry. It analyzes various performance indices across a range of operating points. The behavior of the machine is compared between a symmetrical model and an asymmetrical model, both optimized through Finite Element Method (FEM).

- **Chapter IV** introduces a generalized analytical expression for multi-step discrete skewing in SynRM, examining its impact on torque harmonic components. It introduces a method to visualize how to reduce specific harmonic content. Two SynRM designs are analyzed through finite element analysis to compare the effectiveness of each approach and validate the optimal step skewing predicted by the analytical formulation.

- **Chapter V** employs the methods discussed throughout the manuscript to design a SynRM prototype through optimization using genetic algorithms and FEM simulations. The optimization results in two designs, a symmetrical one and an asymmetrical one, which are compared in terms of average torque, torque ripple, saliency ratio, and power factor. The optimal designs go through further evaluation from a mechanical standpoint to ensure the rotor integrity.



#### IV. *Contributions of the doctoral dissertation*

The specific contributions of this Thesis are summarized as follows:

##### ***The Main Contribution of Chapter II***

Development a fast and accurate analytical model to determine the air-gap flux density distribution and the torque waveform for different combination of pole/barrier and take into account the slotting effect.

Provide the equations to obtain from the air-gap flux density the flux linkages in the  $q-d$  reference frame.

##### ***The Main Contribution of Chapter III***

A comprehensive study on the influence of the benefits and disadvantages of applying asymmetries in the rotor structure of a SynRM for different operating points.

##### ***The Main Contribution of Chapter IV***

Present a comprehensive analytical expression for multi-step discrete skewing in SynRM.

The method calculates a specific skew angle to eliminate a specific harmonic component and a mitigation factor to showcase the impact of skewing on each harmonic component.

##### ***The Main Contribution of Chapter V***

Design and manufacturing of 24kW prototype with two different rotors (symmetric and asymmetric) for laboratory level examinations in order to validate the design methods at University of Nottingham.

#### V. *List of publications and fundings*

This doctoral dissertation contains material from the following papers.

##### ***Journal publications***

- ❖ **C. Gallardo**, J. A. Tapia, M. Degano and H. Mahmoud, "Accurate Analytical Model for Synchronous Reluctance Machine With Multiple Flux Barriers Considering the Slotting Effect," in *IEEE Transactions on Magnetics*, vol. 58, no. 9, pp. 1-9, Sept. 2022, Art no. 8107709.
- ❖ **C. Gallardo**, C. Madariaga, J. A. Tapia, and M. Degano, "A Method to Determine the Torque Ripple Harmonic Reduction in Skewed Synchronous Reluctance Machines," *Applied Sciences* 2023, vol. 13, no. 5, pp. 2949, Feb. 2023.
- ❖ C. Madariaga, **C. Gallardo**, J. A. Tapia, W. Jara, A. Escobar, and M. Degano, "Fast Assessment of Rotor Barrier Dimensional Allowances in Synchronous Reluctance Machines," in *IEEE Access*, vol. 11, pp. 58349-58358, 2023.
- ❖ C. Madariaga, **C. Gallardo**, N. Reyes, J. A. Tapia, W. Jara, and M. Degano, "Design and Evaluation of Matrix Rotor Induction Motor for High-Torque Low-Speed Applications," in *IEEE Transactions on Energy Conversion*, *under review*.

##### ***Conference publications***

- ❖ **C. Gallardo**, J. A. Tapia, M. Degano, H. Mahmoud and A. E. Hoffer, "*Rotor Asymmetry Impact on Synchronous Reluctance Machines Performance*," 2022 International Conference on Electrical Machines (ICEM), pp. 848-854, 2022.
- ❖ **C. Gallardo**, C. Madariaga, V. Rodriguez-Merchan and J. A. Tapia, "*Comparative Analysis of a Synchronous Reluctance and a Solid-Rotor Induction Machine for High-Speed Applications*," 2022 IEEE ANDESCON, 2022.
- ❖ **C. Gallardo**, C. Madariaga, J. A. Tapia and M. Degano "*Effects of Rotor Asymmetries on d-q Axis Parameters in Synchronous Reluctance Machines*," 2023 IEEE International Electric Machines & Drives Conference (IEMDC), San Francisco, CA, USA, 2023.
- ❖ C. Madariaga, **C. Gallardo**, J. A. Tapia, W. Jara and D. Riquelme, "*Quick Comparison of the Cogging Torque Severity in Permanent Magnet Synchronous Machines with Segmented Stator Core*," 2022 IEEE International Conference on Automation/XXV Congress of the Chilean Association of Automatic Control (ICA-ACCA), 2022.
- ❖ F. Ortiz, **C. Gallardo**, C. Madariaga and J. A. Tapia "*Design and Evaluation of Axial-Flux Permanent Magnet Machine with Enhanced Saliency*," 2023 IEEE International Electric Machines & Drives Conference (IEMDC), San Francisco, CA, USA, 2023.
- ❖ N. Reyes, M. Jiménez, A. Hoffer, C. Madariaga, **C. Gallardo**, J. A. Tapia, W. Jara, A. Escobar, and M. Degano, "*Structural Feasibility and Electromagnetic Analysis of an Ironless Rotor Axial Flux Permanent Magnet Synchronous Machine*," 2023 IEEE Energy Conversion Congress and Exposition (ECCE), Nashville, TN, USA, 2023.
- ❖ **C. Gallardo**, C. Madariaga, J. A. Tapia and M. Degano "*Impact of Rotor Step Skew on the Performance of Synchronous Reluctance Machines*," 2023 IEEE CHILEAN Conference on Electrical, Electronics Engineering, Information and Communication Technologies, Valdivia, Chile, 2023.
- ❖ C. Madariaga, **C. Gallardo**, J. A. Tapia, W. Jara, N. Reyes and F. Santacruz "*Comparison of Matrix-Rotor Induction Motor and Permanent Magnet Machine for Low-Speed High-Torque Applications*," 2023 IEEE CHILEAN Conference on Electrical, Electronics Engineering, Information and Communication Technologies, Valdivia, Chile, 2023.
- ❖ F. Santacruz, C. Madariaga, **C. Gallardo** and J. A. Tapia "*Electromagnetic Sizing Validation of Double Cage Induction Motor for Electric Vehicles Using Finite Element Simulation*," 2023 IEEE CHILEAN Conference on Electrical, Electronics Engineering, Information and Communication Technologies, Valdivia, Chile, 2023.

### *Fundings*

- ❖ Fondo de Internacionalización UCO 1866, University of Concepcion.
- ❖ ANID-PFCHA/Doctorado Nacional/2020-21200527.
- ❖ VIU23P0053, "*Diseño de máquinas eléctricas para aplicaciones industriales: software de análisis y simulación para la formación de competencias profesionales*"

## Chapter I: Synchronous Reluctance Machine: an overview.

This chapter introduces an overview of the basic principles of operation for SynRMs. It covers the mathematical model and includes the saturation and cross-coupling effect between the  $d$ - $q$  axes. Additionally, several design techniques that play a major role in improving performance during the SynRM design phase are highlighted.

### 1.1. Operating principle

The first theoretical and technical introduction of a motor with reluctance torque production and sinusoidal MMF using a conventional IM stator was made by Kostko in 1923 [19]. This led over the years to the concept of a SynRM evolving from a simple rotor structure to more complex design structures. However, it was not until the 1990s that it was demonstrated that the SynRM can be controlled using vector control techniques [20]–[23] and thus improve its performance, making this machine topology more attractive.

SynRMs develop electromagnetic torque on the shaft based on the variation of the reluctance. In Figure 1.1 the object (a) has the same geometrical dimensions in all axes, so it is isotropic, when exposed to a magnetic field it has the same reluctance in all axes. Then, the object (b) in Figure 1.1 has different dimensions in the axes (anisotropic), so when exposed to the same magnetic field a reluctance difference appears its axes. As a result, an electromagnetic torque develops in the object (b) which tends to align the  $d$ -axis to the position of less reluctance; this torque will be present as long as there is an angular difference between the  $d$ -axis and the magnetic field to which the object is exposed. The angle between the  $d$ -axis and the magnetic field produced by the stator is known as the load angle ( $\delta$ ). The stator current is responsible for both magnetization (main field) and torque production [21].

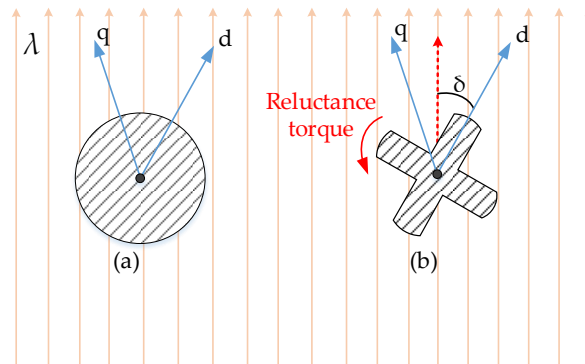


**Figure 1.1.** Sketch representation of the reluctance principle. (a) isotropic object; (b) anisotropic object.

In general, the SynRM is similar to the conventional salient-pole synchronous motor, but it does not have an excitation winding in the rotor structure. The SynRM rotor is composed of flux carriers (electrical steel) and flux barriers (insulating material, usually air), as shown in Figure 1.2. The main advantage of the SynRM lies in the absence of copper losses in the rotor, which allows a higher continuous torque than other IMs of the same size [24], [25]. To meet these requirements, the rotor geometry of a SynRM must be designed so that the inductance on the  $d$ -axis is maximum and minimum on the  $q$ -axis. This ratio between the  $d$ -axis and  $q$ -axis inductances is known as the *saliency ratio* ( $\xi$ ) and is calculated as

$$\xi = \frac{L_d}{L_q}. \quad (1.1)$$

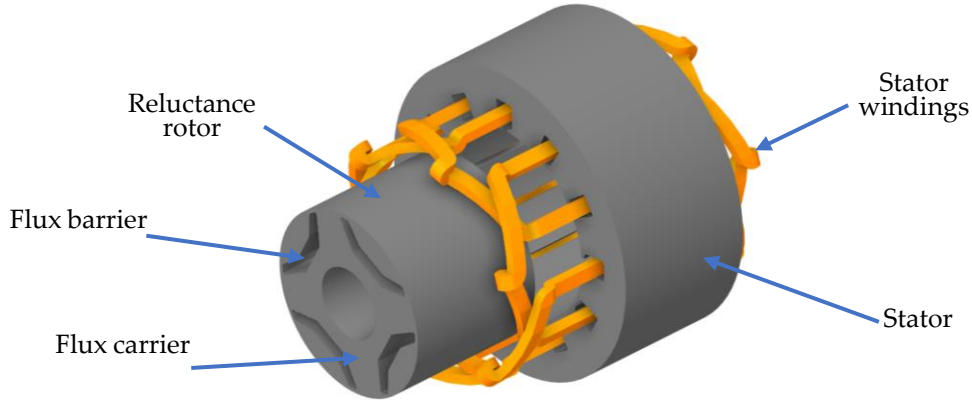


**Figure 1.2.** Sketch of a recent geometry for a 4-pole SynRM.

### 1.2. Electromagnetic torque

The design of an electrical machine must be such that it produces torque efficiently. In the SynRM, the electromagnetic torque is produced by the interaction between the flux in the air gap and their respective magnetizing current. Different expressions for the analytical calculation of the electromagnetic torque in a SynRM were delivered when the saturation and cross-coupling effect is neglected.

$$T_{em} = \frac{3}{2}p(\lambda_d i_q - \lambda_q i_d) \quad (1.2)$$

where  $i_d$ ,  $i_q$  are the current in the  $d$ -axis and  $q$ -axis, respectively; and  $\lambda_d$  and  $\lambda_q$  are the flux linkage in the  $d$ -axis and  $q$ -axis, respectively.

From the torque equations, it is clear that for a specified operating current and speed the electromagnetic torque developed on the shaft depends on the saliency ratio ( $\xi$ ); this reaching its maximum value for a given load angle ( $\delta$ ) or current angle ( $\alpha_i^e$ ). The vector diagram in the  $d$ - $q$  reference frame is shown in Figure 1.3 at steady-state, including the total iron losses, from which the equations relating load angle and current angle can be derived.

$$\delta = \tan^{-1} \left( \frac{\lambda_q}{\lambda_d} \right) \quad (1.3)$$

$$\delta = \tan^{-1} \left( \frac{1}{\xi} \frac{i_q}{i_d} \right) \quad (1.4)$$

$$\alpha_i^e = \tan^{-1} \left( \frac{i_q}{i_d} \right) \quad (1.5)$$

$$\delta = \tan^{-1} \left[ \frac{1}{\xi} \tan(\alpha_i^e) \right] \quad \text{or} \quad \tan(\delta) = \frac{1}{\xi} \tan(\alpha_i^e) \quad (1.6)$$

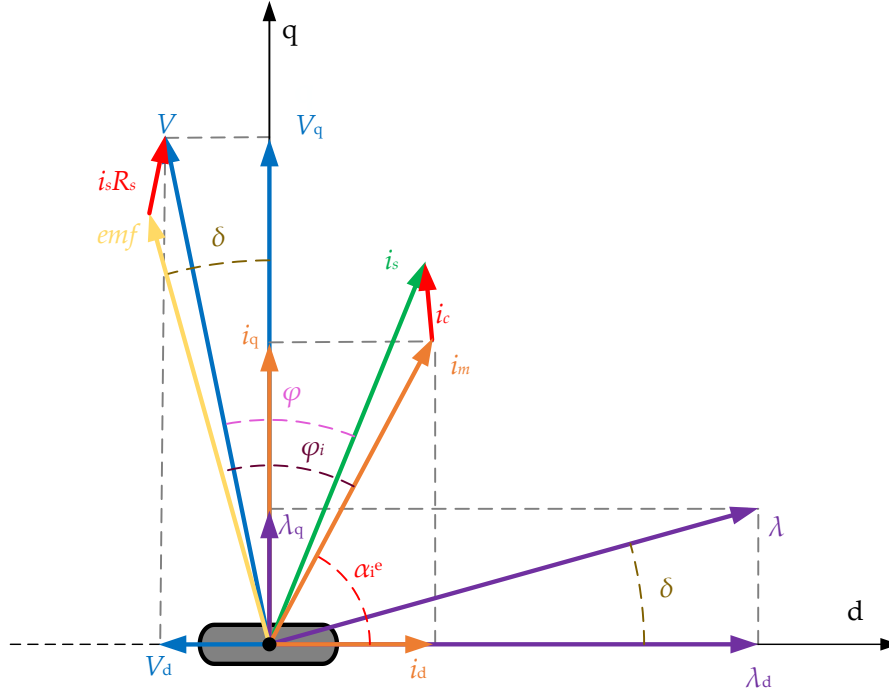


**Figure 1.3.** Phasor diagram for a SynRM at steady-state considering losses.

In the torque equations the machine inductances and flux linkages are constant since saturation is not considered, while the actual parameters depend on the current and the current angle. In fact, the electromagnetic torque shown in (1.2) does not consider the variation of the co-energy with the variation of the rotor position. Therefore, we would only obtain the average torque, it is more accurate to obtain the torque waveform using FEM simulations [26].

Combining the relationship between the current angle and the load angle it is possible to express the torque equation as a function of the load angle as

$$T_{em} = -\frac{3p}{2} L_q (\xi - 1) i_s^2 \sin\{2 \tan^{-1}[\xi \tan(\delta)]\}. \quad (1.7)$$

Figure 1.4 shows the influence of current angle and load angle on the electromagnetic torque. It can be observed that as the saliency ratio increases, the machine develops a higher torque value, which is directly dependent on the current and load angles.

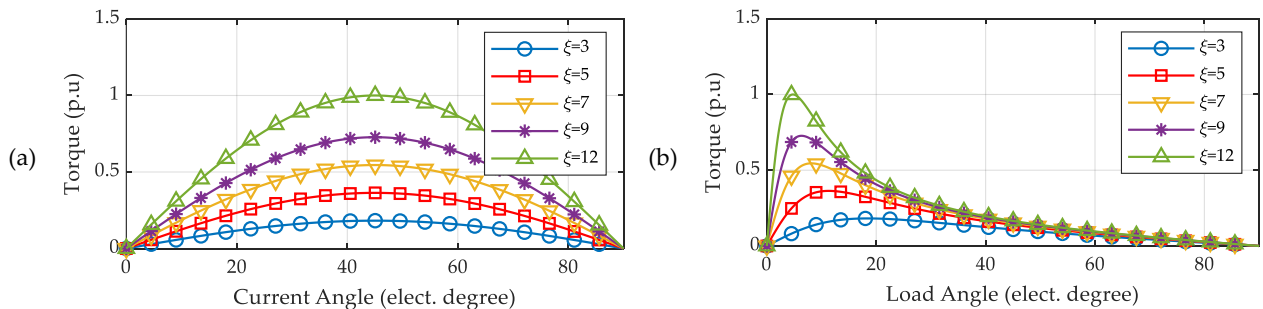


**Figure 1.4.** Influence of the current and load angle on the electromagnetic torque for a SynRM. (a) current angle vs. electromagnetic torque; (b) load angle vs. electromagnetic torque.

### 1.3. Internal Power Factor and Power Factor

The vector diagram in Figure 1.3 allows to identify the internal power factor (IPF) and the terminal power factor (PF) of the machine. This characteristic can be expressed in different forms [27]–[29].

$$\text{IPF} = \cos \varphi_i = \cos \left( \frac{\pi}{2} + \delta - \alpha_i^e \right) = \cos \left[ \tan^{-1} \left( \frac{\frac{\lambda_d}{\lambda_q} + \frac{i_q}{i_d}}{\xi - 1} \right) \right] \quad (1.8)$$

$$\text{PF} = \cos \varphi = \frac{P_{in}}{S_{in}} \quad (1.9)$$

where  $P_{in}$  is the real power and  $S_{in}$  is the apparent power.

Figure 1.5 shows the influence of current angle and load angle on the IPF for an ideal case, when the saturation and losses are neglected. It can be observed that as the saliency ratio increases, the machine develops a higher IPF, which is directly dependent on the current and load angles. The IPF is higher for higher current angles, but the same is not true for the load angle, where a higher IPF is obtained for lower load angles.

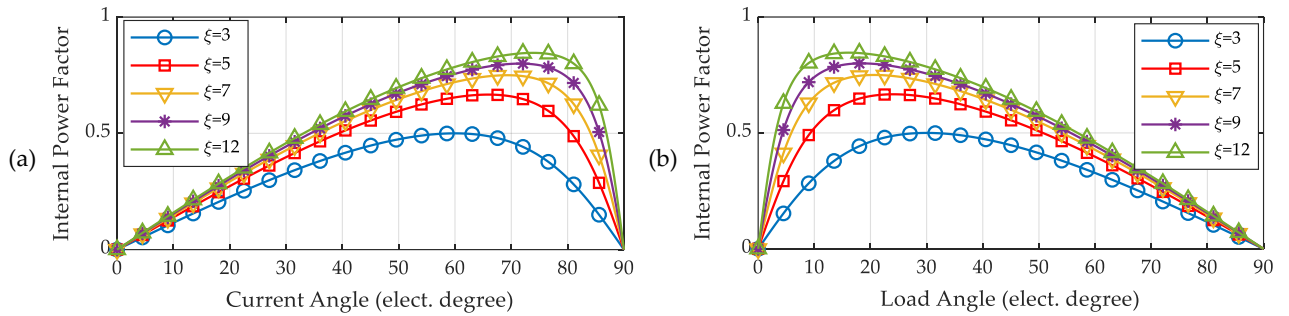


**Figure 1.5.** Influence of the current and load angle on the IPF for a SynRM. (a) current angle vs. power factor; (b) load angle vs. power factor.

Equation (1.8) shows that IPF depends on the current angle and the magnetic saliency of the machine. The maximum internal power factor ( $\text{IPF}_{\max}$ ) can be expressed by (1.10) [28], confirming that a higher saliency ratio ensures a higher IPF. It is observed in Figure 1.6 that to obtain an acceptable power factor the saliency ratio must be greater than 10 [30]. In practice, it is almost impossible to obtain such high saliency values, usually around  $\sim 5$ . Assisted permanent magnet synchronous reluctance machines (PM-SynRMs) with ferrite magnets are emerging as an alternative to achieve a suitable power factor.

$$\text{IPF}_{\max} = \frac{\xi - 1}{\xi + 1} \quad (1.10)$$

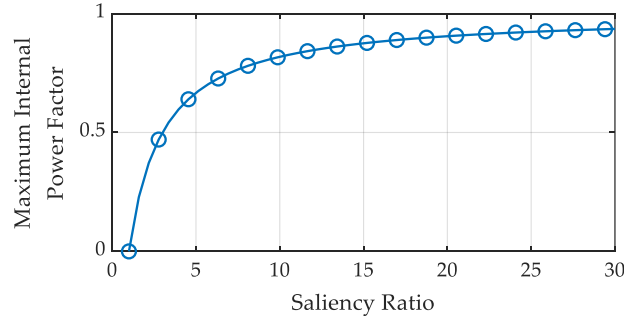


**Figure 1.6.** Maximum power factor for a SynRM for different values of saliency ratio.

When considering all physical phenomena in the electromagnetic analysis, the  $IPF_{\max}$  is not constant, as depicted in Figure 1.7. The saliency changes due to saturation and cross-coupling effects, leading to higher values for the  $IPF_{\max}$  at larger current angles.  $IPF_{\max}$  represents the limit for the PF of the machine. In any operating point, the machine will exhibit a lower PF than the  $IPF_{\max}$ . Regarding to the IPF and PF, for any operation point the PF will be a slightly lower than the IPF due the saturation and losses. In an ideal scenario, the PF would be equal to the IPF, but practical considerations introduce some deviations.

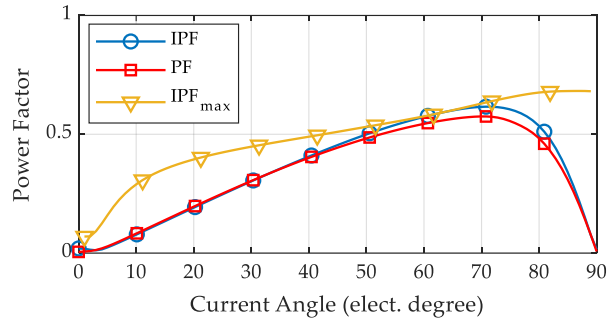


**Figure 1.7.** Behavior of the power factors in a six pole-three flux barriers SynRM analyzed through FEA.

#### 1.4. Control strategy

SynRMs can be controlled by vector control techniques, for which it is necessary to know the voltage and current equations in the  $d$ - $q$  plane. The equations below are obtained by using the vector diagram in Figure 1.3 as a reference and neglected losses.

$$v_d = -\omega L_q i_q = -\omega \lambda_q \quad (1.11)$$

$$v_q = \omega L_d i_d = \omega \lambda_d \quad (1.12)$$

$$v_s = \omega \sqrt{(L_q i_q)^2 + (L_d i_d)^2} \quad (1.13)$$

$$i_d = i_s \cos \alpha_i^e \quad (1.14)$$

$$i_q = i_s \sin \alpha_i^e \quad (1.15)$$

$$i_d^2 + i_q^2 = i_s^2 \quad (1.16)$$

where  $\omega$  is the electrical angular speed.

In addition, it is necessary to define the voltage and current limits, which are normally defined by the converter or the insulation characteristics of the machine. The current limit is defined by (1.17) as a circle with center at the origin, whose radius is defined by the current limit. On the other hand, the voltage limit is defined as an ellipse centered at the origin, (1.18), where the length of its axes decreases with increasing machine operating speed.

$$i_d^2 + i_q^2 = i_{lim}^2 \quad (1.17)$$

$$(L_q i_q)^2 + (L_d i_d)^2 = \left(\frac{v_{lim}}{\omega}\right)^2 \quad (1.18)$$

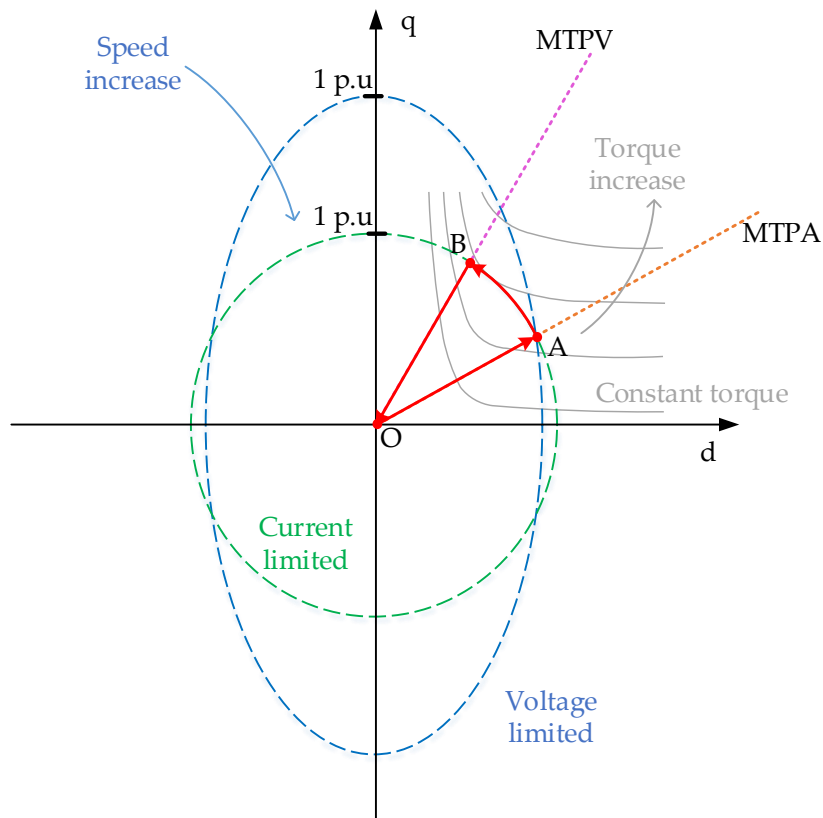


**Figure 1.8.** Machine operating points under vector control techniques.

The literature shows that a SynRM can operate efficiently in different operating modes according to speed and load [31]–[36], such as: maximum torque per ampere (MTPA) from zero speed until the machine reaches rated speed, flux weakening (FW) at medium and high speed, and maximum torque per volt (MTPV) at high speed. The operating points for any SynRM are shown in Figure 1.8; where, with increasing speed the operating points move along the OABO line. At OA the machine operates at MTPA, at AB it operates at FW and at BO it operates at MTPV.



### 1.5. Influence of saturation and cross-coupling effect

Magnetic saturation is normally not considered in the model when it is analyzed by the equations in the  $d$ - $q$  reference frame. However, it is necessary to consider this effect when it is desired to implement a high-performance control strategy or maximizing the machine capabilities. Saturation, resulting from the nonlinear characteristic of the ferromagnetic material, leads to the fact that the inductances and flux linkages in the  $d$ - $q$  axes are not constant, but rather a function of the currents [33], [37]–[40] and can therefore be expressed as

$$\lambda_d = \lambda_d(i_d, i_q) \quad (1.19)$$

$$\lambda_q = \lambda_q(i_d, i_q). \quad (1.20)$$

There are two ways to calculate the flux linkage equations considering the influence of saturation and cross-coupling effects. The first one and the more accurate is by means of FEA simulations in order to obtain the flux linkage per phase and, subsequently, apply the Clarke-Park transformation as follows.

$$\lambda_d = \frac{2}{3} \left[ \lambda_a \cos(\theta_m) + \lambda_b \cos\left(\theta_m - \frac{2\pi}{3}\right) + \lambda_c \cos\left(\theta_m - \frac{4\pi}{3}\right) \right] \quad (1.21)$$

$$\lambda_q = \frac{2}{3} \left[ \lambda_a \sin(\theta_m) + \lambda_b \sin\left(\theta_m - \frac{2\pi}{3}\right) + \lambda_c \sin\left(\theta_m - \frac{4\pi}{3}\right) \right] \quad (1.22)$$

where  $\lambda_a$ ,  $\lambda_b$  and  $\lambda_c$  are the flux linkage of each phase,  $p$  is the pole pairs and  $\theta_m$  is the angular coordinate referring to the stator reference frame and is calculated as follow

$$\theta_m = p(\theta_r + \theta_0) \quad (1.23)$$

where  $\theta_r$  is the rotor position and  $\theta_0$  is the initial rotor position.

Another way to obtain the flux linkage expressions for (1.19) and (1.20) if the inductance per phase is known, is to consider the following transformation

$$L_{dq0} = P(\theta_m)[L_{abc}(\theta_m)]P(\theta_m)^{-1}, \quad (1.24)$$

where

$$L_{dq0} = \begin{bmatrix} L_d & L_{dq} & L_{d0} \\ L_{qd} & L_q & L_{q0} \\ L_{0d} & L_{0q} & L_{00} \end{bmatrix}, \quad (1.25)$$

$$L_{abc}(\theta_m) = \begin{bmatrix} L_{aa}(\theta_m) & L_{ab}(\theta_m) & L_{ac}(\theta_m) \\ L_{ba}(\theta_m) & L_{bb}(\theta_m) & L_{bc}(\theta_m) \\ L_{ca}(\theta_m) & L_{cb}(\theta_m) & L_{cc}(\theta_m) \end{bmatrix}, \quad (1.26)$$

and

$$P(\theta_m) = \begin{bmatrix} \cos(\theta_m) & \cos\left(\theta_m - \frac{2\pi}{3}\right) & \cos\left(\theta_m - \frac{4\pi}{3}\right) \\ \sin(\theta_m) & \sin\left(\theta_m - \frac{2\pi}{3}\right) & \sin\left(\theta_m - \frac{4\pi}{3}\right) \\ \frac{1}{\sqrt{2}} & \frac{1}{\sqrt{2}} & \frac{1}{\sqrt{2}} \end{bmatrix}. \quad (1.27)$$

Considering the stationary reference frame, flux linkage expressions are

$$[\lambda_{dq0}] = \begin{bmatrix} \lambda_d \\ \lambda_q \\ \lambda_0 \end{bmatrix} = \begin{bmatrix} L_d & L_{dq} & L_{d0} \\ L_{qd} & L_q & L_{q0} \\ L_{0d} & L_{0q} & L_{00} \end{bmatrix} \begin{bmatrix} i_d \\ i_q \\ i_0 \end{bmatrix}. \quad (1.28)$$

It is assumed that the machine is being supplied by balanced three phase currents, reason why the zero-sequence component of the stator currents is zero. Thus, the  $d$ - $q$  axes flux linkage expressions of (1.19) and (1.20) can be calculated as

$$\lambda_d = L_d i_d + L_{dq} i_q, \quad (1.29)$$

$$\lambda_q = L_{qd} i_d + L_q i_q. \quad (1.30)$$

From this perspective, and once the effects of saturation and cross-coupling are included in the analysis, the torque equation (1.2) becomes

$$T_{em} = \frac{3}{2} p [L_{dq}(i_q^2 - i_d^2) - (L_q - L_d) i_d i_q]. \quad (1.31)$$

The **first term** is the torque produced because of the magnetic coupling between  $d$ - $q$  axes circuits and the **second term** is the reluctance torque. At low current the first term could be neglected since the magnetic coupling between axis has a low influence on the machine.

Figure 1.9 shows the influence of the current and the current angle on the machine inductances. It can be observed that the inductances when the permeability is infinite, the saturation is neglected, remain constant. In this case, the saliency of the machine is greater than eight and remains constant for every analyzed operating point. On the other hand, when saturation and the cross-coupling effect are considered, the inductances tend to decrease when the phase current increase.

The saturation of the ferromagnetic material causes a change in the saliency ratio of the machine. This is because the reluctance in the  $d$ -axis increases, resulting in a decrease in the  $d$ -axis inductance until it approaches the value of the  $q$ -axis inductance. For a fixed current, the  $q$ -axis inductance experiences a minor variation with the change in current angle. When the machine operates past the knee of the B-H curve, the  $q$ -axis inductance is considered constant, while the  $d$ -axis inductance decreases. However, the  $d$ -axis inductance experiences greater variations as the current angle changes; at a higher current angle, the  $d$ -axis inductance increases. Thus, as the current angle increases, the  $q$ -axis inductance remains constant, the  $d$ -axis inductance increases, and the machine's saliency ratio increases. Operating the machine with a large current angle can improve its performance. However, this approach moves the machine away from the MTPA trajectory and could lead to increased torque ripple.

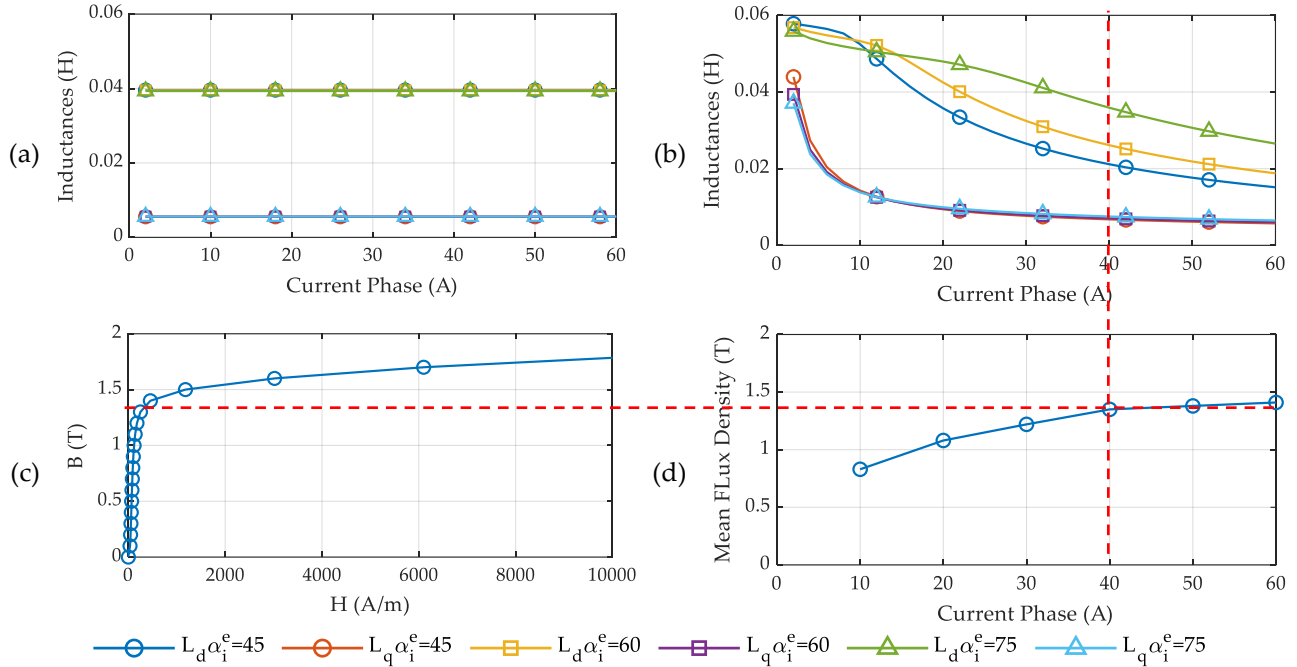


**Figure 1.9.** Influence of the current and the current angle on the machine inductances in a SynRM. (a) material with infinite permeability; (b) behavior of the material according to B-H curve; (c) M350-50A B-H curve; (d) mean flux density in the machine, six points were considered: barrier carrier, radial bridge, two points in the stator yoke and two in the teeth. The analysis was carried out in FEA.

### 1.6. Efficiency

Under the assumption that joule losses in the stator windings are dominant among other losses in the machine at low speeds, the efficiency can be calculated by [41], [42]

$$\eta \approx \left[ 1 + \frac{P_{cu}}{\omega T_{em}} \right]^{-1}. \quad (1.32)$$

This equation can be expanded with some modification as

$$\eta \approx \left[ 1 + \frac{1}{\frac{\omega}{3R_s} \left( \frac{T_{em}}{i_s^2} \right)} \right]^{-1} \quad (1.33)$$

where  $R_s$  is stator winding resistance. It can be deduced from (1.33) that increasing the ratio of  $\left( \frac{T_{em}}{i_s^2} \right)$  tends to increase the machine efficiency. However, this is only valid when core losses and additional losses are negligible compared to the stator resistive losses.

The torque generated by a SynRM is not constant due to space harmonics in the air gap, leading to torque ripple and contributing to core losses. Maximum machine efficiency cannot be achieved through optimization of rotor structure alone, as core losses occur both in the stator and rotor. The distribution of core losses in a standard SynRM is shown in Figure 1.10, with maximum values near the air-gap and minimal losses in the inside part of the rotor due to minimal changes in magnetic flux density over time.

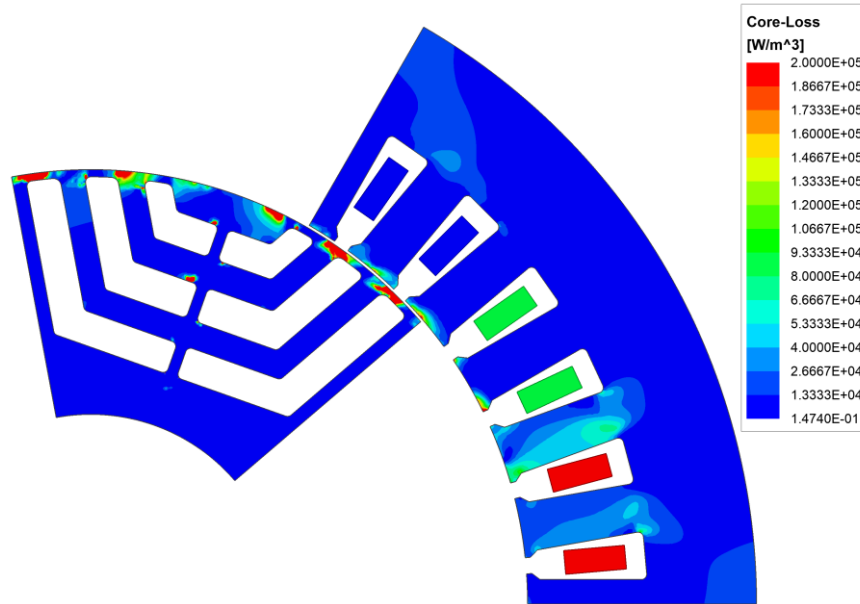


**Figure 1.10.** Core loss distribution in a 6-pole SynRM for low speed and 5 A/mm<sup>2</sup>.

The output parameters of a 6-pole SynRM, supplied at 50Hz with a current density of 5 A/mm<sup>2</sup>, are shown in Table 1.1. The efficiency, obtained from FEA, is 91.4% while the efficiency calculated using equation (1.33) is 92.2%. There is a small error in the calculation due the core losses was neglected, but this data can be considered a first approximation of efficiency in the early design stage.

**Table 1.1.** Output parameters for a case study 6-pole SynRM through FEM.

Parameter	Symbol	Quantity	Unit
Torque	$T_{em}$	49.5	Nm
Stator current	$I_s$	20	A
Rotor angular speed	$\omega$	104.7	rad/s
Winding losses	$P_{cu}$	432.7	W
Core losses	$P_{ed+d+hys+add}$	58.3	W

Figure 1.11 shows the impact of current angle and load angle on efficiency. As the saliency ratio increases, the efficiency of the machine increases. The efficiency is maximum when the machine develops the maximum torque and this depend on the current angle and load angle.

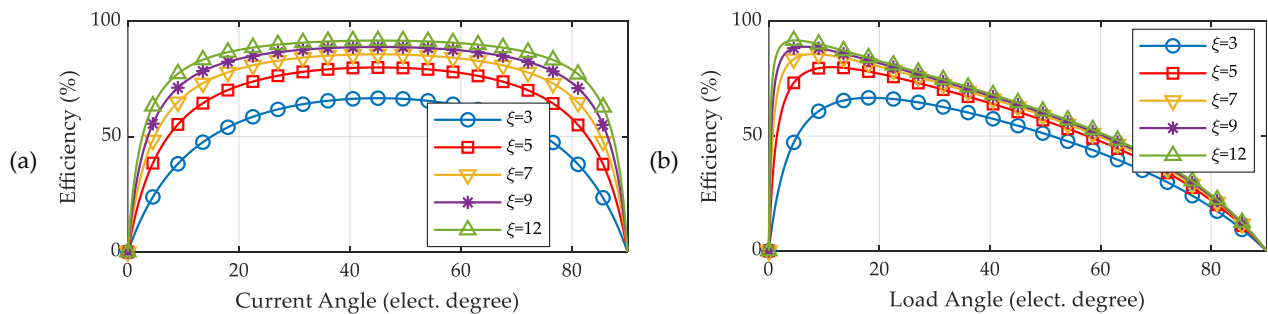


**Figure 1.11.** Influence of the current and load angles on the efficiency in a SynRM. (a) current angle vs. efficiency; (b) load angle vs. efficiency.

## 1.7. Design techniques. Machine performance improvement

### 1.7.1. Analytical models vs. Finite elements methods

Finite Element Analysis (FEA) is one the most popular tool to design and optimize SynRM [9] thanks to the ability to incorporate all the electromagnetic phenomena present in the machines with high accuracy. Although FEM generally produces accurate results, it is subject to a high computational cost, especially during an optimization process where numerous iterations are required to obtain a good design. Consequently, a great deal of research has been conducted to build analytical models that are capable to preserve good accuracy, compared to FEM and achieve results significantly faster [43], [44].

The work done in [43] presents an analytical model based on Maxwell's equations to calculate the flux density in the air-gap. The effects of rotor and stator slots are considered by conformal mapping; however, this does not include the derivation of torque and torque ripple. In [44], an analytical model where the reluctance of the flux barriers is calculated from the conformal mapping is implemented, but the effect of stator slotting is neglected. A simplified method is proposed in [45] from developing a magnetic circuit for a SynRM, the impact of stator slots is neglected. On the other hand, extensive work has been done evaluating the magnetic flux density in the air-gap and the torque as a function of the rotor magnetic potential and the stator electric loading [17], [46]–[50]. The air-gap magnetic flux density is defined as a function of the rotor magnetic potential produced by the stator electric loading, and the torque as an integrated function of the stator electric loading and the rotor magnetic potential. Similarly, the effect of stator slotting is neglected, with the consequent absence of the slot harmonics that are a fundamental component to be considered to capture the torque fluctuations.

A further analytical model for SynRM and its validation through FEM is presented in [51]. This work calculates the air-gap flux density as a function of stator and rotor magnetic potential and the torque by integrating the Lorentz's force density along the air gap surface; but the study neglecting the slotting effect. Using the same principle as in [51], a SynRM with asymmetric flux barrier is designed in [52] to minimize the torque ripple. To obtain higher fidelity, this analysis considers the slotting effect with the conformal mapping technique. This technique requires a hard algebraical work which becomes critical as the number of flux barrier increases.

An accurate Analytical Model (AM) for SynRMs can help the reduction of time spent to derive the preliminary design phase. These models, besides being fast, must deliver sufficiently accurate results; but most importantly, they need to enable the correlation between different parameters defining machine performance, such as electrical, magnetic, and geometrical. The analytical equations allow to study the behavior of certain performance indexes of the machine including the variation of the design parameters and their relationships.

Amongst the features that an AM for SynRM should include, the interaction among the flux barriers and the stator teeth is the most important; the relative position between them causing the appearance of spatial harmonics in the air-gap flux density. These harmonics are one of the primary sources of torque ripple in this type of machine. This issue is solved in [53] where an accurate AM for SynRMs is presented. This work succeeds in predicting the air gap flux density and electromagnetic torque considering the slotting effect.

### 1.7.2. Rotor structure optimization employing asymmetries

Lately, studies have been conducted to investigate the impact of asymmetric structures on the performance of electrical machines [54]–[57], particularly Interior Permanent Magnet Synchronous Machines (IPM). This research has revealed an improvement in average torque and reduction in cogging torque when the rotor structure is designed to be asymmetric. The application of asymmetric designs is believed to lead to an increase in average torque, a decrease in cogging torque and torque ripple. Historically, electrical machines have been designed with symmetrical structures and windings for each pair of poles, with the same electrical and magnetic characteristics being repeated in both the rotor and stator structures.

The stator of an electric machine comprises of the teeth and windings as its main active elements, which are typically designed to be identical and symmetrical. Recent studies have focused on the asymmetrical design of the teeth and slots in the stator structure, with the goal of reducing cogging torque. One example of this is found in [58] where it was shown that asymmetrical design of the stator teeth can lead to a reduction in cogging torque. The impact of unequal tooth width in the stator structure has also been studied in [59], which found that adjusting the width can result in similar torque values while reducing stator current values, leading to a reduction in copper losses and an increase in machine efficiency.

The opening of the slots in a stator may vary and may not be precisely centered in each slot. Additionally, variations in the dimensions of the teeth can be used to achieve optimal electromagnetic design [60]. However, it is typical for all poles in the rotor to be designed symmetrically from the centerline of each pole or identically from pole to pole. Asymmetric design elements can be applied to the rotor, such as the positioning of magnets in PMSMs or the design of flux barriers in IPMSs and SynRMs. These changes can improve the performance of the machine, as evidenced by the numerous patents [61]–[64] and articles [17], [54]–[58], [65]–[75] that have been published on the subject in recent years.

There is a significant gap in the number of studies addressing asymmetries in the stator and rotor structures. Research in [56], [65], [66] have shown that in IPMs with an asymmetric rotor can lead to the two torque components, the excitation and reluctance torque, to achieving their maximum values for the same stator current angle. On the other hand, in SynRMs, the rotor structure plays a crucial role in their performance. The optimal design of flux barriers can increase the saliency ratio, improve average torque, power factor, and efficiency, while also reducing torque ripple as reported in [17], [75].

In [56], an analysis was conducted on IPM with radial magnets (spoke type). Another study, referenced in [70], examined IPMS with V-type rotors. Previous research has shown that applying asymmetries to the rotor structure can improve the average torque. Also, in these IPMs, the two torque components reach their maximum value at the same current angle. A new asymmetric rotor design, with additional flux barriers on the interpolar axis, was compared with a V-type IPM in [57]. This design resulted in an increase in average torque, decrease in torque ripple, and improved constant power characteristic.

The design of PMA-SynRM is presented in reference [71]. The rotor design's asymmetry is achieved through a combination of magnet positioning and flux barrier design. In [65], a rotor structure was developed combining the advantages of both a SynRM and a PMSM. The rotor assembly is designed to achieve the maximum of both torque components at the same current angle and significantly reduce torque ripple. Reference [75] presented a rotor with two flux barriers, with

the position of the barriers relative to the stator teeth being different at each rotor pole, creating an asymmetrical design. This design reduces torque ripple and increases average torque.

A comprehensive study on the impact of asymmetries in the rotor structure of a SynRM was conducted in reference [55], evaluating various rotor topologies without radial ribs to enhance average torque and decrease torque ripple. The study compares a symmetric structure with three asymmetric designs. All three asymmetric designs showed an improvement in average torque, however, only two achieved a reduction in torque ripple, highlighting those asymmetric structures as a promising approach in the design of electrical machines.

It is apparent that most research on asymmetric structures has been focused on IPMs, with relatively few studies on the benefits of asymmetries in SynRMs. The most extensive analysis on this subject can be found in [18], where the impact of asymmetric positioning of flux barriers relative to the q-axis of the rotor on machine performance is examined for a specific operating point. However, it is important to note that an electrical machine does not function continuously at the same operating point, as variations in the load will cause the operating point to change. Thus, it is crucial to understand how the machine responds to these changes.

### 1.7.3. Rotor skewing

Skewing techniques can be classified into two main categories: continuous skewing and discrete skewing (also called step skewing). The first one involves rotating each lamination of the stator or rotor core in regular angular distribution, between the first and the last slice equal to the skew angle [76], as depicted in Figure 1.12 (b). This can drastically reduce torque ripple but complicates and makes the manufacturing process more expensive since each lamination of the rotor has a different position with respect to a symmetry axis, thus requiring specific tooling. In turn, the second category, considers the division of the rotor stack into a few discrete segments, as shown in Figure 1.12 (c).

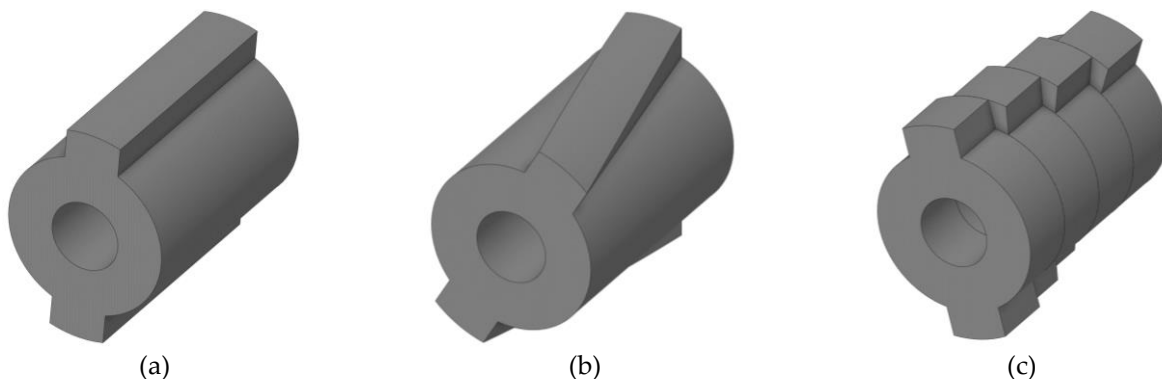


**Figure 1.12.** 3D sketch of different types of skew. (a) reference skewless rotor; (b) continuous skew; (c) discrete skew, also mentioned as step skew.

A considerable number of works have addressed the rotor skewing technique using the conventional one-slot-pitch skew angle. These works can be found in references [77]–[84]. In [77], the performance of a SynRM is compared when it is operated without skewing to when the rotor is skewed by one stator tooth pitch. Reference [78] investigates the effect of rotor skewing on reducing slot harmonic torques, using a conventional skew angle of one stator slot pitch, but this reduces the average torque as well. This was confirmed in [79] and [80]. In [81], the equation to calculate the skew angle to suppress the stator slot harmonic component (one slot pitch) was presented, considering the

number of slices in the calculation. The novel forced feasibility concept was introduced in [82] to improve optimization convergence and reduce overall optimization time in a SynRM design. A rotor skew was chosen as the best suited torque-ripple mitigation option by skewing the rotor at an angle of one stator slot. Recently in [83], a SynRM with salient pole rotor was continuously skewed by one stator slot pitch to improve energy conversion and reduce torque ripple. The impact of rotor skewing on torque ripple in SynRMs was analyzed in recent research [84], comparing both continuous and segmented rotor skewing. Post-optimization simulations were performed for both methods and yielded similar results, with a slight advantage to segmented rotor skewing due to the increased cost of continuous skewing. In both cases, the total skew angle was equal to one stator slot. As it may be noted from the dates of these works, the one-slot-pitch skewing trend has been dominant as a post optimization process, applicable to several machine topologies up to date.

In turn, several papers have discussed the skewing technique for reducing torque ripple [85]–[91], but they lack information on the selection of the skew angle or the skewing parameters used. In [85], a rotor design with an asymmetric flux barrier was created to reduce torque ripple by splitting the rotor into two step-skewed parts. However, the paper does not mention the method used to determine the skew angle, which is assumed to be equal to the slot pitch. Reference [88] evaluates the suitability of SynRMs for electric traction applications. Skew is applied to reduce torque ripple by using a  $2.5^\circ$  mechanical skew angle between three stacks, resulting in an angle close to the slot pitch. In [89], the torque ripple was reduced by dividing the machine into three layers using step skew, but the skewing angle is not specified. A SynRM was optimized using topology optimization in [90], which increased the torque compared to a model optimized with parameters, but also increased the torque ripple. The skewing technique was used to reduce the torque ripple by dividing the rotor into two slices, but the specific skew angle and its determination method are not reported. In [91], the goal was to reduce torque ripple through rotor skewing while maintaining a power factor through optimization. The study found that the optimum mechanical skew angle across all machines was 2.5 mechanical degrees, very close to the slot pitch. All these works seem to match the one-slot-pitch skewing trend.

Despite the prevalence of the slot pitch angle as the optimal skew angle in literature, references [73], [92] question its effectiveness in minimizing torque ripple. Reference [73] demonstrates that a torque ripple of less than 3.0% can be achieved by applying rotor skew. The optimum rotor skew angles, ranging from 60-70% of a slot pitch angle for the 24-slot machine and 30-80% for the 36-slot machine, have as an outcome this achievement. The analysis highlights that the ideal rotor skew angle heavily depends on both the stator configuration and the rotor topology. In [92], a comparison between continuous skewing discrete skewing was performed over a SynRM. The results indicated that the torque ripple was significantly reduced even with two stacks, while only slightly decreasing in the average torque when high order torque harmonics were produced. Some results showed that the optimal skew angle differed from the traditional one-slot pitch, being either higher or lower, depending on the type of skew technique applied (continuous or discrete).

As a result, recent trends have been investigated to improve the effectiveness of skewing in different topologies [93]–[95]. A new unconventional magnet step-skew method for PMSM is introduced in [93]. It involves varying both the length of the magnet and the skew angle between magnet segments, in contrast to the constant stack length and step-skew angle in conventional PM motors. A semi-FEA algorithm is developed showing improved performance compared to conventional step-skew. However, it comes with increased magnet manufacturing cost. In [94] a new



method for parameterizing the flux barrier profiles of SynRMs and PMA-SynRMs was introduced. To reduce torque ripple the skew angle is obtained through a parametric FEA analysis. A discrete rotor skewing of  $4^\circ$  in 3-step pieces is applied which deviates from the conventional  $10^\circ$  angle for a 36-slot machine based on one slot pitch. In [95], the impact of step skewing on the output torque and motor inductance in a 30-slot/4-pole SynRM configuration was examined. A comparison of step skewing was made theoretically, and the study considered the effect of two harmonic orders but did not account for the number of steps in the skewing angle calculation. Moreover, it was discovered that the average torque reduction resulting from skewing is dependent on the machine operating point.

This topic has brought increased attention in the literature. A better understanding of how the optimal skewing can be achieved at the design stage is an important factor in the sizing of a SynRM. It is necessary a generalized multi-step skewing approach for SynRM which considered a torque ripple harmonic content and not the traditional one-slot-pitch skewing technique. This aims to serve as an input of post-optimization processes in the design stage of SynRMs.

Reducing the difficulties and cost of the manufacturing process and providing the possibility of mitigating relevant harmonic content in the electromagnetic torque may be achieved when applying discrete multi-step skewing in a SynRM. Of course, the manufacturing complexity and performance benefits may be adversely affected as the number of steps increases, but this is yet to be disclosed. As a result, in [96] is propose some generalized analytical expressions for multi-step discrete skewing on SynRM in order to mitigate undesired harmonic content of the electromagnetic torque and its influence on other harmonic components.

### *1.8. Summary*

This chapter provides an overview of the basic principles of operation for SynRMs. It covers the mathematical model, vector diagram, and including the saturation and cross-coupling effect between  $d$ - $q$  axes. Additionally, a first approximation of the efficiency calculation is developed. Key design features of the machine are described and how their affect the machine's performances. As well, the electrical, mechanical, magnetic, and geometrical parameters and their impact on the first stage of the machine's design were discussed. Additionally, a few designs technique that play a major role in the performance improvement in the design step of SynRM were highlighted, such as the use of asymmetrical barriers on the rotor and the use of the skew technique to reduce torque ripple.

## Chapter II: Accurate Analytical Model for Synchronous Reluctance Machine

This chapter introduces an Analytical Model (AM) for predicting air-gap flux density and electromagnetic torque in SynRMs with good accuracy. The impact of stator slotting and flux barriers on the torque and magnetic flux density in the air-gap is analyzed. Two methods for calculating torque are studied, and their limitations in accounting for the effect of slotting are emphasized. The method will first be developed for a rotor with one flux barrier and then expanded to multiple barriers. The AM's results are compared with FEM results to validate the model.

### 2.1. Main assumptions

Figure 2.1 shows a general rotor geometry for a SynRM. The following assumptions are made for the implementation of the analytical method:

- the tangential iron bridges of the rotor barriers are highly saturated under normal working conditions, the relative permeability in these parts is negligible. Therefore, the regions of the rotor iron bridges are considered as air [43], [44], [50], [51], [97],
- the rotor structure has no radial iron bridges,
- the permeability of the ferromagnetic material tends to infinity,
- and the tangential flux density is not considered for the torque calculation.

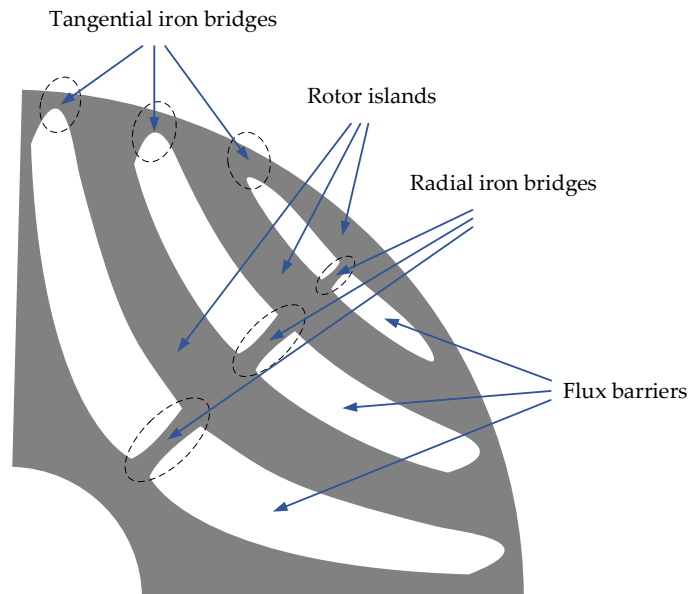


**Figure 2.1.** Sketch of a general rotor geometry for a SynRM.

The above assumptions have been considered in most of the analytical models described so far, e.g., [43], [44], [50], [51], [98]. These assumptions also limit the proposed method to low-speed applications. In high-speed applications the radial and tangential bridges must be thick enough to provide the rotor with the required structural integrity. This causes the bridges to not fully saturate and provide a low reluctance path for the q-axis flux, penalizing the saliency ratio of the machine. The fact that the bridges are wide causes the cross-coupling phenomenon between the d-axis and q-axis to be present to a greater extent in high-speed SynRM. The above consideration means that in high-speed SynRM, bridges must be taken into account in the electromagnetic analysis.

## 2.2. Air-gap flux density calculation

The approach for calculating the magnetic flux density consists mainly of two steps: first, the magnetic potential across the flux barriers is determined. Secondly, the magnetic potential is combined with Ampere's Law to calculate the flux density distribution of the air-gap.

It is necessary to start by calculating the MMF, which can be derived from Ampere's Law; according to [99], it can be defined by (2.1) for a three-phase winding.

$$MMF_g(\theta_s, \theta_m) = \frac{3}{2} MMF_f \sum_{n=-\infty}^{\infty} \frac{k_{w,6n+1}}{6n+1} \sin[(6n+1)\theta_s p - p\theta_m - \alpha_1^e] \quad (2.1)$$

$$MMF_f = \frac{2}{\pi} N_t \sqrt{2} I_{rms} \quad (2.2)$$

where  $k_{w,6n+1}$  is the winding factor,  $p$  is the pole pair of the machine,  $\theta_s$  is the position along the stator periphery,  $\theta_m$  is the rotor position,  $\alpha_1^e$  is the current angle,  $N_t$  is the turns per pole per phase,  $I_{rms}$  is the supply current and  $n = 0, \pm 1, \pm 2 \dots \pm \infty$ .

AM's for the calculation of the flux density is presented by several authors in [48]–[50], [85], [100], where the flux density in the air-gap is calculated from the magnetic potential of the stator and rotor in the air-gap like see in Figure 2.2, as in

$$B_g(\theta_s, \theta_m) = \frac{\mu_0 [-U_s(\theta_s, \theta_m) + U_r(\theta_m)]}{g} \quad (2.3)$$

where  $U_s(\theta_s, \theta_m)$  is the stator magnetic potential, which is equivalent to the drop of the  $MMF(\theta_s, \theta_m)$ ,  $U_r(\theta_m)$  is the rotor magnetic potential,  $g$  is the air-gap length and  $\mu_0$  the air permeability.

The electric loading produces a magnetic potential distributed along the inner circumference of the stator. The magnetic flux (green lines in Figure 2.2) crossing the flux barrier has a magnetic potential in the rotor, calculated by (2.4). The rotor potential will be considered constant in each magnetic "island" of the rotor, bordered by the air-gap and the flux barrier, and zero in the remainder, this can be seen in Figure 2.2.

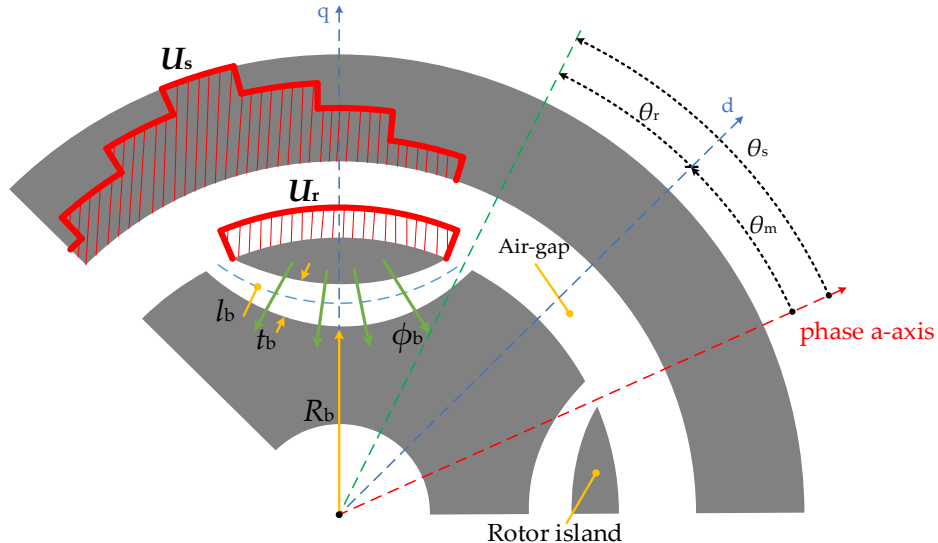


**Figure 2.2.** Stator and rotor magnetic potential in the air-gap.

In this research, the behavior of the flux barrier opening is the same as the behavior of the slot. Therefore, just as the slot opening is considered in the stator magnetic potential from the winding factor, it will also be considered in the rotor magnetic potential. This behavior is considered from a wave between the points  $(\alpha_r, D_{ro}/2)$  and  $(l_{br}, U_r)$  in Figure 2.3.

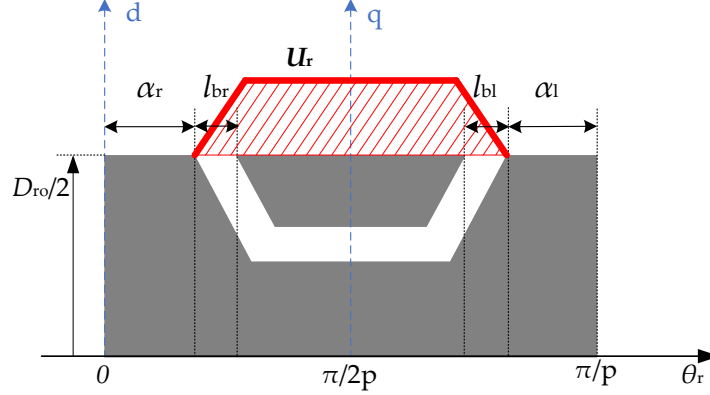


**Figure 2.3.** Flux barrier geometry and rotor magnetic potential in a rotor pole.

For the slot opening on the right side the curve will have positive slope and for the left side negative slope.

$$U_r(\theta_m) = \Phi_b(\theta_m) \mathcal{R}_b \quad (2.4)$$

$$\mathcal{R}_b = \frac{t_b}{\mu_0 l_b l_{axial}} \quad (1.5)$$

where  $\Phi_b(\theta_m)$  is the magnetic flux crossing the flux barrier,  $\mathcal{R}_b$  is the reluctance of the flux barrier,  $t_b$  and  $l_b$  are the width and length of the flux barrier, respectively.

The flux crossing the flux barrier is calculated by (2.6), integrating the magnetic flux density in the air-gap from the limits defined by the position of the flux barriers. A single flux barrier per pole structure will be analyzed to explain the procedure correctly.

$$\Phi_b(\theta_m) = \int_{\alpha_r}^{\frac{\pi}{p} - \alpha_1} \frac{-B_g(\theta_s, \theta_m) l_{axial} D_{ro}}{2} d\theta_s \quad (2.6)$$

where  $D_{ro}$  is the rotor outer diameter.

Substituting (2.3), (2.4), and (2.5) into (2.6) and performing algebraic work, it is possible to derive the magnetic potential of the rotor as

$$U_r(\theta_m) = \left[ \frac{D_{ro}}{2g} \right] \left( \frac{t_b}{l_b} \right) \int_{\alpha_r}^{\frac{\pi}{p} - \alpha_1} U_s(\theta_s, \theta_m) d\theta_s - \left[ \frac{\pi}{p} - (\alpha_r + \alpha_1) \right] U_r(\theta_m) \quad (2.7)$$

Simplifying (2.7)

$$U_r(\theta_m) = a \int_{\alpha_r}^{\frac{\pi}{p} - \alpha_1} U_s(\theta_s, \theta_m) d\theta_s \quad (2.8)$$

where

$$a = \frac{\left\{ \left[ \frac{D_{ro}}{2g} \right] \left( \frac{t_b}{l_b} \right) \right\}}{\left\{ 1 + \left[ \frac{D_{ro}}{2g} \right] \left( \frac{t_b}{l_b} \right) \left[ \frac{\pi}{p} - (\alpha_r + \alpha_l) \right] \right\}} \quad (2.9)$$

Figure 2.4 shows the results of applying the procedure described above for a SynRM with two poles pairs. The stator has 48 slots and distributed three-phase windings; the other design data are summarized in Table 2.1.

**Table 2.1.** Machine main parameters.

Parameter	Symbol	Quantity	Unit
Stator outer diameter	$D_{so}$	346.7	mm
Stator inner diameter	$D_{si}$	245.2	mm
Rotor outer diameter	$D_{ro}$	244	mm
Rotor inner diameter	$D_{ri}$	70	mm
Air-gap length	$g$	0.6	mm
Radio barrier	$R_b$	45	mm
Axial length	$l_{axial}$	172	mm
Slot pitch	$\tau_s$	7.5	mechanical degrees
Slot opening	$b_{ss}$	1.4	mechanical degrees
Flux barrier width	$t_b$	15	mm
Flux barrier length	$l_b$	194.5	mm
Flux barrier opening	$l_{b(r=1)}$	7.08	mechanical degrees
Flux barrier angle	$\alpha_{(r=1)}$	10.5	mechanical degrees
Turns per slot	$N_s$	10	turns
Current Angle	$\alpha_i^e$	45	electrical degrees

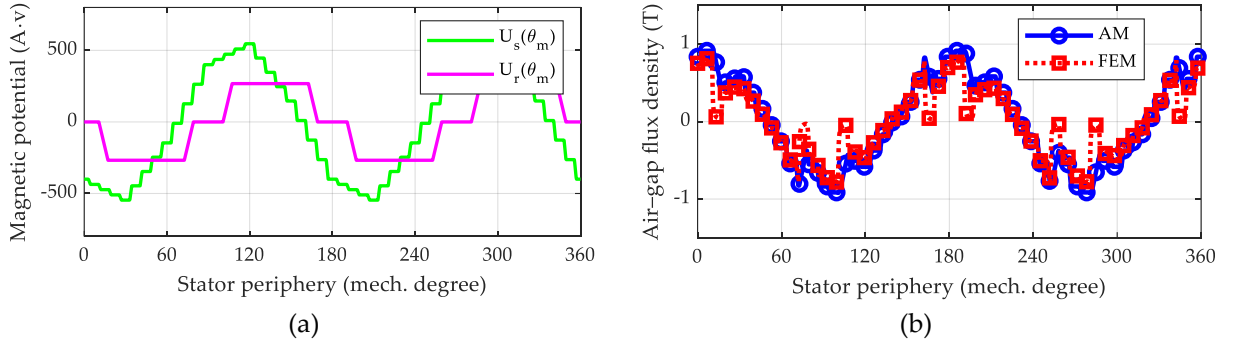


**Figure 2.4.** Magnetic potential and air-gap flux density without slotting effect for  $\theta_m = 0$ . (a) stator and rotor magnetic potential; (b) air-gap flux density.

For this analysis, the of the electric loading ( $\hat{K}_s$ ) fundamental value is the 8.4 A/mm. Figure 2.4 (b) compares the magnetic flux density in the air-gap calculated by analytical model, which is represented by the acronym AM on the curve, and obtained in FEM. It is important to note that only the effect of the rotor flux barriers is considered; the influence of the stator slots is not considered. Equation (2.3) is modified to consider the effect of the flux barriers on the air-gap flux density, where

$P(\theta_s, \theta_m)$  is the air-gap permeance (2.11) and  $g_r(\theta_s, \theta_m)$  is the air-gap function, it is calculated from the infinite slot assumption [101].

$$B_g(\theta_s, \theta_m) = P(\theta_s, \theta_m)[-U_s(\theta_s, \theta_m) + U_r(\theta_m)] \quad (2.10)$$

$$P(\theta_s, \theta_m) = \frac{\mu_0}{(g + g_r(\theta_s, \theta_m))} \quad (2.11)$$

Similarly, the effect of stator slotting can be included in the result of magnetic flux density in the air-gap under the same assumption of the infinite slot, as clear from the results shown in Figure 2.5. Both effects, slotting and barriers, are correctly processed by the proposed AM. In Figure 2.5 (a) the flux density waveform has the same behavioral trend for both analyses, FEM and AM. Figure 2.5 (b) shows the harmonic analysis for the air-gap flux density. As expected, the AM overestimates the flux density. This can be seen in Figure 2.5 (b), where the fundamental component is slightly larger in the comparison with the results obtained by FEM. This difference is mainly due to the assumptions that were adopted during the development of the analytical model, i.e., by not considering the nonlinearities in the machine. The remaining harmonic components in the AM show the same behavior as those obtained from FEM. This flux density distribution in the air-gap is used to calculate the electromagnetic torque waveform in the following section.

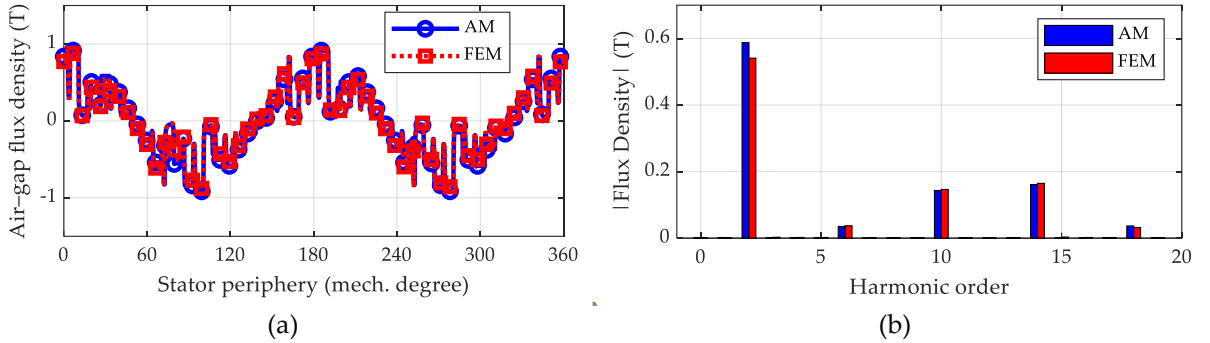


**Figure 2.5.** Air-gap flux density with slotting effect for  $\theta_m = 0$ . (a) air-gap flux density waveform; (b) harmonic distribution of the air-gap flux density.

### 2.3. Torque calculation

The electromagnetic torque waveform is essential to evaluate torque ripple; in basic terms, torque ripple can be defined mathematically, as shown in (2.12), it expressed in Nm (peak to peak).

$$T_{rp} = \max(T_{em}) - \min(T_{em}) \quad (2.12)$$

Historically, the torque of a SynRM was derived from two methods. Several researchers mainly focus on evaluating the torque as a function of stator electric loading and rotor magnetic potential [48]–[50], [85], [100]. The torque can be obtained by integrating Lorentz's force ( $B_g(\theta_s)K_s(\theta_s)$ ) along the air-gap surface, as in

$$T_{em}(\theta_m) = R^2 l_{axial} \int_0^{2\pi} B_g(\theta_s, \theta_m) K_s(\theta_s, \theta_m) d\theta_s. \quad (2.13)$$

where  $l_{\text{axial}}$  is the axial length of the machine,  $R$  is the air-gap radius and  $K_s(\theta_s, \theta_m)$  is the electric loading.

In [99], the effect of the  $MMF$  in the air-gap field is represented with sufficient accuracy by a current charge distributed over the area of the slot opening, in other words, by the electric loading. Therefore, the  $MMF$  can also be calculated from (2.14), from where the electric loading can be obtained.

$$MMF_g(\theta_s, \theta_m) = \int \frac{K_s(\theta_s, \theta_m) D_{si}}{2} d\theta_s \quad (2.14)$$

The electromagnetic torque for both flux densities calculated in the previous section is shown in Figure 2.6. These curves were performance by moving the rotor 60 mechanical degrees, which corresponds to two torque ripple periods for three-phase machine [102]. When the effect of stator slotting is ignored, Figure 2.6. (a), the comparison with FEM is satisfactory; while when the influence of slotting is evaluated, the results show considerable differences, Figure 2.6. (b). Therefore, the above method effectively determines the electromagnetic torque waveform when the stator slotting effect is neglected.

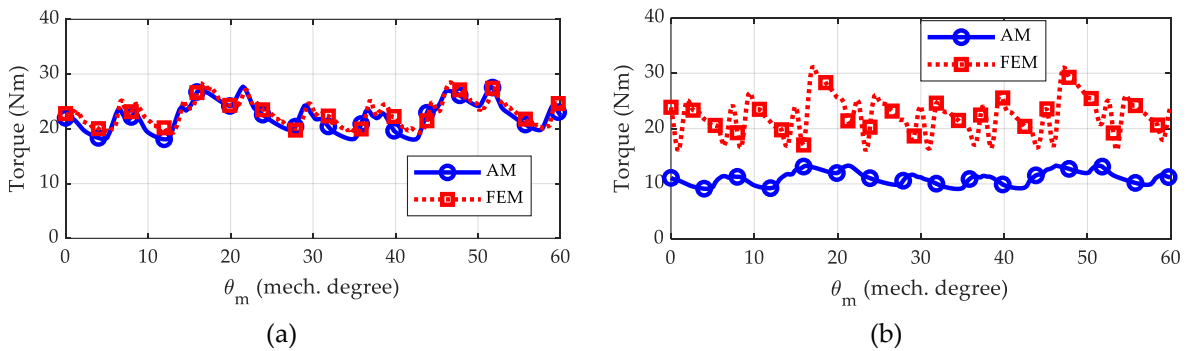


**Figure 2.6.** Electromagnetic torque waveform for two torque ripple periods. (a) without slotting effect; (b) with slotting effect.

Harmonic analysis was performed to analyze this fact. The magnetic flux density is correct; at any instant of time studied, the comparison with FEM is accurate. Additionally, the electric loading is relatively easy to obtain and is the same for both cases investigated, including the slotting effect or not. Figure 2.7 shows the torque when considering specific harmonics of the magnetic flux density. It is observed that considering only the first harmonic, the average torque of the analytical model and FEM are matching well; the exact values are shown in Table 2.2. However, as the number of harmonics of the flux density increases, torque ripple appears, and the average torque decreases. This effect becomes more predominant when harmonics above the 50<sup>th</sup> are included (green curve in Figure 2.7). It is important to note that the flux density's harmonics significantly influence the final torque result.

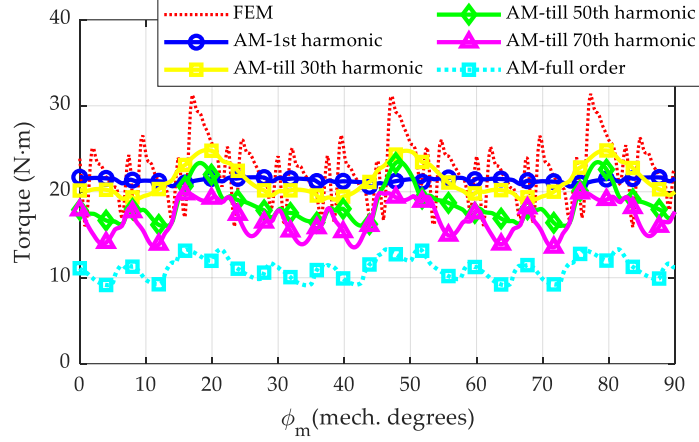


**Figure 2.7.** Harmonic torque analysis when considering slotting effect for two torque ripple periods.

It is well known that the stator slotting introduces the higher order harmonics in the magnetic flux density. Therefore, by not considering the higher order harmonics, it again ignores the slotting effect, which is not the objective of the research. Thus, the calculation method for electromagnetic torque from Lorentz's force is effective only for finding the average torque when the stator slotting effect is considered.

Based on the above, the magnetic flux density in the air-gap can be decomposed as a sum of harmonics as

$$B_g(\theta_s) = \sum_{v=1}^{\infty} |B_g(v)| \cos(v\omega_0\theta_s + \varphi(v)). \quad (2.15)$$

**Table 2.2.** Average torque and torque ripple values for harmonic analysis.

Analysis method & harmonic order	$T_{avg}$ (Nm)	$T_{rp}$ (Nm)
FEM	21.03	15.3
AM-1st harmonic	21.33	1.14
AM-30th harmonic	21.29	5.76
AM-50th harmonic	18.49	7.48
AM-full order	11.07	4.22

In the same way, the electric loading can be decomposed as follows,

$$K_s(\theta_s) = \sum_{\eta=1}^{\infty} |K_s(\eta)| \cos(\eta\omega_0\theta_s + \varphi(\eta)). \quad (2.16)$$

Therefore, the average torque is calculated by (2.17) when  $v = \eta = 1$ ;

$$T_{avg}(\theta_m) = -R^2 l_{axial} \int_0^{2\pi} |B_g(v)| |K_s(\eta)| \cos(v\omega_0\theta_s + \varphi(v)) \cos(\eta\omega_0\theta_s + \varphi(\eta)) d\theta_s \quad (2.17)$$

Furthermore, the principal of the torque pulsation relative to slot harmonics lays on the fact that, in SynRM the rotor is forced to be aligned with the minimum reluctance. Any change on this



alignment causes variations of stored energy at the slots opening area in the rotor and stator, results in changes in their equivalent co-energy. These variations which depend on the rotor angle and them are the potential sources for torque ripple [103], [104]. Discarding the magnetic saturation, the torque ripple is calculated from the total energy stored in the machine [105]. Under the hypothesis of infinite permeability, no energy is stored in the ferromagnetic core. Therefore, the magnetic energy ( $W_m$ ) is

$$W_m(\theta_m) = W_g(\theta_m) + W_b(\theta_m). \quad (2.18)$$

where  $W_g(\theta_m)$  is the energy stored in the air-gap and  $W_b(\theta_m)$  is the energy stored in the flux barrier, (2.19) and (2.20), respectively.

$$W_g(\theta_m) = \frac{l_{\text{axial}} R g}{2\mu_0} \int_0^{2\pi} [B_g(\theta_s, \theta_m)]^2 d\theta_s \quad (2.19)$$

$$W_b(\theta_m) = p [R_b(\phi_b(\theta_m))]^2 \quad (2.20)$$

In this case, the torque is calculated by (2.21). The first term is the average torque, calculated by (2.17). The second term represents the torque ripple, the pulsating component of the torque, obtained from the magnetic energy stored in the machine, (2.22).

$$T_{\text{em}}(\theta_m) = T_{\text{avg}}(\theta_m) + T_{\text{rp}}(\theta_m) \quad (2.21)$$

$$T_{\text{rp}}(\theta_m) = -\frac{\partial W_m}{\partial \theta_m} \quad (2.22)$$

As can be seen, the pulsating component depends on the magnetic flux density distribution in the air-gap, which is a function of the position of the rotor flux barriers and the stator slotting. Therefore, it is possible to analyze the effect of both parameters on the torque waveform from the stored energy method, which is compared to the one resulting from FEM simulations as shown in Figure 2.8. It can be noted from Figure 2.8 (a) that the oscillation trends obtained in AM is consistent with FEM. In the same way that the flux density in the air-gap was analyzed, the harmonic distribution for the torque was obtained. From Figure 2.8 (b), the AM overestimates the fundamental harmonic component of the electromagnetic torque, which was to be expected since the torque is obtained from two methods that depend on the air-gap flux density. The behavior of the rest of the harmonic components in AM is the same as that obtained from FEM.

Figure 1.8 shows that the model can predict the ripple torque with good accuracy. Table III shows that the absolute error for the average torque and the ripple torque is 0.303 N·m and 0.903 N·m, respectively. These errors can be considered acceptable. The main cause of this difference is the assumptions made throughout the development of the AM and the fact that the effect of tangential flux density is neglected in the torque calculation.

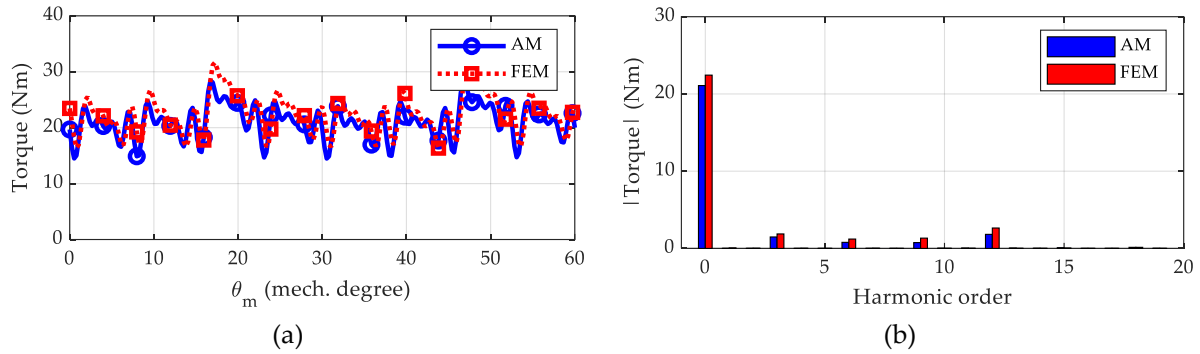


**Figure 2.8.** Electromagnetic torque waveform for two torque ripple periods with slotting effect. (a) torque waveform; (b) torque harmonic components.

#### 2.4. Extension of the method to machines with a larger number of flux barriers per pole

An increased number of flux barriers per pole leads to greater rotor anisotropy, which results in a higher magnetic saliency, the primary metric for evaluating the performance of a SynRM. The saliency refers to the ratio between the inductance of the direct and quadrature axes. By increasing the number of barriers, the reluctance of the quadrature axis is altered, which modifies the saliency and enhances machine performance.

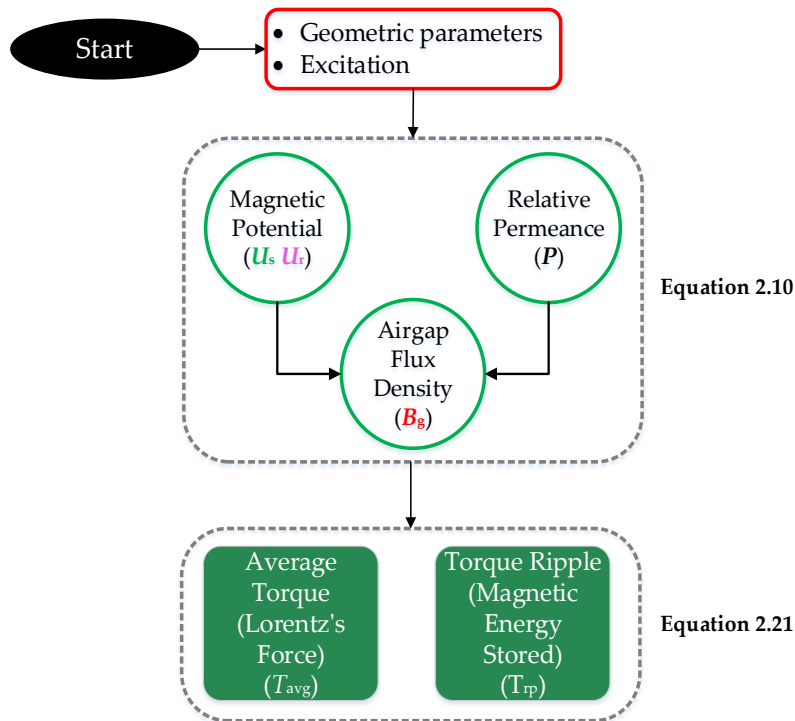


**Figure 2.9.** Analytical method workflow.

The extension of the method is necessary to evaluate machines with better performance characteristics and to generalize the approach to any number of flux barriers. It is presented following the procedure described above for one flux barrier per pole, considering that the magnetic potential of each barrier is the result of the flux crossing the barrier, and this is only present in the barrier island. For the sake of clarity, a more intuitive representation of the method adopted, the

workflow adopted is shown in Figure 2.9. Following this procedure, the air-gap magnetic flux density and torque were calculated when the rotor structure has two, three, four, five, and six flux barriers per pole. It is chosen to compute up to six flux barriers per pole because this is the optimum number of flux barriers per pole for a stator configuration with 48 slots [3], [106]. The comparison with FEM is shown in Figure 2.10 for flux density and torque. It is important to note that the higher the number of flux barriers the more parameters must be analyzed, and therefore the model's accuracy may decrease.

The flux density shows a good agreement with FEM for any of the cases analyzed. Figure 2.10 shows the comparison for  $\theta_m = 0$ , but for any rotor position analyzed, the results are equally satisfactory. The flux density curves clearly show the effect of flux barriers and stator slots.

On the other hand, Figure 2.11 shows that the torque behavior is agreement to the one obtained in FEM; the average torque values, torque ripple, and absolute error are shown in Table 2.3. This metric compares the absolute difference between the FEA values and the values predicted by the analytical model. The torque ripple results are less accurate than the average torque, as indicated by the mean absolute error. However, the analytical model achieves an error of less than one with respect to the FEA results, which indicates a good prediction of the phenomenon.

**Table 2.3.** Average torque and torque ripple for different rotor configurations.

Barrier number	Analysis method & error	$T_{avg}$ (Nm)	$T_{rp}$ (Nm)
1	FEM	21.03	15.37
	AM	21.33	14.50
	Absolute error	0.30	0.90
2	FEM	21.49	14.03
	AM	22.82	13.61
	Absolute error	1.32	0.42
3	FEM	21.49	24.66
	AM	22.84	20.90
	Absolute error	1.35	3.75
4	FEM	21.44	13.14
	AM	22.18	13.02
	Absolute error	0.74	0.12
5	FEM	20.70	13.03
	AM	21.61	12.86
	Absolute error	0.91	0.17
6	FEM	20.72	12.45
	AM	21.21	11.92
	Absolute error	0.49	0.53
Mean Absolute Error		<b>0.85</b>	<b>0.98</b>

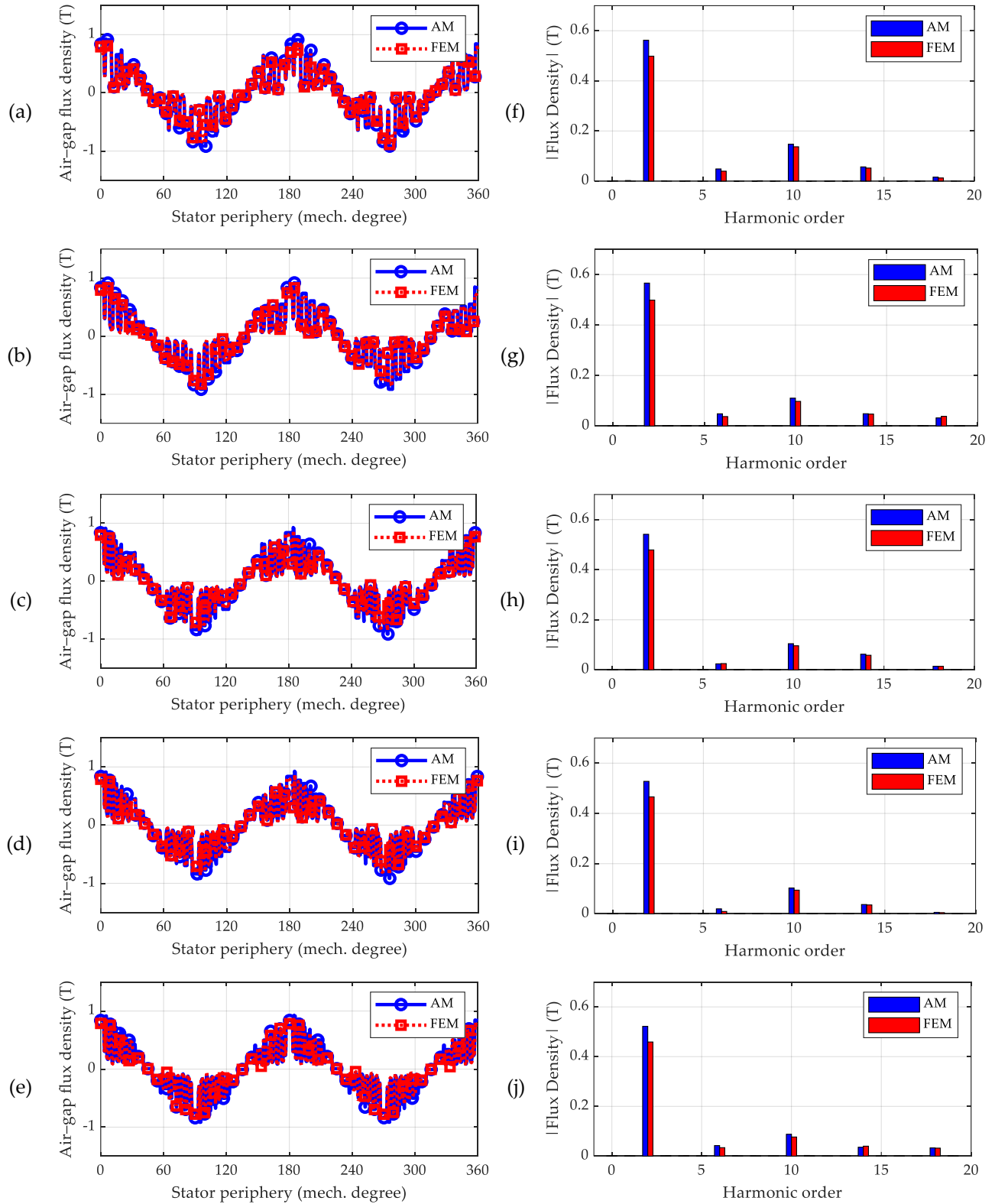


**Figure 2.10.** Air-gap flux density waveform for  $\theta_m = 0$  for different rotor configuration and the harmonic components. (a, f) two barriers per pole; (b, g) three barriers per pole; (c, h) four barriers per pole; (d, i) five barriers per pole; (e, j) six barriers per pole torque ripple periods.

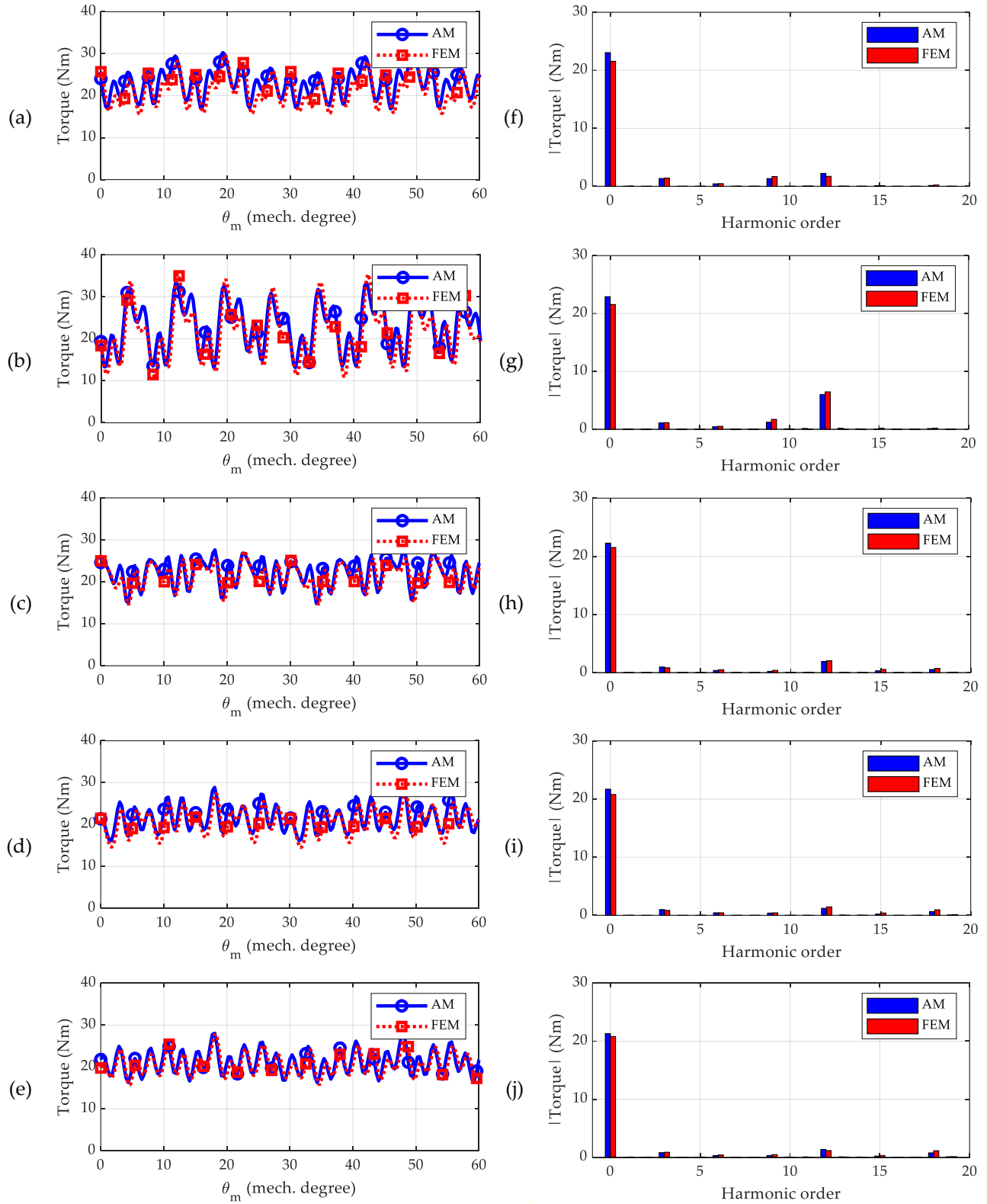


**Figure 2.11.** Electromagnetic torque waveform for different rotor configuration and the harmonic components. (a, f) two barriers per pole; (b, g) three barriers per pole; (c, h) four barriers per pole; (d, i) five barriers per pole; (e, j) six barriers per pole torque ripple periods.

Despite this, the AM proposed shows an acceptable behavior; of the six rotor structures analyzed, the rotor with three flux barriers per pole shows the highest error in the torque calculation. Moreover, the variation trend of the torque waveform obtained by both methods is consistent. It is also observed from Table 2.3 that in all cases the average torque value is higher in the analytical model. The assumption that the permeability of the ferromagnetic material is infinite leads to ignore the magnetic saturation of the cores iron and hence the average torque will be overestimated. This occurs because in the FEM model the permeance has a very large value to simulate the infinite permeance assumed in the analytical model, but despite this, it is a finite value and small drops of potential are affecting the results.

### 2.5. Parameters on the d-q reference frame

According to [107] the Winding Function (WF) for an arbitrary phase "i" and its corresponding Fourier Series can be calculated from equation (2.25); for this analysis the windings are assumed to be stationary, only depending on  $\theta_s$ . Figure 2.12 shows the winding function for each phase of the machine under analysis.

$$N_i(\theta_s) = \sum_{n=1,3,5,\dots}^{\infty} \frac{4N_t k_{wn}}{pn\pi} \cos \left[ pn \left( \theta_s - k \frac{2\pi}{pm} \right) \right] \quad (2.25)$$

where  $k=0, 1, 2, \dots$  for phases A, B, C...,  $p$  represents the pole pairs,  $m$  the number of phases and  $n$  the order of the harmonic,  $N_t$  the number of turns per phase per pole,  $k_{wn}$  is the winding factor for harmonic  $n$  and it is calculated as follows,

$$k_{wn} = k_{dn} k_{pn} k_{xn} \quad (2.26)$$

$$k_{dn} = \frac{\sin \left( \frac{n\pi}{2m} \right)}{q \sin \left( \frac{n\pi}{2qm} \right)} \quad (2.27)$$

$$k_{pn} = \sin \left( n \frac{\pi W}{2 \tau_p} \right) \quad (2.28)$$

$$k_{xn} = \sin \frac{\left( \frac{nb_{ss}}{2} \right)}{\frac{nb_{ss}}{2}} \quad (2.29)$$

where  $q$  is the number of slots per phase per pole,  $W$  is the width of the winding,  $\tau_p$  is the polar pitch y  $b_{ss}$  is the slot opening.

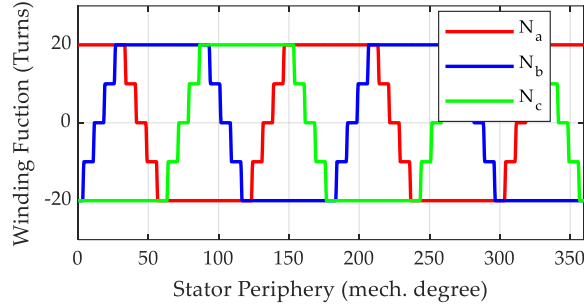


**Figure 2.12.** Winding function for a four pole SynRM.

The flux linkages can be calculated as the multiplication of the flux density by the cross-sectional area, generalizing this to a three-phase machine the flux linkages for an arbitrary phase “ $i$ ” can be calculated as

$$\lambda_i(\theta_m) = \int_0^{2\pi} B_g(\theta_m, \theta_s) N_i(\theta_s) dA \quad (2.23)$$

$$dA = R l_{\text{axial}} d\theta_s \quad (2.24)$$

When the Clarke-Park’s transformation is applied to these flux linkages like in the Chapter I, the flux linkage on the  $d$ - $q$  axes is obtained as follows

$$\lambda_d = \frac{2}{3} \left[ \lambda_a \cos(\theta_m) + \lambda_b \cos\left(\theta_m - \frac{2\pi}{3}\right) + \lambda_c \cos\left(\theta_m - \frac{4\pi}{3}\right) \right] \quad (2.30)$$

$$\lambda_q = \frac{2}{3} \left[ \lambda_a \sin(\theta_m) + \lambda_b \sin\left(\theta_m - \frac{2\pi}{3}\right) + \lambda_c \sin\left(\theta_m - \frac{4\pi}{3}\right) \right]. \quad (2.31)$$

Once the flux linkages are obtained in  $d$ - $q$  reference frame the inductances and the average torque developed by the machine can calculate by (1.4). The comparison with FEM is shown in Figure 2.13 showing a correct prediction of the AM for the flux linkage in both reference frame. On the other hand, the mean torque values are shown in Table 2.4. The main differences in the results are due to the assumptions that were considered during the development of the AM and the stator leakage inductance are neglected.

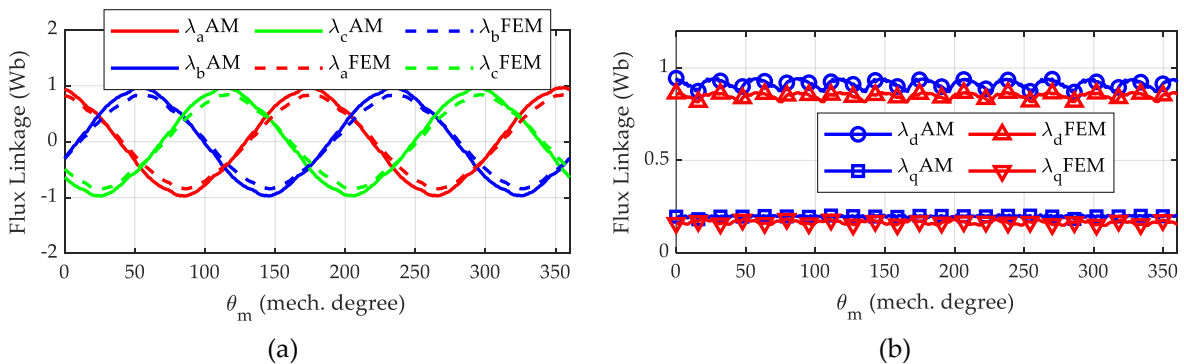


**Figure 2.13.** Flux linkage for a four pole SynRM. (a) flux linkage for the  $abc$  reference frame; (b) flux linkage for the  $d$ - $q$  reference frame.

**Table 2.4.** Mean torque comparison between FEM and AM.

<b>Analysis method</b>	<b>T<sub>em</sub> (Nm)</b>
FEM	20.5
AM	21.5

### 2.6. Summary

This chapter presents the development of an AM to evaluate the performance of a SynRM that combines two methods proposed by the research community as possible ways to be adopted for the analysis of SynRMs. The method including the slotting effect in a relatively simple way in the torque wave and with equations that allow to analyze how each parameter affects the result. In addition, it provides the possibility that the parameters can be freely and easily modified for further optimization. The analysis process is explained in detail for a machine configuration with one flux barrier per pole and subsequently extended for machines with a larger number of barriers.

Even though the assumptions were made throughout the development of the method, the comparison with FEM shows satisfactory results, both for air-gap flux density and torque. To validate the method, several FEM simulations were performed for different machine configurations where the dimensions and the electrical steel used were changed. In all analyses the AM shows a correct prediction of the machine behavior until the machine starts to operate above the saturation knee of the B-H curve. The analyses carried out allow us to affirm that the analytical model gives sufficiently accurate results when the machine is operated in the linear zone of the B-H curve.

The harmonic analysis showed that the AM overestimates the air-gap flux density and the electromagnetic torque. This difference is mainly due to the assumptions that were adopted during the development of AM, i.e., by not considering the nonlinearities in the machine. The remaining harmonics components in the AM shows the same behavior as that obtained from the FEM. There is another factor that also affects the torque results and that is that the tangential flux density is neglected, being the model with the highest deficiency the one with three flux barriers per pole.

It is also important to mention that for the application of the AM it was necessary to assume certain conditions that are mentioned at the beginning of the chapter, which limits its application to low-speed purposes. In practice, radial and tangential barrier bridges are necessary for mechanical reasons. Considering these as air is a good assumption, but ignoring these bridges also leads to a small overestimation of the average torque.



### Chapter III: Rotor asymmetric impact on Synchronous Reluctance Machine Performance

This chapter examines the impact of an asymmetric rotor design on the performance of a SynRM using FEM. The analyzed rotor has a simple structure, featuring two flux barriers per pole, optimized through a multi-objective optimization algorithm. The rotor design exhibits asymmetry along the q-axis, but each machine pole is identical, resulting in circumferential symmetry.

#### 3.1. Modelling of the SynRMs under analysis

##### 3.1.1. Sizing method

In this study, a 12kW@1500rpm SynRM with a two-pole-pair was designed to investigate the potential benefits of an asymmetrical rotor design. The machine was sized using a specific methodology [108], and features a stator with 48 slots and three-phase distributed windings (Figure 3.1), as well as a rotor with two flux barriers per pole. The ferromagnetic material used in the stator and rotor cores is M19-29G. The main dimensions of the machine are outlined in Table 3.1. It is well known that torque ripple in SynRMs is influenced by the interaction between the spatial harmonics of the magnetomotive force caused by stator currents and the rotor geometry. Research [109] and [102] have shown that the position of the flux barriers is a key factor in reducing torque ripple in SynRMs, and thus is the primary variable to be analyzed in this study. The topology of the machine under study is shown in Figure 3.1 together with the rotor parameterization.

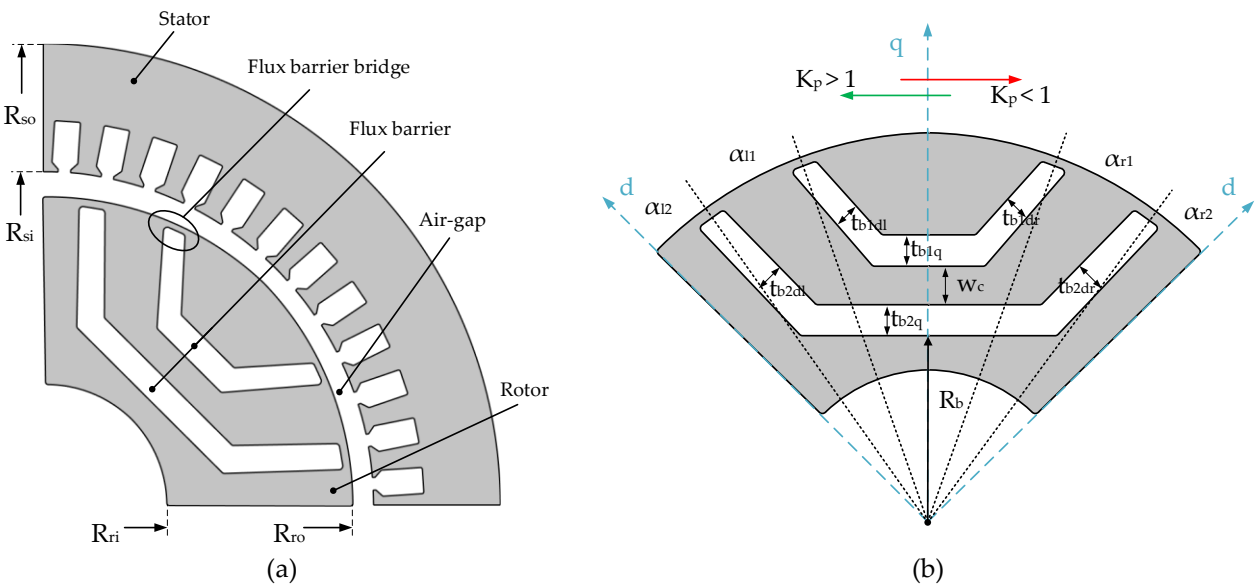


**Figure 3.1.** Machine topology. a) stator and rotor; b) rotor parametrization.

**Table 3.1.** Design parameters

Parameter	Symbol	Quantity	Unit
Stator outer diameter	$D_{so}$	346.7	mm
Stator inner diameter	$D_{si}$	245.2	mm
Rotor outer diameter	$D_{ro}$	244	mm
Rotor inner diameter	$D_{ri}$	70	mm
Air-gap length	$g$	0.6	mm
Axial length	$l_{axial}$	172	mm
Slot pitch	$\tau_s$	7.5	mechanical degree
Slot open	$b_{ss}$	1.4	mechanical degree
Turns per slot	$N_s$	10	-
Slots numbers	$Q_s$	48	-

### 3.1.2. Optimization process

From the preliminary sizing described above, a design refinement stage is carried out to optimize two objective functions: maximize torque production and minimize torque ripple. The air-gap length, the inner and outer diameters of the stator and rotor are geometrical constraints.

The objective variables are set only on the rotor geometry, such as the position of flux barriers concerning the  $d$ -axis ( $\alpha_{rn}$ ,  $\alpha_{ln}$ ), flux barrier opening ( $l_{brn}$ ,  $l_{bln}$ ), flux barrier width ( $t_{bn}$ ), the separation between the barriers ( $w_c$ ) and the radius to the center the most inner barrier ( $R_b$ ).

The optimization was implemented in ANSYS commercial software package using a Multi-Objective Genetic Algorithm (MOGA). Rotor geometry was parameterized in a CAD software included in the ANSYS package and FEM analysis was performed in ANSYS Electronics Desktop. MOGA is defined with an initial number of 150 samples with a maximum of 35 iterations; 100 designs were analyzed per iteration. The symmetric design converged after 2087 evaluations, and the asymmetric after 2623. This analysis allows to obtain the anisotropic structure of the rotor that fulfills the objective functions.

Figure 3.2 shows the optimization process workflow, and the range of input variables is shown in Table 3.2. The model was supplying with 10 A/mm<sup>2</sup> during the optimization; this current value corresponds to approximately 2 times the rated current. Choosing a current value between 2 and 3 times the rated current ensures that the torque ripple is less sensitive to load variations [110], [111]. On the other hand, the current angle is adjusted according to the objective functions for MTPA.

The insulation ratio, which is defined as the ratio between thickness of total insulation ( $t_{b1} + t_{b2}$ ) over total length ( $(D_{ro} - D_{ri})/2$ ) inside the rotor, by (3.1). This parameter attempts to represent the feature of the machine anisotropic structure quality. The insulation ratio has a great impact on the torque production; therefore, in order to determine the performance characteristics of the machine are only affected by the possible asymmetry in the rotor structure, this parameter is the same for both designs in the optimization process.

$$k_{air} = \frac{t_{b1} + t_{b2}}{(D_{ro} - D_{ri})/2} \quad (3.1)$$

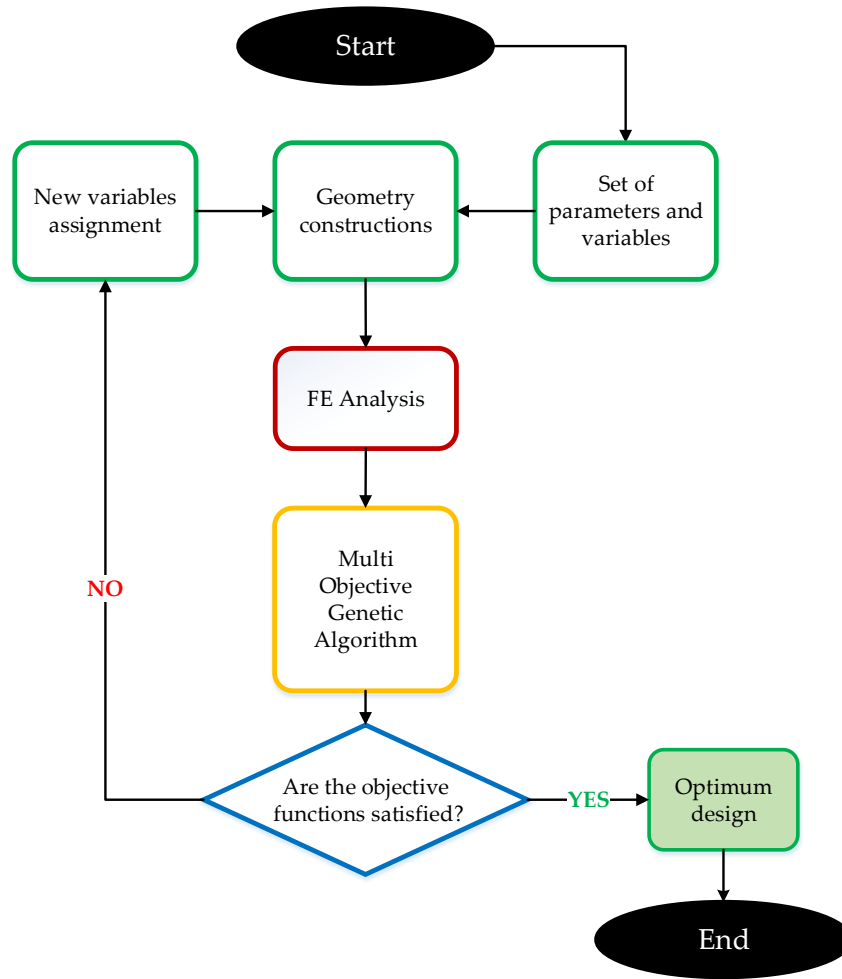


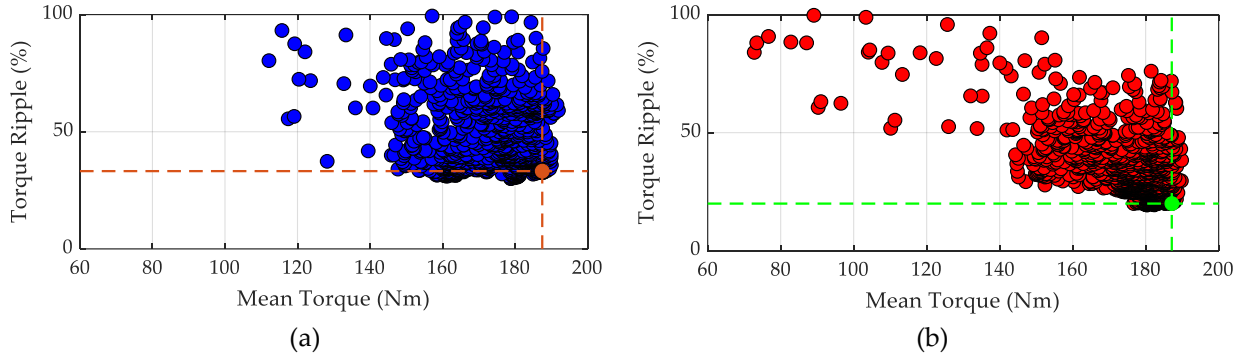
Figure 3.2. Optimization process workflow.

Table 3.2. Input variables range.

Parameter	Symbol	Boundaries		Unit
		Lower	Upper	
Flux barrier angle 1 (right)	$\alpha_{r1}$	1	30	mechanical degree
Flux barrier angle 2 (right)	$\alpha_{r2}$	1	30	mechanical degree
Flux barrier angle 1 (left)	$\alpha_{l1}$	1	30	mechanical degree
Flux barrier angle 2 (left)	$\alpha_{l2}$	1	30	mechanical degree
Flux barrier opening 1(right)	$l_{br1}$	2	10	mechanical degree
Flux barrier opening 2(right)	$l_{br2}$	2	10	mechanical degree
Flux barrier opening 1(left)	$l_{bl1}$	2	10	mechanical degree
Flux barrier opening 2(left)	$l_{bl2}$	2	10	mechanical degree
Flux barrier width 1	$t_{b1}$	10	22	mm
Flux barrier width 2	$t_{b2}$	10	22	mm
Width between barriers 1-2	$w_c$	2	10	mm
Current Angle	$\alpha_i^e$	45	75	electrical degree
Inner barrier radius	$R_b$	40	50	mm

### 3.1.3. Optimum Designs

For the symmetric model, the position and opening of the flux barriers on the left side remain the same as those on the right side, while in the asymmetric model, they can take any value within the set limits. The optimization results are presented in Figure 3.3 for the symmetric (a) and asymmetric (b) models. The rotor structure data and the current angle for the optimal designs are shown in Table 3.3.



**Figure 3.3.** Designs obtained from the optimization process for a 4-pole machine with two flux barriers per pole. The current was fixed to  $\sim 10$  A/mm<sup>2</sup> and the current angle was defined in the optimization algorithm for MTPA. (a) symmetric design; (b) asymmetric design. The selected designs are highlighted on the figure.

**Table 3.3.** Geometric values for optimal symmetrical and asymmetrical designs.

Parameter	Symbol	Symmetric design	Asymmetric design	Unit
Flux barrier position index	$K_p$	1	1.42	-
Flux barrier opening index	$K_w$	1	1.65	-
Flux barrier width 1	$t_{b1}$	21.16	17.90	mm
Flux barrier width 2	$t_{b2}$	11.81	14.95	mm
Width between barriers 1-2	$w_c$	8.39	9.25	mm
Deeper radio barrier	$R_b$	48.77	47.70	mm
Insulation ratio	$k_{air}$	0.38	0.38	-
Current angle	$\alpha_e^1$	60.56	61.95	°

To characterize the level of asymmetry of the designs, the following coefficients,  $K_p$  and  $K_w$ , are introduced. The first index ( $K_p$ ) is the ratio between the barrier angles and the second ( $K_w$ ) is the ratio between the barrier opening angles. Equations (3.2) and (3.3) show how these indices are calculated for a  $i$ -th barrier.

$$K_{p_i} = \frac{\alpha_{r_i}}{\alpha_{l_i}} \quad (3.2)$$

$$K_{w_i} = \frac{l_{r_i}}{l_{l_i}} \quad (3.3)$$

When the machine is symmetrical these indices are equal to one, both sides of the magnetic pole have the same dimension. If the design is asymmetrical, both  $K_{p_i}$  and  $K_{w_i}$  can be greater or less than one. To characterize the possible displacement of the machine's  $q$ -axis because of asymmetry, it will be classified as positive or negative according to the value of  $K_{p_i}$ . If  $K_{p_i} > 1$  the asymmetry will

be positive, and the q-axis will be displaced in a leftward direction and if  $K_{p_i} < 1$  the symmetry will be negative, and the q-axis will be displaced to the right as shown in Figure 3.1 (b).

To increase the anisotropy in SynRMs, it is common that the rotor has more than one flux barrier per pole, in this case the indexes are calculated as follows, where  $n$  is the number of flux barriers per pole of the rotor.

$$K_p = \frac{\sum_{i=1}^n K_{p_i}}{n} \quad (3.4)$$

$$K_w = \frac{\sum_{i=1}^n K_{w_i}}{n} \quad (3.5)$$

### 3.2. Results analysis

Both designs were analyzed using ANSYS Electronics Desktop, a commercial software package. The analysis involved variations in rotation direction (clockwise and counter-clockwise) and operating conditions (current angle ranging from 25-85 degrees and current density from 0-10 A/mm<sup>2</sup>) in order to evaluate the behavior of the designs under different scenarios.

#### 3.2.1. Saliency ratio

The variation of the saliency ratio for symmetrical and asymmetrical designs as a function of current angle and current density is shown in Figure 3.4. It can be observed that the symmetric design shows higher saliency values than the asymmetric design for a value of the current angle less than 60 electrical degrees, when exceeding this value, the asymmetric design shows better saliency. In general, the highest saliency values are achieved for both designs when the machine begins to be saturated and for high current angle values.

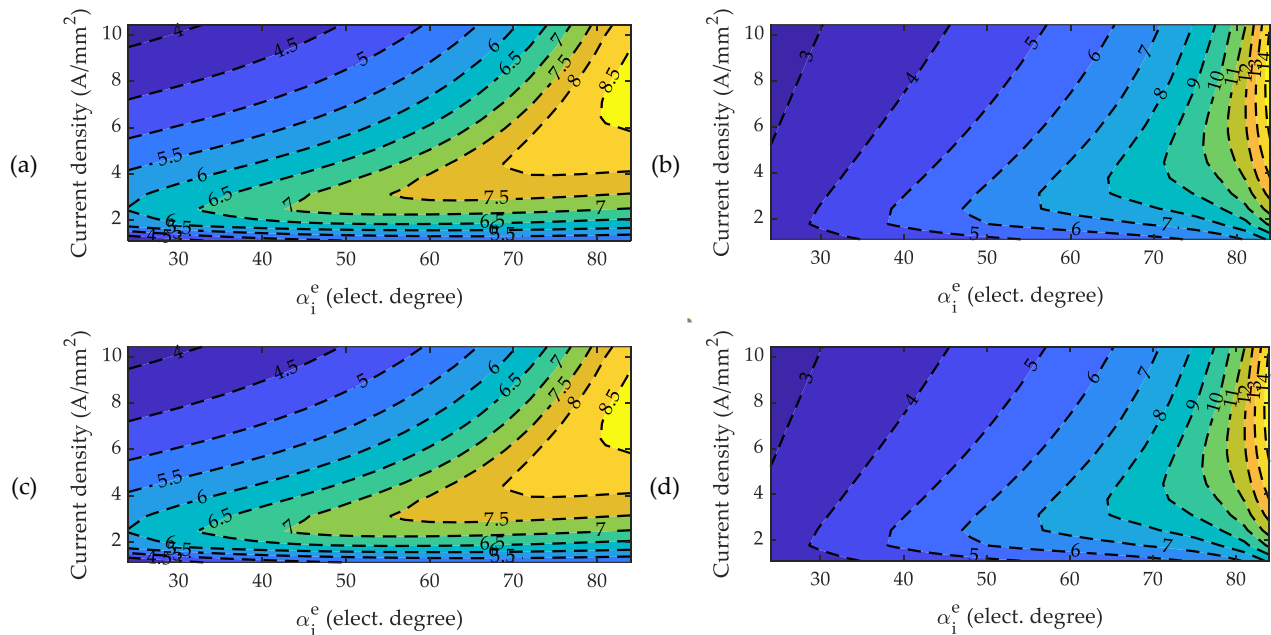


**Figure 3.4.** Saliency ratio as a function of the current density and the current angle. (a) symmetric design counter-clockwise; (b) asymmetric design counter-clockwise; (c) symmetric design clockwise; (d) asymmetric design clockwise.

The saliency ratio ( $\xi$ ) is used to evaluate the SynRM performance. As mentioned in Chapter I, for a fixed value of current the  $q$ -axis inductance presents a small variation associated with the change in the current angle. When the machine is operated beyond the knee of the B-H curve the  $q$ -axis inductance can be considered constant, while the  $d$ -axis inductance continues to reduce. On the other hand, the  $d$ -axis inductance presents greater variations as the current angle changes, for a higher current angle the value of the  $d$ -axis inductance will be higher. Therefore, if the current angle increases the  $q$ -axis inductance remains constant and the  $d$ -axis inductance increases, and the saliency ratio of the machine increases as the current angle increases. This behavior in the inductance is caused by the saturation and cross-coupling between the  $d$ -axis and  $q$ -axis.

### 3.2.2. Maximum internal power factor

Figure 3.5 shows the IPF behavior in both designs for different values of current and current angle. Given the dependence between IPF and saliency ratio (equation 1.8), the behavior of both indices is similar, the symmetric design shows higher power factor than the asymmetric design for a value of the current angle less than 60 electrical degrees, when exceeding this value, the asymmetric design shows better power factor reaching values above 0.8.

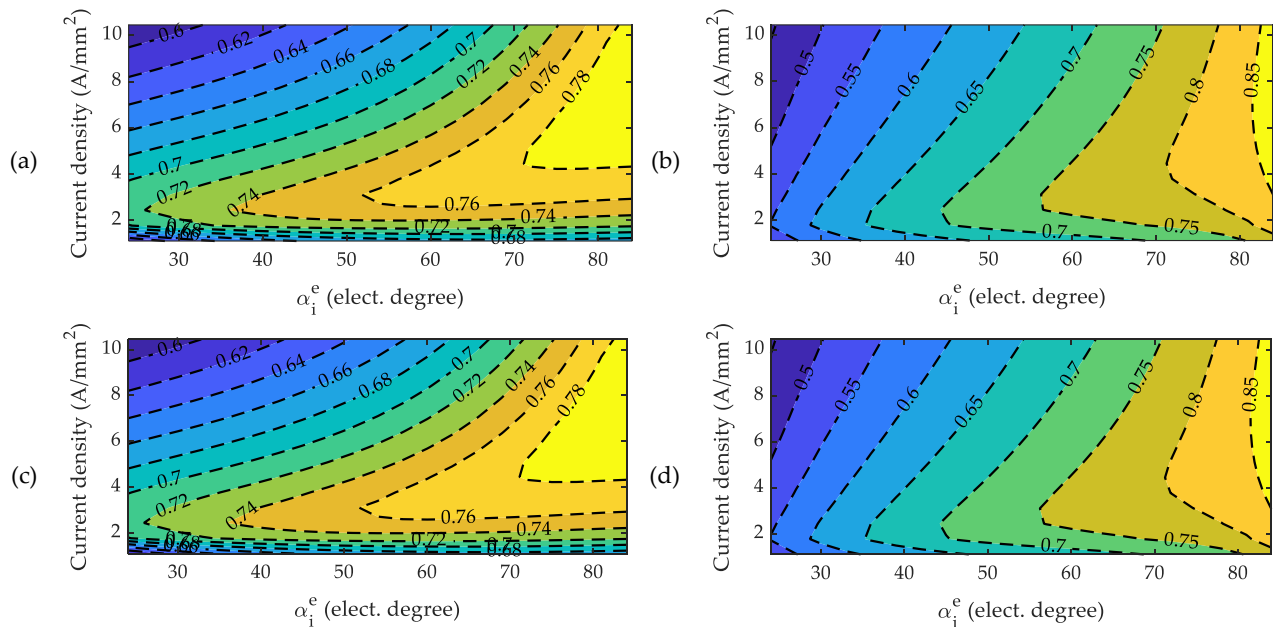


**Figure 3.5.** Internal power factor as a function of the current density and the current angle. (a) symmetric design counter-clockwise; (b) asymmetric design counter-clockwise; (c) symmetric design clockwise; (d) asymmetric design clockwise.

### 3.2.3. Electromagnetic torque

Figure 3.6 illustrates the behavior of electromagnetic torque for both symmetrical and asymmetrical designs as a function of current density and current angle. Neglecting saturation, a SynRM achieves its maximum torque value at a current angle of 45 electrical degrees. However, as saturation occurs, the current angle for maximum torque increases above 45 electrical degrees. The impact of saturation can be easily observed in the torque contour curves (Figure 3.6) for both designs. As the current density increases, the current angle for maximum torque also increases.

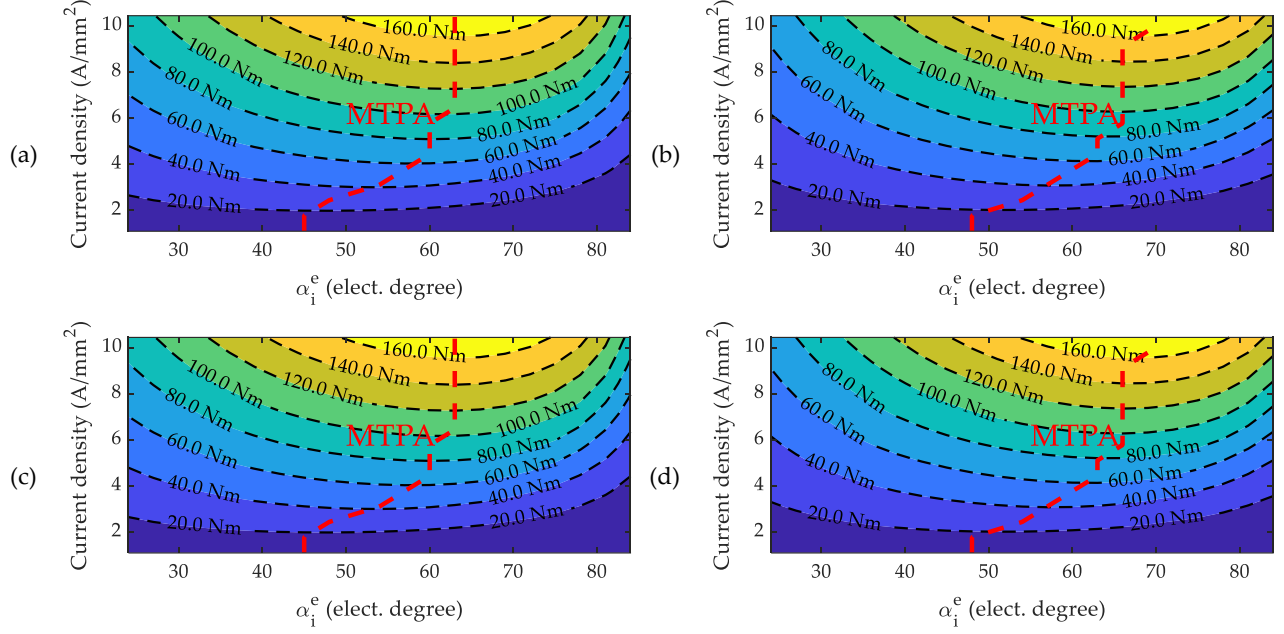


**Figure 3.6.** Electromagnetic torque as a function of the current density and the current angle. MTPA trajectory is highlighted in red. (a) symmetric design counter-clockwise; (b) asymmetric design counter-clockwise; (c) symmetric design clockwise; (d) asymmetric design clockwise.

In the asymmetric design this effect is a is slightly more evident because the asymmetry generates a shift in the  $q$ -axis of the machine. In a symmetric design,  $d$ -axis inductance is obtained when aligning the  $a$ -phase symmetry axis with the rotor  $d$ -axis and supplying the  $a$ -phase with current that has a current angle of 45 electrical degrees ( $\alpha_i^e = 45^\circ$ ) and the maximum torque is obtained. In the case of an asymmetric rotor, repeating this procedure does not provide the maximum torque since the  $q$ -axis and  $d$ -axis are shifted as a result of the asymmetry. Accordingly, for the proposed asymmetrical design, the maximum torque is obtained for a larger current angle than in the symmetrical design. This increase in the current angle to obtain the maximum torque makes it possible that when the machine operates at MTPA the salience presented by the machine is higher, despite this advantage, the asymmetric model is not able to develop a higher torque than the symmetric design since the  $\sin 2\alpha_i^e$  begins to decrease when the current angle is greater than 45 electrical degrees.

### 3.2.4. Torque ripple

The primary advantage of the asymmetric design over the symmetric design is the significant reduction in torque ripple. Figure 3.7 illustrates the torque ripple behavior for both designs at various current and current angle values. When following an MTPA trajectory, the asymmetric design consistently exhibits the lowest torque ripple value, as shown in Figure 3.7. Adhering to this control strategy, the asymmetric design consistently demonstrates a torque ripple lower than 20%, while the symmetric design exhibits a torque ripple higher than 20%, reaching as high as 30% at specific operating points. These torque ripple values are further discussed in the following section.

One of the main contributors for the large torque ripple in SynRM is the interaction of spatial harmonics of the MMF generated by stator currents and rotor geometry [14]. High torque ripple generates vibrations that can cause higher acoustic noise and impact the current harmonics. Moreover, in high-performance applications, low torque ripple is strictly required [15]. In this sense,

the reduction in torque ripple is mostly due to the asymmetric position of the rotor flux barriers, which allow some degree of mitigation of the spatial harmonics appearing in the air-gap.

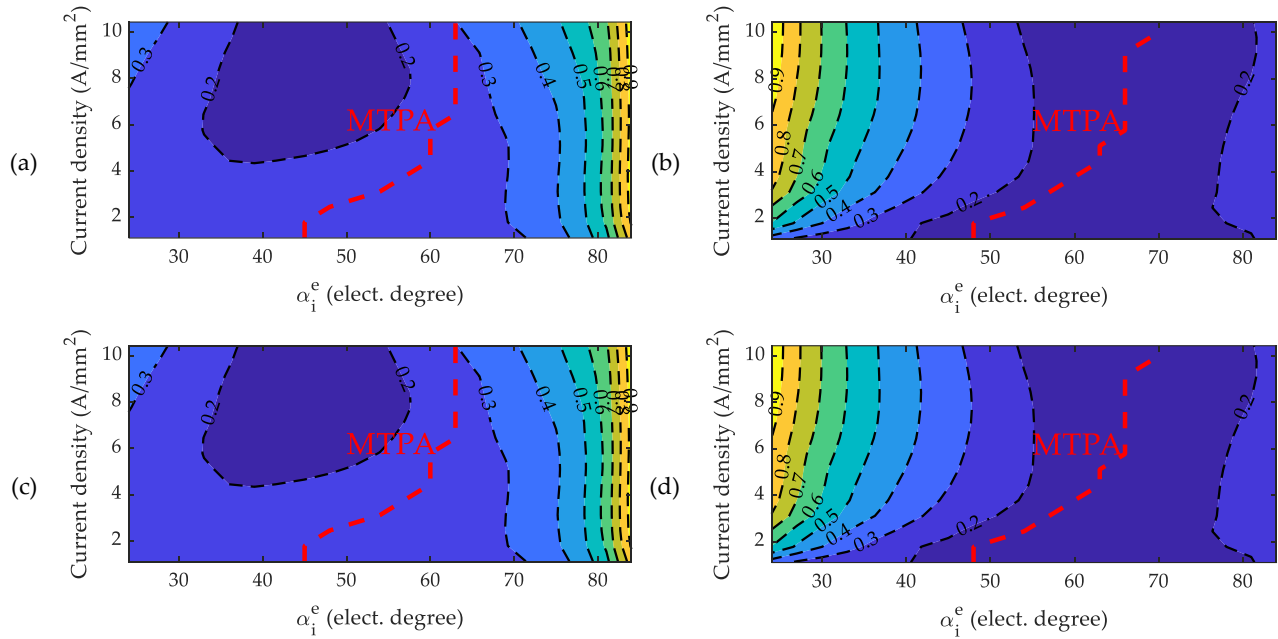




**Figure 3.7.** Torque ripple as a function of the current density and the current angle. MTPA trajectory is highlighted in red. (a) symmetric design counter-clockwise; (b) asymmetric design counter-clockwise; (c) symmetric design clockwise; (d) asymmetric design clockwise.

### 3.2.5. Additional discussion on efficiency and CPSR

In this section the designs will only compare when they rotate counter-clockwise, since, as it was observed in the previous sections, there are no considerable differences in the performance indexes according to the change of the direction of rotation. Figure 3.8 show the intersection of the contour curves of the internal power factor, torque ripple and the mean torque over a certain range of current density and current angle for the symmetric and asymmetric design, respectively. Two operating points in the MTPA trajectory corresponding to 5 A/mm<sup>2</sup> for the inverted blue triangle and 10 A/mm<sup>2</sup> for the red triangle have been highlighted in the figure. Table 3.4 provides the values of performance indexes for the operating points defined in Figure 3.8. The mean torque values are relatively similar between the symmetric and asymmetric designs. The asymmetric design demonstrates a 10% increase in power factor compared to the symmetric design. The most notable distinction between the symmetric and asymmetric designs can be found in torque ripple, where the asymmetric design offers a reduction of approximately 35% with respect to the symmetric one.

**Table 3.4.** Performance indices for the operating points defined in Figure 3.8 for the symmetrical and asymmetrical designs when the machine rotated counter-clockwise.

Operating point	Symmetric				Asymmetric			
	IPF	$T_{avg}$ [Nm]	$T_{rp}$ [%]	P [kW]	IPF	$T_{avg}$ [Nm]	$T_{rp}$ [%]	P [kW]
	0.7	80.4	24.2	12.6	0.8	78.2	16.2	12.3
	0.6	175.1	29.9	27.5	0.7	176.2	15.7	27.6



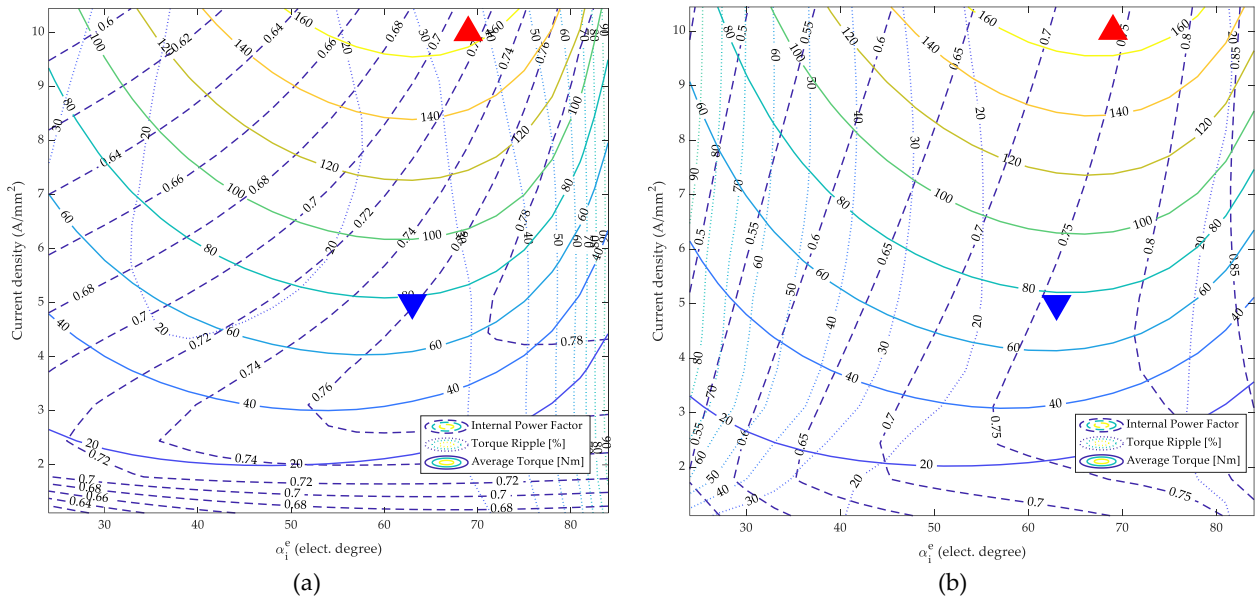


**Figure 3.8.** Electromagnetic torque and power factor as a function of the current density and the current angle for counter-clockwise rotation. (a) asymmetric design; (b) symmetric design.

To evaluate the performance of the designs under examination, an efficiency map was created for each design using the ANSYS Electronics Desktop's Machine-Toolkit. The analysis was performed using a line-to-line voltage of 380 V with a star connection and operated at MTPA with a maximum current density of 5 A/mm<sup>2</sup>. Figure 3.9 shows the result for the symmetrical and asymmetrical design for counter-clockwise rotation.

The most widely accepted approaches acknowledge that the constant power speed range (CPSR) largely depends on the saliency ratio [112]. Therefore, designing SynRM with enhanced saliency ratio can expand the application of this motor topology in various fields, such as electric vehicles. Figure 3.9 shows that the asymmetric design maintains nominal torque up to the nominal speed, whereas in the symmetric design, the torque begins to decrease at 1200 rpm, resulting in an 8% reduction of torque at the nominal speed. This is primarily due to the increased saliency ratio in the asymmetric design. In terms of efficiency, both designs exhibit a similar behavior, reaching 90% efficiency at the rated speed.

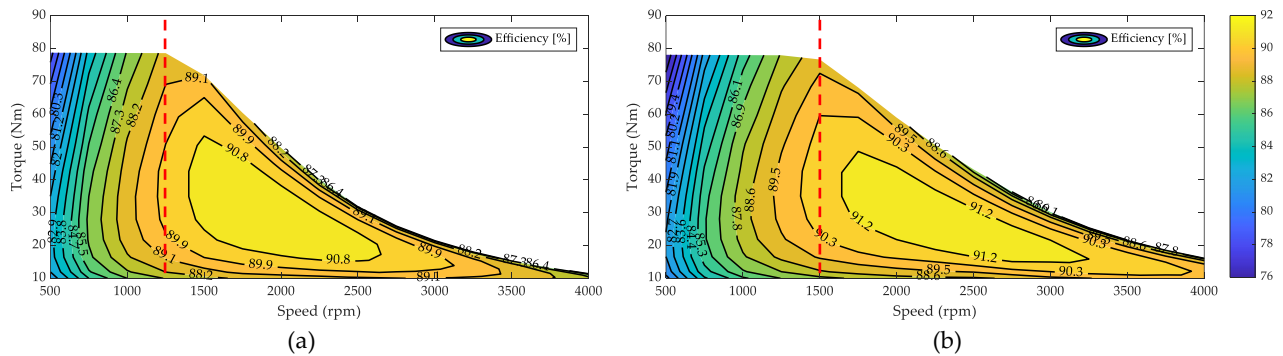


**Figure 3.9.** Efficiency map when the machine is operated a MTPA for a maximum current density of 5 A/mm<sup>2</sup> for counter-clockwise rotation. (a) symmetric design; (b) asymmetric design.

### 3.2.6. Sensitive analysis

After optimizing a design, it is important to conduct a sensitivity analysis to determine which variables have the greatest impact on the target functions. This analysis provides insight about potential errors that may occur during the manufacturing of a prototype. The ModeFRONTIER optimization program can be used to conduct the sensitivity analysis, which illustrates the relative significance of each component of the model based on its percentage contribution to overall variance.

The sensitivity analysis identifies the most crucial input variables by evaluating the main and interaction effects of factors on responses. Factors are inputs that affect changes in responses, while responses are outputs that are often dependent variables. Based on the sensitivity analysis results, certain variables may be eliminated in future optimizations to reduce computational effort and gain a deeper model understanding.

The key factors of the rotor structure that affect the average torque and torque ripple are the length, width, and location of the flux barriers [113]. The insulation ratio and current angle play a significant role in the average torque developed by the machine. Since the insulation ratio is kept constant between the two designs and the current angle is adjusted for maximum torque, the average torque is the same for both designs and no sensitivity analysis was conducted for this performance metric.

Figure 3.10 shows the relative significance of different terms on the torque ripple, specifically, the percentage of contribution of each term to the overall variance. The analysis focuses solely on the torque ripple and how the position and opening of the flux barriers affect it. As shown in this figure, the position of the flux barriers has the most significant influence on torque ripple in both designs. The increased degree of freedom in the asymmetric model allows for a smaller contribution of the position of each barrier to the overall variance than in the symmetric model. This results in a significant reduction of torque ripple in an asymmetric design, as well as an improvement in other performance indices such as average torque, power factor and CPSR.

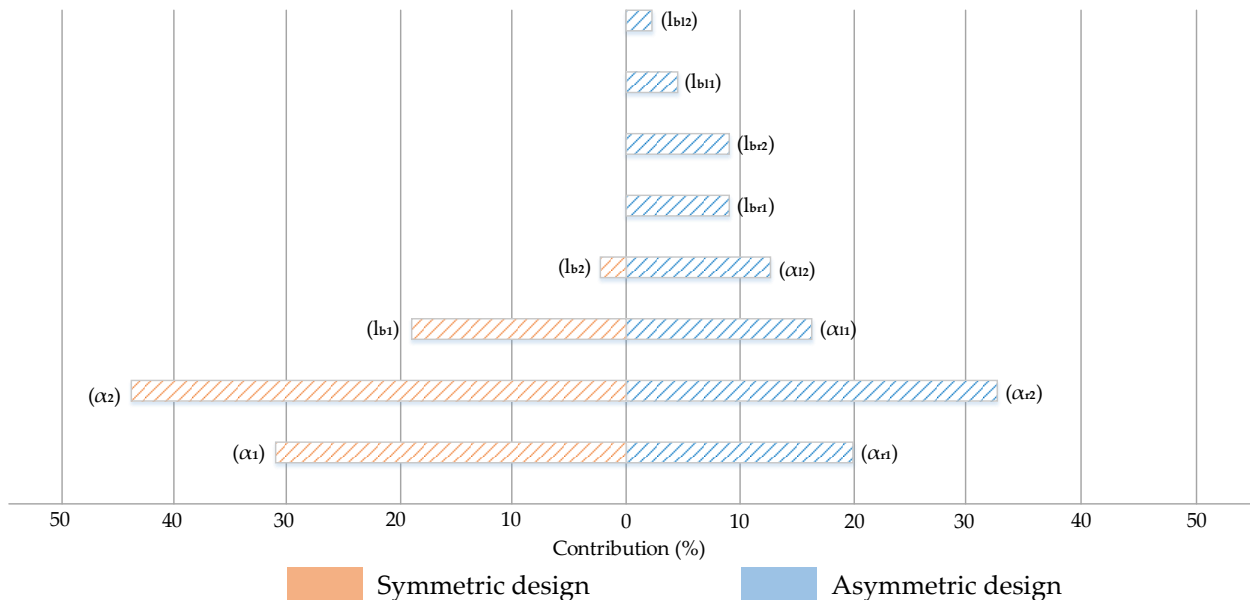


**Figure 3.10.** Percentage of contribution of each term to the global variance. Influence of barriers position ( $\alpha_{rn}$  and  $\alpha_{ln}$ ) and opening ( $l_{rn}$  and  $l_{ln}$ ) on torque ripple for both designs.

### 3.3. Summary

The proposed asymmetrical rotor topology for a SynRM demonstrates improved performance, specifically a 35% reduction in torque ripple at a specific operating point without a decrease in average torque compared to the symmetrical design. The asymmetric design also presents a lower torque ripple throughout the entire MTPA trajectory. FEM analysis confirms that the improvement is given by the asymmetrical positioning of the rotor flux barriers, which enhances the saliency ratio of the machine and reduces space harmonics in the air-gap. Additionally, the IPF increases by 10% in the asymmetric design in comparison to the symmetric design. The efficiency values for both designs are similar, but the asymmetric design can achieve the rated torque up to the rated speed, resulting in a higher CPSR than the symmetric model. These performance improvements indicate that incorporating asymmetry in the rotor's q-axis is a promising technique for reducing torque ripple and increasing power factor, which are significant drawbacks in this electric machine configuration.

## Chapter IV: A method to determine the torque ripple harmonic reduction in skewed Synchronous Reluctance Machines

This section presents a general analytical expression for multi-step discrete skewing in SynRM, which considers the impact on all torque harmonic components and offers a way to visualize the reduction of specific undesired harmonic content. To evaluate the expression's accuracy, two SynRM designs are analyzed through both two-dimensional (2D) and three-dimensional (3D) finite element analysis (FEA). The results show that 2D FEA is effective in predicting the optimal step skewing and the proposed expression is validated by the comparison between the 2D and 3D analysis. The proposed equations are applied to 2-step, 3-step, and 4-step skewing and yield promising results, demonstrating the ability to mitigate selected undesired harmonics and reduce other harmonic content as a side effect.

### 4.1. Selected machines

With the aim of giving insight of the procedures required to use the proposed N-step skewing analytical expressions, two SynRM machines are considered as a case study and assessed in this work, as presented in Figure 4.1(a) and Figure 4.1(b), respectively. Single-layer distributed windings are considered for both machines.

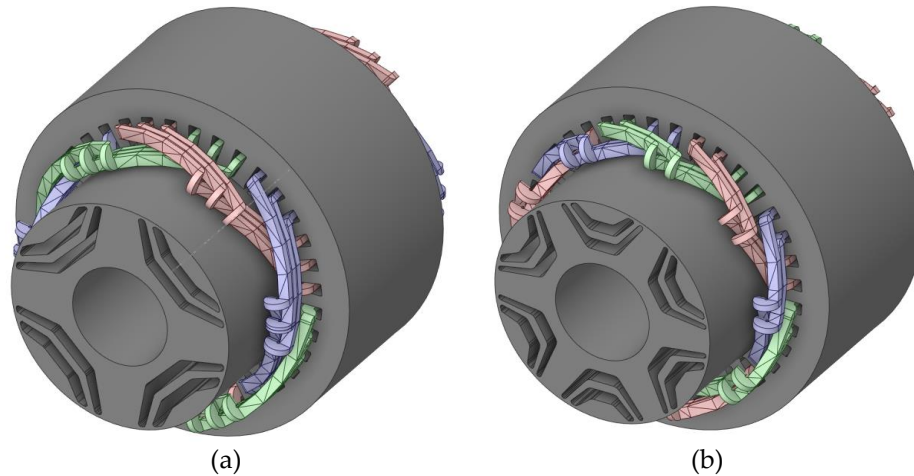


**Figure 4.1.** 3D sketches of (a) four-pole synchronous reluctance motor with two barriers per pole; (b) six-pole synchronous reluctance motor with two barriers per pole. Three-phase stator windings are highlighted in red, green, and blue, corresponding to each phase. Rotor in both machines is shown as an exploded view.

Several geometrical parameters of the rotor structure of SynRM can affect to different levels the performance of a SynRM. There are a number of design guidelines established in the literature to choose the number of flux barriers and poles. The number of parameters increase exponentially as the number of flux barriers per pole and pole pairs increase. SynRM is designed to maximize  $d$ -axis inductance and minimize  $q$ -axis inductance as this ensures that the machine's saliency ratio is large enough for the machines to achieve the required torque performance. On the one hand, to obtain a good saliency ratio, a small number of pole pairs is preferred, and the literature recommends to adopting two or three pole pairs [45]. On the other hand, the optimum number of flux barriers is defined according to the number of stator slots. For the case of a 36-slot machine, some authors do

not encourage to adopt more than three flux barriers. A greater number of barriers could jeopardize the mechanical integrity of the rotor or make the design process more complex [3], [106].

Therefore, in this paper two machines with two and three pole pairs are considered, and each pole features two barriers. The common data for all machines are presented in Table 4.1.

**Table 4.1.** Main data of the selected machines.

Parameter	Symbol	Value	Unit
Stator outer diameter	$D_{so}$	245	mm
Stator inner diameter	$D_{si}$	161.4	mm
Rotor outer diameter	$D_{ro}$	160.4	mm
Rotor inner diameter	$D_{ri}$	70	mm
Tooth height	$h_t$	22.8	mm
Tooth width	$b_t$	9	mm
Air-gap length	$g$	0.5	mm
Stack length	$l_{st}$	120	mm
Turns per slot	$N_s$	20	-
Number of slots	$Q_s$	36	-
Speed	$n$	3000	rpm
Current Density	$J$	10	A/mm <sup>2</sup>
Current angle	$\alpha_i^e$	60	°

#### 4.2. Analytical method derivation for discrete skewing

The main period of torque ripple of three-phase winding machines is 60 electrical degrees [102], which therefore dictates the period of the harmonic of the torque ripple of order  $v$ , given in electrical degrees by:

$$T_{v,\text{elec}} = \frac{360^\circ}{v}. \quad (4.1)$$

The aim of the discrete skewing to consider  $N$  machine slices, rotated with respect to each other by a specific angle, so that each slice contributes to different torque harmonics, that will ultimately modulate the torque waveform. This superposition has to be adjusted with the aim of mitigating undesired harmonic components of the resulting torque waveform. The  $v$ -th harmonic of the torque ripple can be expressed as a term of the Fourier series expansion of the electromagnetic torque as:

$$T_{\text{ripple},v}(\theta_{r,e}) = A_v \cdot \cos\left(\frac{\pi}{180} \theta_{r,e} v + \phi_v\right), \quad (4.2)$$

where  $A_v$  is the amplitude of the  $v$ -th harmonic of the torque ripple,  $\theta_{r,e}$  is the rotor position in electrical degrees,  $\phi_v$  is the phase shift of the torque waveform, and  $v = 1, 2, 3, \dots$

In this sense, and following the concept of balanced multiphase systems, if the  $w$ -th harmonic of the torque ripple wants to be mitigated, then the electrical angle between each one of the rotor sectors ( $N$ ) of the machine is proposed as:

$$\theta_{w,\text{elec}} = \frac{360^\circ}{Nw}. \quad (4.3)$$

For example, if a two-step skew is adopted, then the machine rotor will be comprised of two sectors (two halves), each one contributing with torque waveforms that are shifted one with respect to the other. If the electrical shift is  $\theta_{w,elec}$ , then the positive semi-cycles of the  $w$ -th harmonic of the torque ripple of one half of the rotor will compensate the negative semi-cycles of the other half, hence mitigating the undesired component.

The electrical angle between the  $N$  slices of the machine is translated into the skew angle ( $\theta_{skew}$ ), which corresponds to the mechanical angle in which two consecutive rotor slices are rotated one with respect to the other so as to mitigate the  $w$ -th harmonic of the torque ripple.

$$\theta_{skew} = \frac{360^\circ}{pNw} \quad (4.4)$$

In Figure 4.2, the proposed methodology is schematized, comprising the decomposition of the electromagnetic torque waveform in harmonic components, the selection of a high-magnitude undesired component, and the calculation of  $\theta_s$  to mitigate that undesired harmonic depending on the adopted number of slides  $N$ .

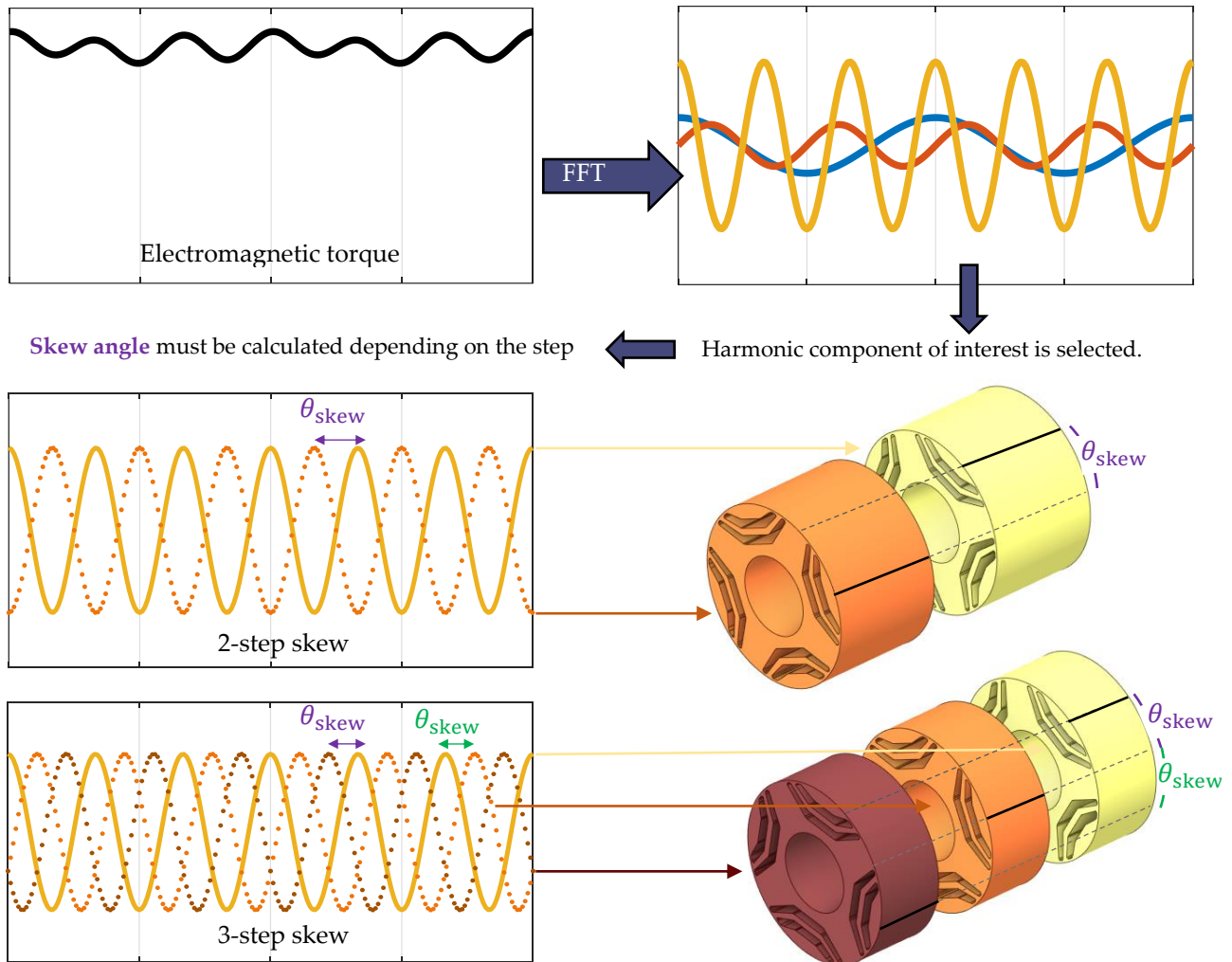


**Figure 4.2.** Schematics of the proposed methodology to calculate the skew angle  $\theta_{skew}$  to mitigate a selected harmonic of order  $w$ . 2 step and 3-step discrete skew are presented, although the method can be used for any number of slides.

Considering the proposed skew angle, (4.2) can be expressed in terms of a sum of the contributions of the  $N$  slices of the machine as

$$T_{rs,v}(\theta_{r,e}) = \sum_{i=1}^N \frac{A_v}{N} \cos\left(\frac{\pi}{180} \theta_{r,e} v - \frac{2\pi v}{Nw}(i-1)\right). \quad (4.5)$$

The resulting reduction on each component of the torque ripple, considering idealized conditions and electromagnetic independency between adjacent slices can be obtained by means of the phasor representation and consequent analysis of (4.5). Then:

$$\Re\{T_{rs,v}(\theta_{r,e})\} = \sum_{i=1}^N \frac{A_v}{N} \cos\left(-\frac{2\pi v}{Nw}(i-1)\right) \quad (4.6)$$

$$\Im\{T_{rs,v}(\theta_{r,e})\} = \sum_{i=1}^N \frac{A_v}{N} \sin\left(-\frac{2\pi v}{Nw}(i-1)\right) \quad (4.7)$$

In consequence, the magnitude of the  $v$ -th harmonic of the torque ripple after applying discrete skewing following the design guidelines of (4.3) and (4.4) can be expressed as

$$|T_{rs,v}(\theta_{r,e})| = \frac{A_v}{N} \sqrt{\left(\cos\left(-\frac{2\pi v}{Nw}(i-1)\right)\right)^2 + \left(\sin\left(-\frac{2\pi v}{Nw}(i-1)\right)\right)^2}. \quad (4.8)$$

Finally, a skew mitigation factor ( $k_{rs,v}$ ) can be devised by obtaining the ratio between (4.2) and (4.8), given by:

$$k_{rs,v} = \frac{1}{N} \sqrt{\left(\cos\left(-\frac{2\pi v}{Nw}(i-1)\right)\right)^2 + \left(\sin\left(-\frac{2\pi v}{Nw}(i-1)\right)\right)^2}. \quad (4.9)$$

This factor is meant to be used after the calculation of the skew angle as per (4.4), and it allows to estimate the resulting amplitude of each torque ripple component (of order  $v$ ) after applying the skew. Simplified equations for  $N = 2, 3$  and  $4$  are provided in the following section, which are further verified and analyzed by means of 2D and 3D finite element analysis.

#### 4.3. Finite Element validation: results and discussion

This section shows the results obtained by applying the analytical method described in section 4.2 for both 4-pole and 6-pole SynRMs. In order to provide the results in a clear fashion, this section is divided into four subsections. The first presents the evaluations of the machines without considering any type of skew, hereby called skewless machines; and the following three sections address machines with different slide number ( $N = 2, N = 3$  and  $N = 4$ ). All the results are obtained by means of 2D and 3D FEA simulations carried out in the commercial package ANSYS Electronic Desktop. The simulation time was chosen to evaluate a whole period of the machine's torque ripple.

#### 4.3.1. FEA evaluation original designs (skewless machines)

Figure 4.3 presents the electromagnetic torque waveform and spatial harmonic spectrum of both the 4-pole and the 6-pole SynRMs. Both 2D and 3D results are shown for comparison. From the results, it can be seen that the evaluation of the 2D and 3D models provide similar values, showing expected small differences, in accordance with the findings of [114]. The harmonic components of the electromagnetic torque for each machine are detailed in Figure 4.3(b) and Figure 4.3(d) for the 4-pole and 6-pole machine respectively. As expected, the largest harmonic component in both designs corresponds to the one generated by the stator slotting effect. Specifically, the highest-magnitude harmonic of the 4-pole machine corresponds to  $v = 3$ , and that of the 6-pole machine corresponds to  $v = 2$ . Therefore, and according to the methodology proposed in Section 3,  $w = 3$  for the 4-pole SynRM and  $w = 2$  for the 6-pole machine. Table 4.2 shows the skew angle that should be considered to discrete skew the machine according to (4.4), depending on the desired step number and aiming to mitigate the highest-magnitude harmonic component. The following sections evaluate the impact of the proposed skew methodology on mitigating torque ripple for  $N = 2$ ,  $N = 3$  and  $N = 4$ .

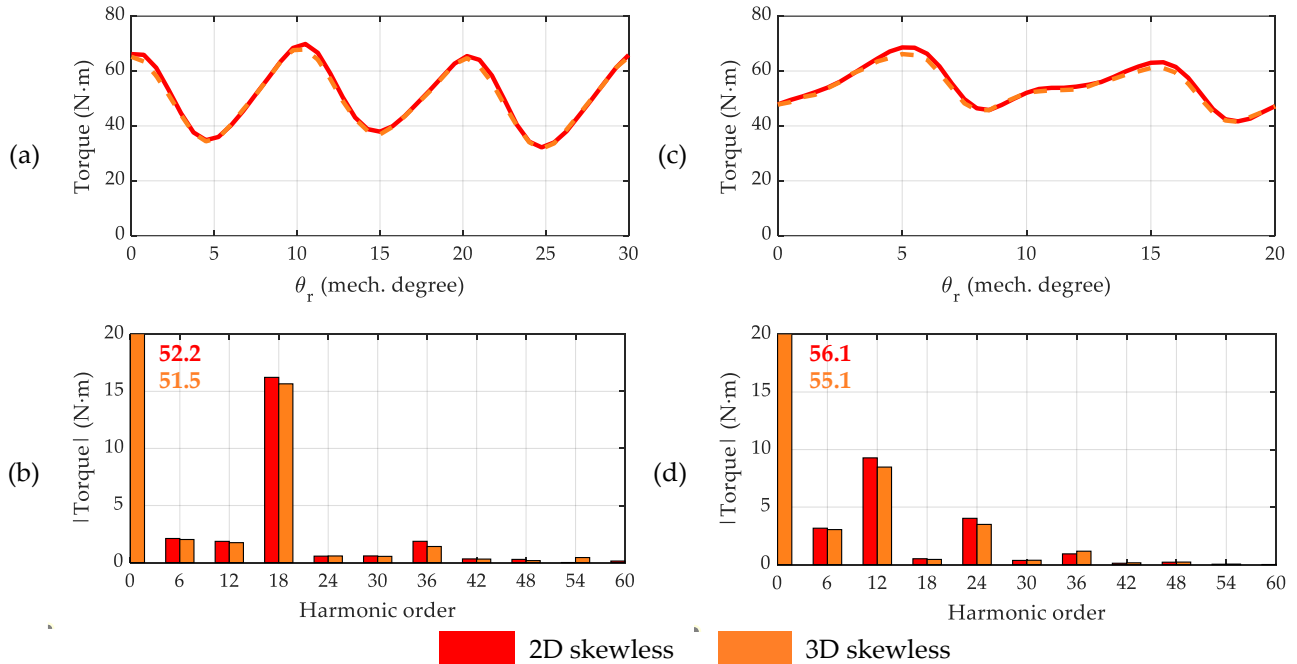


**Figure 4.3.** Electromagnetic torque waveform and spectrum of skewless reference machine; (a) torque waveform of 4-pole machine with two barriers per pole; (b) torque spatial harmonic content of 4-pole machine with two barriers per pole; (c) torque waveform of 6-pole machine with two barriers per pole; (d) torque spatial harmonic content of 6-pole machine with two barriers per pole. Additionally, 2D and 3D simulation results are compared.

**Table 4.2.** Skew angle to reduce a specific electromagnetic torque harmonic order by discrete skew.

	Harmonic order	Mechanical angle for 2-step skew	Mechanical angle for 3-step skew	Mechanical angle for 4-step skew
2p2b	18 <sup>th</sup>	5°	3.33°	2.5°
3p2b	12 <sup>nd</sup>	5°	3.33°	2.5°



### 4.3.2. Evaluation of torque ripple reduction by means of two-step discrete skew

The comparison of the electromagnetic torque for the 4-pole and 6-pole machine is shown in Figure 4.4 when two-step skewing is applied. It can be observed that there is a significant reduction in the harmonic torque component to be mitigated, to around 10% of its original value.

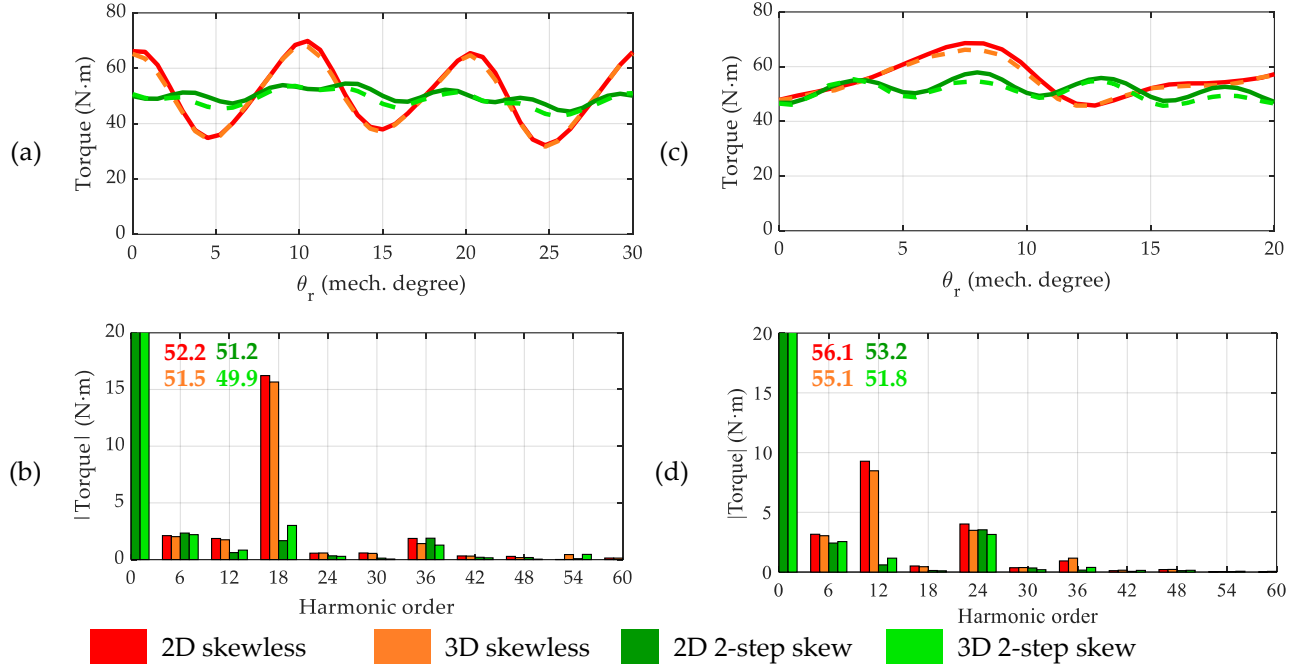


**Figure 4.4.** Comparison of electromagnetic torque waveform and harmonic content of skewless machine vs 2-step skewed machine; (a) torque waveform of 4-pole machine with two barriers per pole; (b) torque spatial harmonic content of 4-pole machine with two barriers per pole; (c) torque waveform of 6-pole machine with two barriers per pole; (d) torque spatial harmonic content of 6-pole machine with two barriers per pole. 2D and 3D simulation results are compared.

This agrees with the estimations obtained from the reduction factor proposed in (4.9), which can be simplified when evaluating  $N = 2$  to:

$$k_{rs,v} = \frac{\sqrt{2}}{2} \sqrt{1 + \cos\left(\pi \frac{v}{w}\right)}. \quad (4.10)$$

According to (4.10), the reduction of the main component of the electromagnetic torque (which has order  $w = 18$ ) should be maximum ( $k_{rs,w} = 0$ ). The difference lies in the fact that (9) considers magnetically independent rotor slices, neglecting their interaction. Regardless of this, a significant reduction was observed in other harmonic components. In addition, for the 4-pole machine it was found the torque ripple harmonic component with  $v = 12$  was also reduced to  $\sim 45\%$  of its original value, whilst other relevant harmonics of order  $v = 6$  and  $v = 36$  were not significantly affected. This agrees with the estimated reduction factor proposed in (4.10), since  $k_{rs,6} = 0.87$ ,  $k_{rs,12} = 0.5$  and  $k_{rs,36} = 1$ . In turn, for the 6-pole machine it was observed the relevant torque ripple harmonic component with  $v = 24$  is slightly reduced (to 87% of the original value), and that other relevant harmonics of order  $v = 6$  and  $v = 36$  are reduced to 77% and 14% of their original magnitude, respectively. This agrees with the estimated reduction factor proposed in (4.10), since  $k_{rs,6} = 0.7$ ,

$k_{rs,24} = 1$  and  $k_{rs,36} = 0$ . In addition, the trend of other less-relevant harmonic components of both machines matches closely with the estimations of (4.10). These findings are summarized in Table 4.3.

**Table 4.3.** Torque ripple harmonic component reduction as a result of 2-step skewing. 3D results are considered, and relevant harmonic components are analyzed.

Harmonic order	4-pole SynRM		6-pole SynRM	
	$k_{rs,v}$ (analytical)	$k_{rs,v}$ (FEA)	$k_{rs,v}$ (analytical)	$k_{rs,v}$ (FEA)
$v = 6$	0.87	0.95	0.71	0.77
$v = 12$	0.50	0.45	0.00	0.06
$v = 18$	0.00	0.10	-	-
$v = 24$	-	-	1.00	0.87
$v = 30$	-	-	-	-
$v = 36$	1.00	1.02	0.00	0.14

As a consequence of the discrete two-step skewing, the peak-to-peak value of the torque ripple was reduced. Table 4.4 summarizes the torque ripple as a percentage of the mean torque for the 2D and 3D simulations results, respectively. The torque ripple reduction is greater than 70% for the 4-pole machine and up to 55% for the 6-pole design, and an expected slight reduction of the average torque was also obtained.

**Table 4.4.** Average torque and torque ripple comparison when applying 2-step skewing, by means of 2D and 3D FEA simulations.

		Skewless 2D	Skewless 3D	2-step skew 2D	2-step skew 3D
4-pole SynRM	$T_{avg}$	51.0 Nm	50.2 Nm	50.0 Nm	48.7 Nm
	$T_{rp}$	73.9 %	72.1 %	20.2 %	22.6 %
6-pole SynRM	$T_{avg}$	54.7 Nm	53.8 Nm	51.9 Nm	50.5 Nm
	$T_{rp}$	49.2 %	45.9 %	21.4 %	19.2 %

In this specific case, it can be observed that the 3D evaluation shows worse results than the 2D assessment, since in the 3D the ripple reduction is lower, and the mean torque reduction is increased, with respect to the 2D simulations. This can be ascribed to the fact that 2D simulations on ANSYS consider each slice of the machine as independent machines, when discrete skewing is applied, and the interface between slices is not taken into account, resulting in an idealization of the problem. On the other hand, the 3D simulation evaluates the rotor as a whole unit comprised of physically rotated slices, hence considering effects within the adjacent slices interface. This is further addressed in section 4.5.

#### 4.3.3. Evaluation of torque ripple reduction by means of three-step discrete skew

The comparison of the electromagnetic torque for the 4-pole and 6-pole machine is shown in Figure 4.5 when adopting a three-step discrete skew strategy.

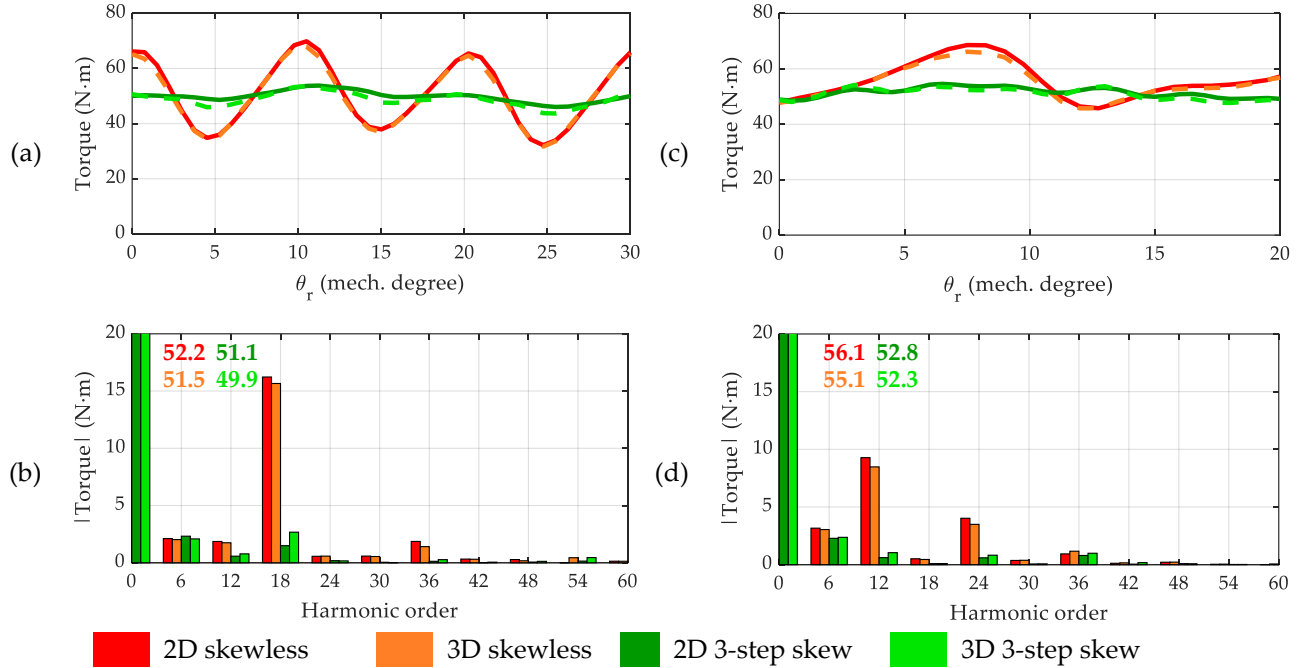


**Figure 4.5.** Comparison of electromagnetic torque waveform and harmonic content of skewless machine vs 3-step skewed machine; (a) torque waveform of 4-pole machine with two barriers per pole; (b) torque spatial harmonic content of 4-pole machine with two barriers per pole; (c) torque waveform of 6-pole machine with two barriers per pole; (d) torque spatial harmonic content of 6-pole machine with two barriers per pole. 2D and 3D simulation results are compared.

As in the case of the two-step skewing, there is a significant reduction of the highest-magnitude harmonic component of the torque ripple, of up to 93%. This is concordance with the reduction factor derived in (4.9), expression that can be further simplified for cases with  $N = 3$  as per:

$$k_{rs,v} = \frac{1}{3} \left[ 1 + 2 \cos\left(\frac{2\pi v}{3w}\right) \right] \quad (4.11)$$

According to (4.11), the reduction of the highest-magnitude component of the electromagnetic torque, when  $v = w$ , is maximum ( $k_{rs,w} = 0$ ). Additionally, for the 4-pole machine it was found the torque ripple harmonic components with  $v = 12$  and  $v = 36$  were reduced to  $\sim 45\%$  and  $\sim 6\%$  of their original value, respectively, whilst the other relevant harmonic of order  $v = 6$  is not significantly affected. This agrees with the reduction factor proposed in (11) for  $N = 3$ , since  $k_{rs,6} = 0.84$ ,  $k_{rs,12} = 0.45$  and  $k_{rs,36} = 0$ . On the other hand, for the 6-pole machine it was observed the harmonic components with  $v = 6$  and  $v = 24$  were reduced to  $\sim 70\%$  and  $\sim 12\%$  of their original value, respectively, whilst the harmonic of order  $v = 36$  is not visibly reduced. This agrees with the values provided by (4.11), since  $k_{rs,6} = 0.67$ ,  $k_{rs,24} = 0$  and  $k_{rs,36} = 1$ . Although they are not relevant contributors, the trend of other harmonic components of both machines are in good agreement with the expression presented in (4.11). These findings are summarized in Table 4.5.

**Table 4.5.** Torque ripple harmonic component reduction as a result of 3-step skewing. 3D results are considered and relevant harmonic components are analyzed.

Harmonic order	4-pole SynRM		6-pole SynRM	
	$k_{rs,v}$ (analytical)	$k_{rs,v}$ (FEA)	$k_{rs,v}$ (analytical)	$k_{rs,v}$ (FEA)
$v = 6$	0.84	0.95	0.67	0.70
$v = 12$	0.45	0.45	0.00	0.06
$v = 18$	0.00	0.09	-	-
$v = 24$	-	-	0.00	0.12
$v = 30$	-	-	-	-
$v = 36$	0.00	0.06	1.00	0.90

As a result of the discrete three-step skewing, the peak-to-peak value of the torque ripple was considerably reduced. Table 4.6 presents the obtained mean torque and torque ripple (as a percentage of the mean torque) for the 2D and 3D simulations respectively. It may be noted that the torque ripple reduction is greater than 75% in both designs analyzed and there is an expected slight reduction of the average torque.

Similar to the case of two-step skewing, it can be appreciated that the 3D evaluation shows a worse outcome than the 2D assessment, since a lower ripple reduction and a higher mean torque reduction are achieved.

**Table 4.6.** Average torque and torque ripple comparison when applying 3-step skewing, by means of 2D and 3D FEA simulations.

		Skewless 2D	Skewless 3D	2-step skew 2D	2-step skew 3D
4-pole SynRM	$T_{avg}$	51.0 Nm	50.2 Nm	49.9 Nm	48.7 Nm
	$T_{rp}$	73.9 %	72.1 %	15.6 %	18.3 %
6-pole SynRM	$T_{avg}$	54.7 Nm	53.8 Nm	51.5 Nm	51.0 Nm
	$T_{rp}$	49.2 %	45.9 %	11.8 %	12.7 %

#### 4.4.4. Evaluation of torque ripple reduction by means of four-step discrete skew

The comparison of the electromagnetic torque for the 4-pole and 6-pole machine is shown in Figure 4.6 when four-step skewing is applied. It can be observed that there is a significant reduction in the harmonic torque component to be mitigated, to around 10% of its original magnitude, in a similar extent to the 2-step and 3-step skewing.

The information in Figure 4.8 agrees with the estimations obtained from the reduction factor proposed in (4.9), which, for the specific case of  $N = 4$  can be simplified to:

$$k_{rs,v} = \frac{\sqrt{2}}{2} \cos\left(\frac{\pi v}{2w}\right) \sqrt{1 + \cos\left(\frac{\pi v}{2w}\right)} \quad (4.12)$$

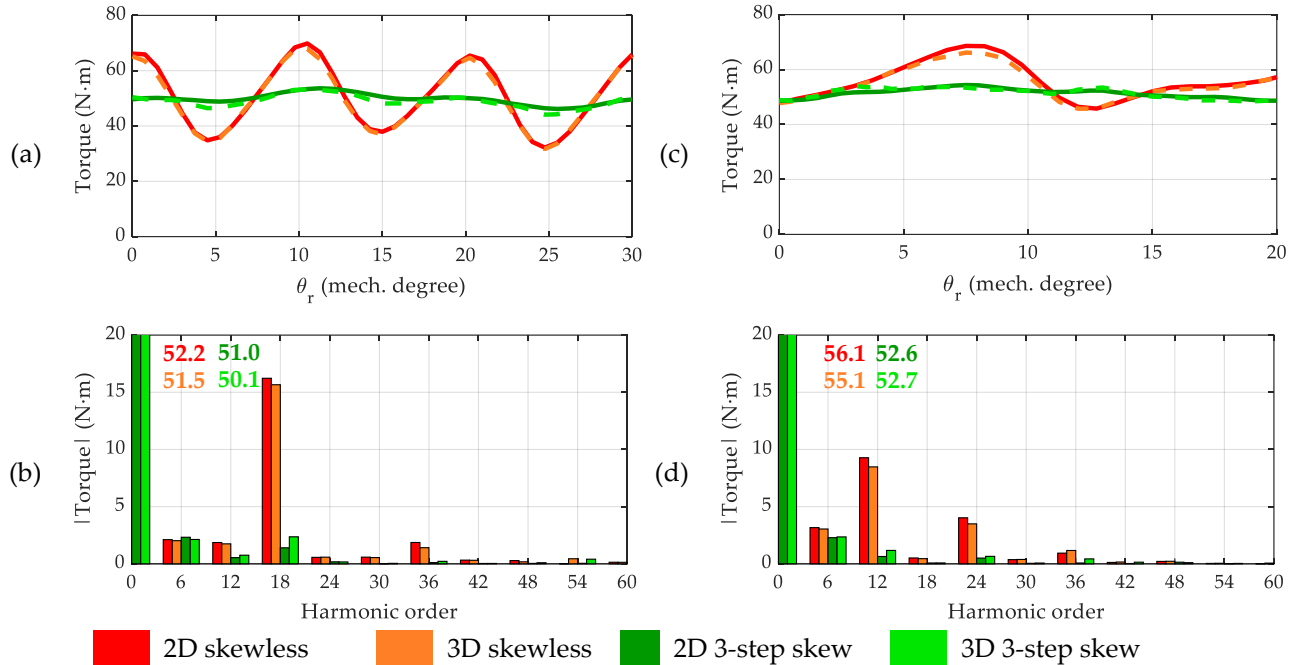


**Figure 4.6.** Comparison of electromagnetic torque waveform and harmonic content of skewless machine vs 4-step skewed machine; (a) torque waveform of 4-pole machine with two barriers per pole; (b) torque spatial harmonic content of 4-pole machine with two barriers per pole; (c) torque waveform of 6-pole machine with two barriers per pole; (d) torque spatial harmonic content of 6-pole machine with two barriers per pole. 2D and 3D simulation results are compared.

Based on (4.12), the reduction of the highest-magnitude component of the electromagnetic torque, when  $v = w$ , is maximum ( $k_{rs,w} = 0$ ). Additionally, for the 4-pole machine it was found the torque ripple harmonic components with  $v = 12$  and  $v = 36$  were reduced to  $\sim 35\%$  and  $\sim 5\%$  of their original value, respectively, whilst the other relevant harmonic of order  $v = 6$  is not affected. This agrees with the reduction factor proposed in (4.12) for  $N = 3$ , since  $k_{rs,6} = 0.84$ ,  $k_{rs,12} = 0.43$  and  $k_{rs,36} = 0$ . On the other hand, for the 6-pole machine it was observed the harmonic components with  $v = 6$ ,  $v = 24$  and  $v = 36$  were reduced to  $\sim 74\%$ ,  $\sim 12\%$  and  $\sim 6\%$  of their original value, respectively. This agrees with the values provided by (4.12), since  $k_{rs,6} = 0.65$ ,  $k_{rs,24} = 0$  and  $k_{rs,36} = 0$ . Although they are not relevant contributors, the trend of other harmonic components of both machines are in good agreement with the expression presented in (4.12). The summary of these results is presented in Table 4.7.

**Table 4.7.** Torque ripple harmonic component reduction as a result of 3-step skewing. 3D results are considered and relevant harmonic components are analyzed.

Harmonic order	4-pole SynRM		6-pole SynRM	
	$k_{rs,v}$ (analytical)	$k_{rs,v}$ (FEA)	$k_{rs,v}$ (analytical)	$k_{rs,v}$ (FEA)
$v = 6$	0.84	1.01	0.65	0.74
$v = 12$	0.43	0.35	0.00	0.06
$v = 18$	0.00	0.08	-	-
$v = 24$	-	-	0.00	0.12
$v = 30$	-	-	-	-
$v = 36$	0.00	0.05	0.00	0.06

Four-step skewing resulted into a severe torque ripple reduction, as summarized in Table 4.8, which presents the results obtained by means of the 2D and 3D evaluations, respectively. The torque ripple reduction is greater than 75% in both designs analyzed and there is an expected slight reduction of the average torque.

**Table 4.8.** Average torque and torque ripple comparison when applying 4-step skewing, by means of 2D and 3D FEA simulations.

		Skewless 2D	Skewless 3D	2-step skew 2D	2-step skew 3D
4-pole SynRM	$T_{avg}$	51.0 Nm	50.2 Nm	49.8 Nm	48.7 Nm
	$T_{rp}$	73.9 %	72.1 %	15.0 %	18.3 %
6-pole SynRM	$T_{avg}$	54.7 Nm	53.8 Nm	51.4 Nm	51.0 Nm
	$T_{rp}$	49.2 %	45.9 %	11.2 %	12.7 %

Close to the case of two-step and three-step skewing, it may be appreciated that the 3D evaluation shows a worse outcome than the 2D assessment, since a lower ripple reduction and a higher mean torque reduction are achieved.

#### 4.4. Comparison, analysis, and recommendations

The flux density distribution for the 6-pole SynRM is show in Figure 4.7 for the skewless rotor, and for the 2, 3 and 4-steps skew models. It can be observed that the tangential bridges of the barriers are well saturated. From the 3D plots of the flux density distribution the number of steps used for the skewing is clearly highlighted. The step used for the skew of each case becomes smaller as the number of steps increases. SynRMs are affected by the leakage flux and the cross-coupling effect between the  $dq$ -axes. The cross-coupling between the different modules causes a leakage between each slice, which is only taken into account by 3D simulations. All the above-mentioned phenomena are affected by the skew angle: a smaller skew angle causes have less influence on this effect, and thus on the performance of the machine.

When comparing the results of the 2D with those of 3D FEA simulations, a slight difference can be observed. First, the average torque reduction due to skew in 3D simulation is greater than the 2D simulation, which occurs because the step-step leakage contributes to the reduction of the average torque. Nevertheless, the torque ripple reduction in both cases is quite similar. As a result, it can be said that during the preliminary design stage 2D simulations can be used to save time and understand the effects of discrete skew method on torque performance.

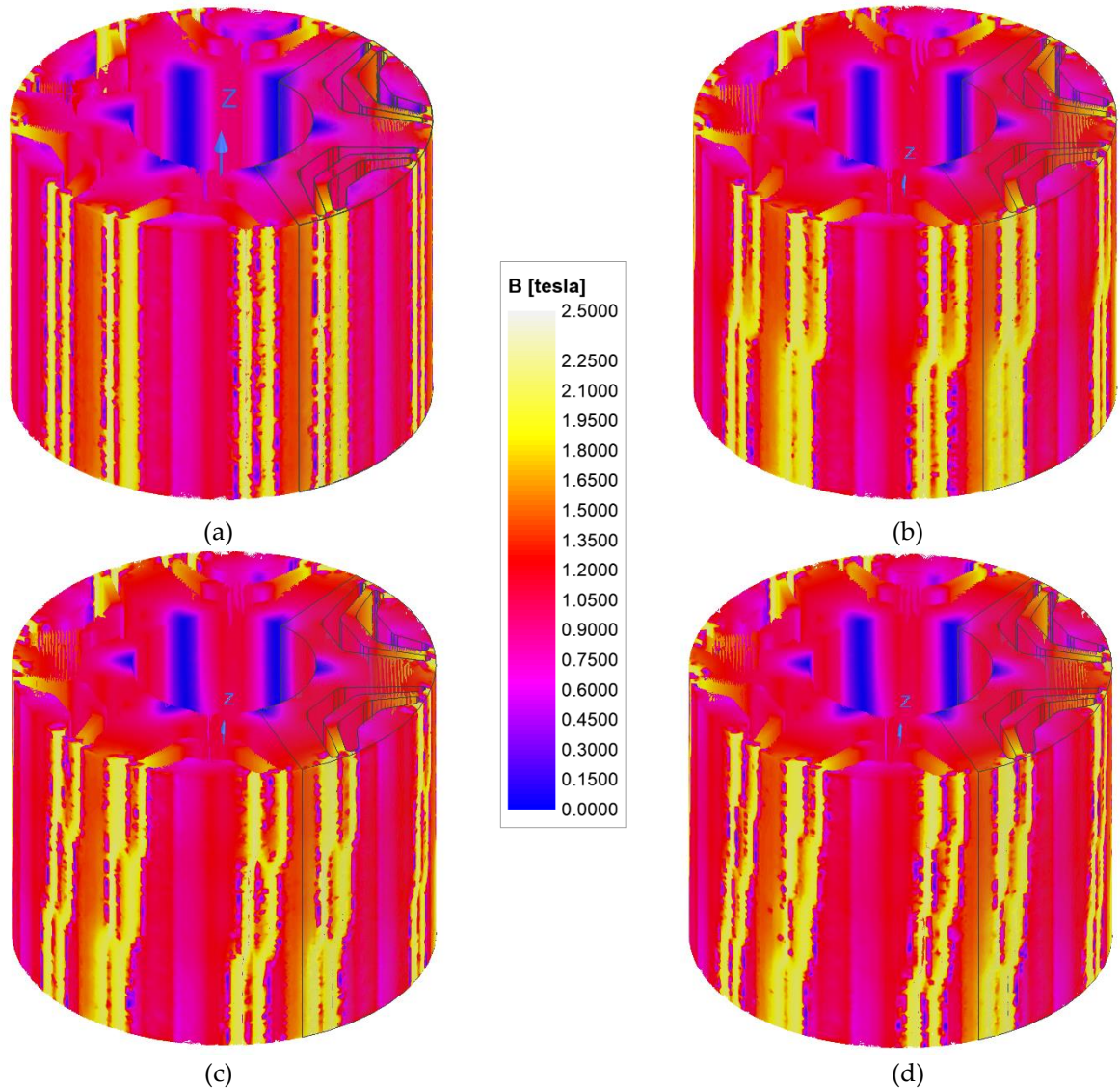


**Figure 4.7.** Flux density distribution in a 6-pole machine with two barriers per pole for  $J = 10 \text{ A/mm}^2$  and  $\theta_{r,e} = 0$ . (a) skewless machine; (b) 2-step skew machine; (c) 3-step skew machine; (d) 4-step skew machine.

It is possible to observe that, when  $N=2$  and  $N=3$  is compared, there is a considerable improvement in the reduction of the torque ripple, and the behavior is different for  $N=3$  and  $N=4$ , where the reduction is the same. For all cases,  $N=2$ ,  $N=3$  and  $N=4$ , the average torque remains relatively constant. Therefore, when assessing close-to-purely-sinusoidal electromagnetic torque waveforms in a SynRM, then 2-step skew may be sufficient as a single ripple component must be mitigated. Conversely, if there are several preponderant harmonic components, then it is worth taking a multi-step skewing approach, to mitigate multiple harmonics at once. In consequence, it is necessary to correctly analyze the harmonic distribution of the electromagnetic torque to properly choose  $N$ , as increasing the number of steps does not always guarantee a significant reduction in torque ripple and could lead to other different manufacturing costs.

#### *4.5. Summary*

A study on the discrete-skew methodology was conducted and a method was proposed to better understand the impact of skewing angle and its determination during the design phase of SynRM. After reviewing relevant literature, a reduction factor for each harmonic component was introduced and derived in general form to estimate the torque ripple component amplitudes as a function of skew. This allowed for the calculation of the overall torque ripple waveform. The proposed method was validated by evaluating two SynRMs and achieving a torque ripple reduction of up to 70%. Results from the analysis and FEA evaluation showed good agreement. The results suggest that 2D FEA is preferred over computationally intensive 3D simulations to assess the performance of discrete skew. The harmonic distribution of torque ripple can be used to select the best skewing strategy: a 2-step skewing is recommended for mostly-purely-sinusoidal waveforms, while a multi-step skewing is advised for machines with multiple high-magnitude harmonic components.



## Chapter V: Proposed design of a Synchronous Reluctance Machine

This chapter utilizes the techniques outlined in previous chapters to design a SynRM prototype through an optimization process based on genetic algorithms and FEM simulations. The optimization yields two designs, one symmetrical and one asymmetrical, which are evaluated for average torque, torque ripple, saliency ratio, and power factor. The optimal designs are further scrutinized mechanically to ensure they meet established standards for rotor integrity.

### 5.1. Set-up of the optimization process

Figure 5.1 presents the rotor parameterization for one pole of a SynRM with three flux barriers per pole. The optimization process was carried out using ANSYS commercial software package (Electronic Desktop for electromagnetic analysis, DesignModeler for geometry parameterization, and Workbench for optimization), combining MOGA and FEM simulations. The optimization considered two machine configurations: a 4-pole and a 6-pole. Only rotor geometry was optimized in both cases because torque ripple is more sensitive to rotor structure variations [115] as showed in sensitivity analysis on Chapter 3. The number of poles was chosen because average torque is inversely proportional to the number of poles [45], [116], making machines with a low number of poles preferable.

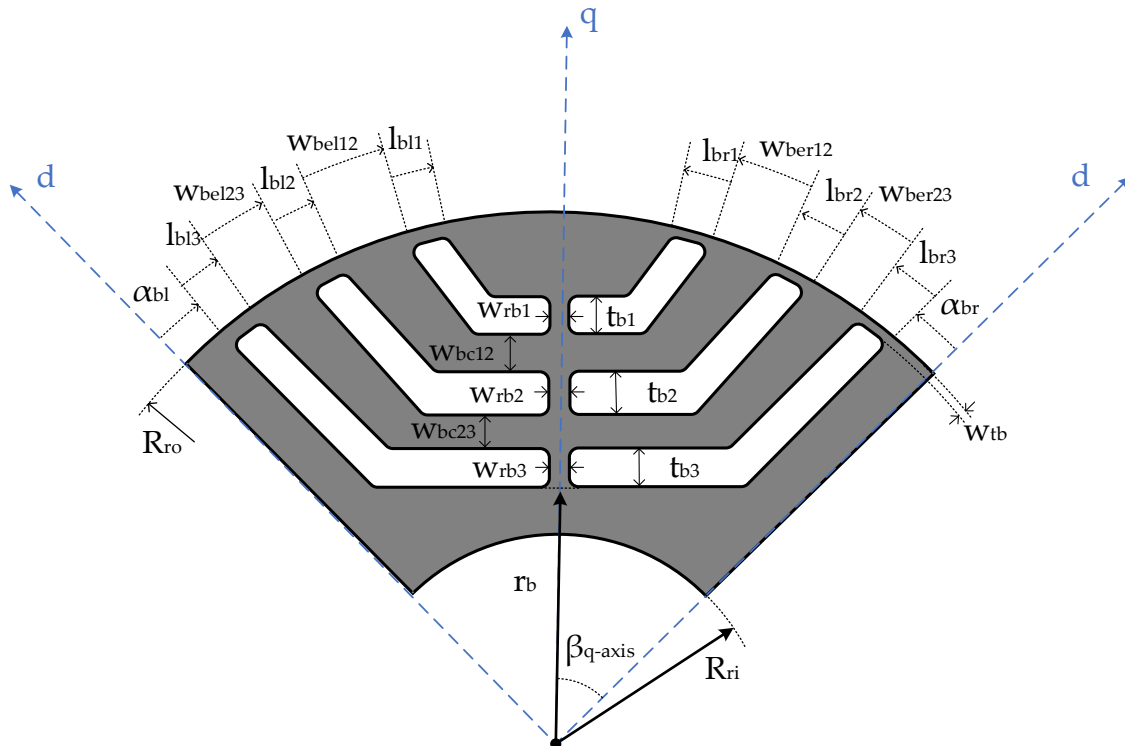


**Figure 5.1.** Sketch of the rotor of a SynRM with three flux barriers per pole. The parameters subject to optimization are properly defined on both sides of the  $q$ -axis of the rotor.

The optimization process involves two steps. First, a symmetrical design is found where the rotor parameters on both sides of the  $q$ -axis are identical. The second step involves optimization for an asymmetrical design with complete freedom for the rotor parameters on either side of the  $q$ -axis.

Radial bridges are excluded from the electromagnetic optimization because they would significantly prolong the optimization phase. Each step of the optimization follows the workflow outlined in Figure 3.2 of Chapter III. The optimization starts with defining the geometry, then it is analyzed through FEM simulation to obtain the desired performance indices.

The main data of the machine is presented in table 5.1. During optimization, the machine was supplied with 20 A/mm<sup>2</sup>, which corresponds to approximately 3 times the rated current listed in Table 5.1. Selecting a current between 2 and 3 times the rated current improves the torque ripple's insensitivity to load variations [110], [111].

**Table 5.1.** Main data of the machine subject to optimization.

Parameter	Symbol	Value
Stator outer diameter	$D_{so}$	246 mm
Stator inner diameter	$D_{si}$	161.4 mm
Rotor outer diameter	$D_{ro}$	160.4 mm
Rotor inner diameter	$D_{ri}$	70 mm
Tooth height	$h_t$	22.8 mm
Toot width	$b_t$	9 mm
Air-gap length	$g$	0.5 mm
Stack length	$l_{st}$	120 mm
Number of slots	$Q_s$	36
Number of turns	$N_s$	6
Number of pole pairs	$p$	2 - 3
Synchronous speed	$n$	5000 rpm
Rated current density	$J_n$	7.5 A/mm <sup>2</sup>
Stacking factor	$k_s$	0.95
Lamination thickness	$e$	0.35 mm

The objective functions are set to minimize the torque ripple, maximize the power factor, and maintain the average torque above a specific value (100 Nm), as shown in Table 5.2. The primary constraint during optimization was to maintain the machine's insulation ratio within the limits defined in literature [117], between 0.35 and 0.45. Geometric constraints were established to ensure that feasible rotor geometries are obtained and to prevent errors or unrealistic solutions during the optimization process. The upper and lower limits for the rotor's geometrical parameters (objective variables) are properly defined and displayed in Table 5.3.

**Table 5.2.** Objective function for the optimization process.

Parameter	Symbol	Operator	Value	Objective	Unit
Torque Ripple	$T_{rp}$	-	-	min	-
Average Torque	$T_{avg}$	$\geq$	100		Nm
Maximum Internal Power Factor	$IPF_{max}$	-	-	max	-

The optimization process was adjusted by defining a minimum quality mesh that would yield proper torque waveform values, enabling effective extraction of average torque and torque ripple. Iron losses were not analyzed in this stage for faster optimization. Only one torque ripple period was

simulated, equivalent to 60 electrical degrees in three-phase machines [102], and the sample number was selected based on the Nyquist criteria for accurate FFT calculation.

### 5.2. Results from the optimization process

The optimization results are presented in Figures 5.2 and 5.3 for the 4-pole and 6-pole machines, respectively. It can be concluded from the results that the 6-pole machine delivers a higher average torque and a lower torque ripple compared to the 4-pole machine. The optimal design is selected based on a trade-off between average torque and torque ripple as it is not possible to achieve the lowest torque ripple and highest average torque simultaneously.

**Table 5.3.** Input variables range for the optimization process for 4-pole and 6-pole SynRM.

Symbol	4-pole		6-pole		Unit
	Lower	Upper	Lower	Upper	
$\alpha_{br}$	1	35	1	25	mech. degree
$\alpha_{bl}$	1	35	1	25	mech. degree
$l_{br1}$	3	10	2.5	10	mech. degree
$l_{br2}$	3	10	2.5	10	mech. degree
$l_{br3}$	3	20	2.5	20	mech. degree
$l_{bl1}$	3	10	2.5	10	mech. degree
$l_{bl2}$	3	10	2.5	10	mech. degree
$l_{bl3}$	3	10	2.5 <td 10	mech. degree	
$w_{ber_{12}}$	2	10	2	10	mech. degree
$w_{bel_{12}}$	2	10	2	10	mech. degree
$w_{ber_{23}}$	2	10	2	10	mech. degree
$w_{bel_{23}}$	2	10	2	10	mech. degree
$t_{b1}$	5	15	5	15	mm
$t_{b2}$	5	15	5	15	mm
$t_{b3}$	5	15	5	15	mm
$w_{bc_{12}}$	2	10	2	10	mm
$w_{bc_{23}}$	2	10	2	10	mm
$w_{tb}$	0.5	2	0.5	2	mm
$r_b$	40	50	40	50	mm
$\alpha_i^e$	50	70	50	70	elect. degree

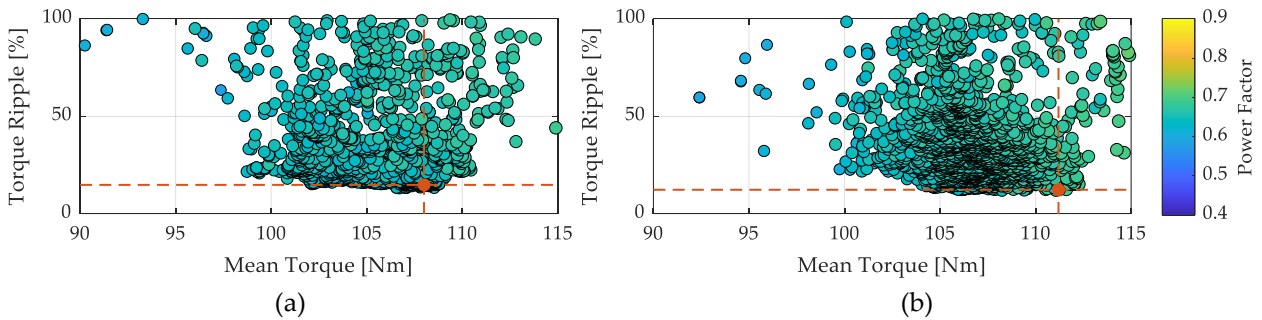


**Figure 5.2.** Designs obtained from the optimization process for a 4-pole machine with three flux barriers per pole. The current was fixed to  $\sim 20$  A/mm<sup>2</sup> and the current angle was defined in the optimization algorithm for MTPA. (a) symmetric design; (b) asymmetric design. The selected designs are highlighted on the figure.

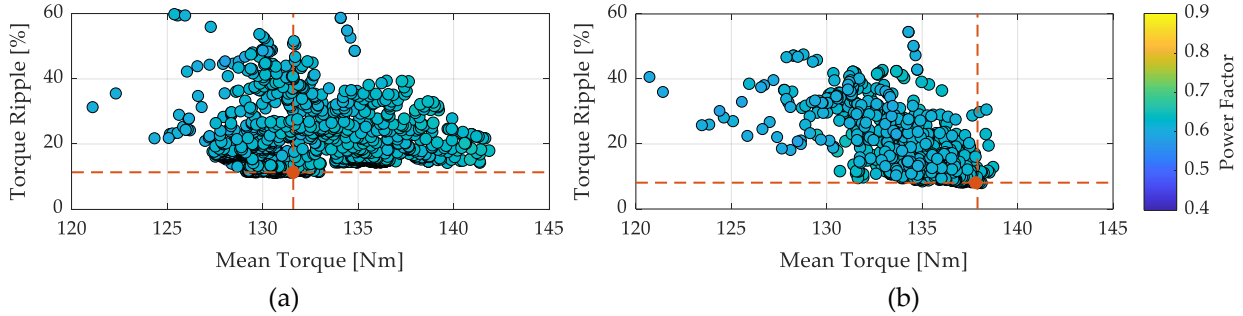


**Figure 5.3.** Designs obtained from the optimization process for a 6-pole machine with three flux barriers per pole. The current was fixed to  $\sim 20$  A/mm<sup>2</sup> and the current angle was defined in the optimization algorithm for MTPA. (a) symmetric design; (b) asymmetric design. The selected designs are highlighted on the figure.

The optimized design incorporates ducts in the first rotor island to decrease the island mass and centrifugal force. Figures 5.4 and 5.5 depict the impact of duct radius and current density on average torque and torque ripple with a fixed current angle of 60 electrical degree. The ducts have minimum effect on average torque, but a slight effect on torque ripple. Thus, ducts were included in the final design to reduce island mass and the width of radial bridges, leading to quicker saturation and fewer flux lines crossing the flux barriers. The mechanical analysis of these optimal designs will be conducted in the next subchapter.

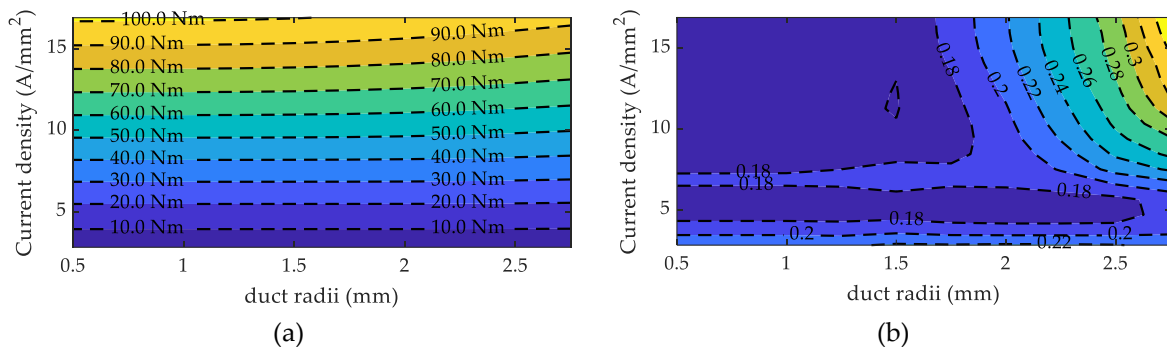


**Figure 5.4.** Behavior of the average torque and torque ripple in the symmetrical design for different radii of the duct located in the first rotor island when  $\alpha_i^e = 60^\circ$  elect. degree. (a) average torque; (b) torque ripple.

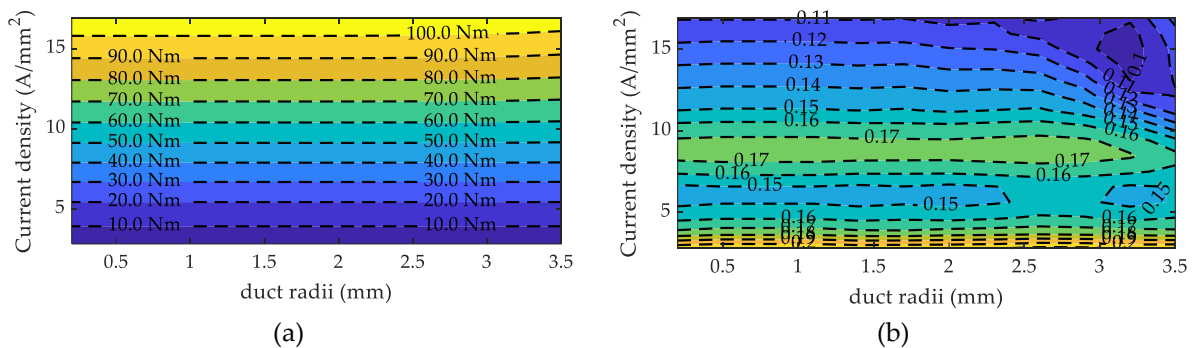


**Figure 5.5.** Behavior of the average torque and torque ripple in the symmetrical design for different radii of the duct located in the first rotor island when  $\alpha_i^e = 60^\circ$  elect. degree. (a) average torque; (b) torque ripple.

### 5.3. Structural analysis

To validate the rotor's mechanical robustness, 2D structural analysis was conducted using ANSYS Mechanical at a maximum speed of 10,000 rpm. Radial iron bridges were added to the rotor structure and their thicknesses were determined based on the rotor island mass, as described in [118]. Figure 6.6 shows the considered rib distribution, with innermost, middle, and outermost barriers having thicknesses of 1.8mm, 1.5mm, and 1.4mm, respectively, for both symmetrical and asymmetrical designs. Both designs have a tangential rib thickness of  $\sim 1.3$  mm. The effects of temperature were neglected in this analysis. The symmetrical design has a safety factor of 1.78, and the asymmetrical design has a safety factor of 1.64, based on the 465 MPa yield stress of M250-35A laminated steel. Figure 5.6 shows some areas of the rotor structure that are subject to high von-Mises stress in both designs.

Figure 5.7 displays the ANSYS Mechanical results for 10,000 rpm M250-35A steel rotor show a deformation of  $\sim 0.013$  mm ( $\sim 3\%$  of the air-gap length) in the air-gap zona. This deformation falls within the acceptable range for many applications, indicating that the rotor is likely to perform reliably and efficiently under these operating conditions. However, it's important to keep in mind that this deformation could be an indicator of excessive loading or wear on the rotor and require further evaluation to ensure its continuity and safety in operation.

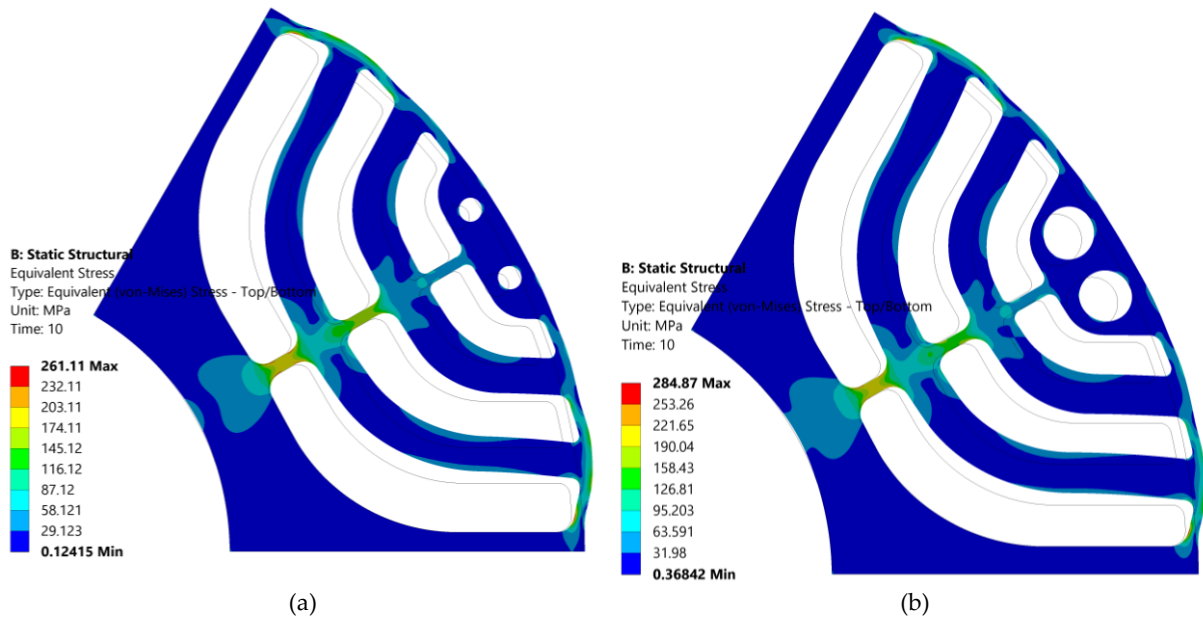


**Figure 5.6.** Von Mises stress distribution for the optimal designs at 10,000 rpm. (a) symmetric design; (b) asymmetric design. Graphical results are magnified x10 for easy viewing.

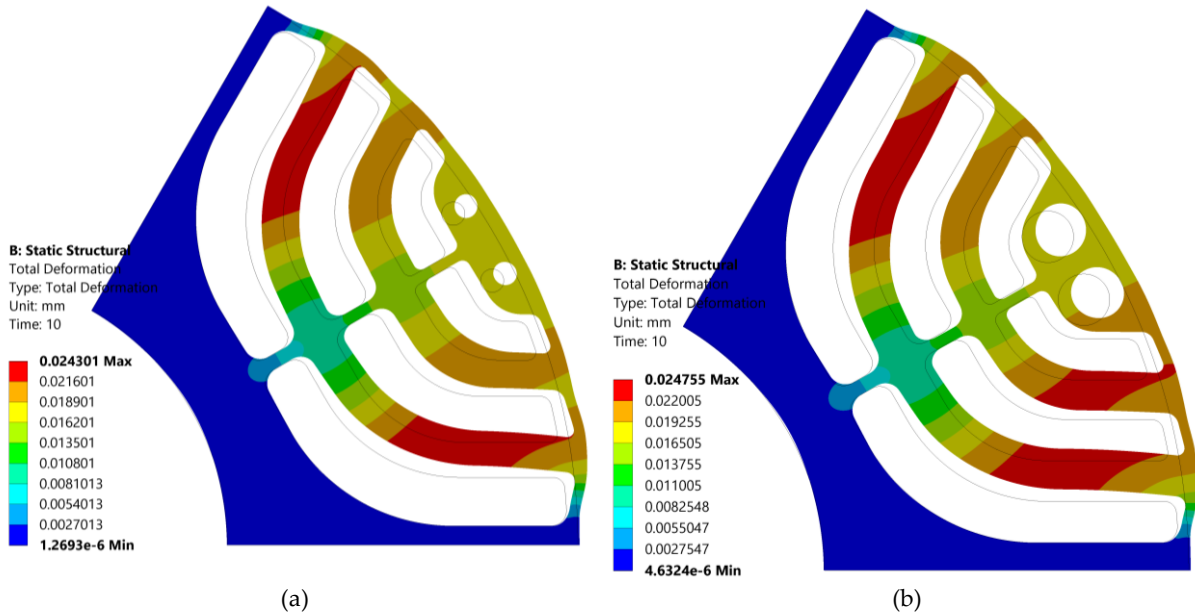


**Figure 5.7.** Total deformation distribution for the optimal designs at 10,000 rpm. (a) symmetric design; (b) asymmetric design. Graphical results are magnified  $\times 10$  for easy viewing.

#### 5.4. Optimal design adjustment

The optimal designs were analyzed for their saliency ratio, power factor, average torque, and torque ripple across various operating points. These analyses were conducted for both clockwise and counter-clockwise rotations. Figures 5.8, 5.9, 5.10 and 5.11 display the contour maps for the saliency ratio, internal power factor, ripple torque, and average torque, respectively.

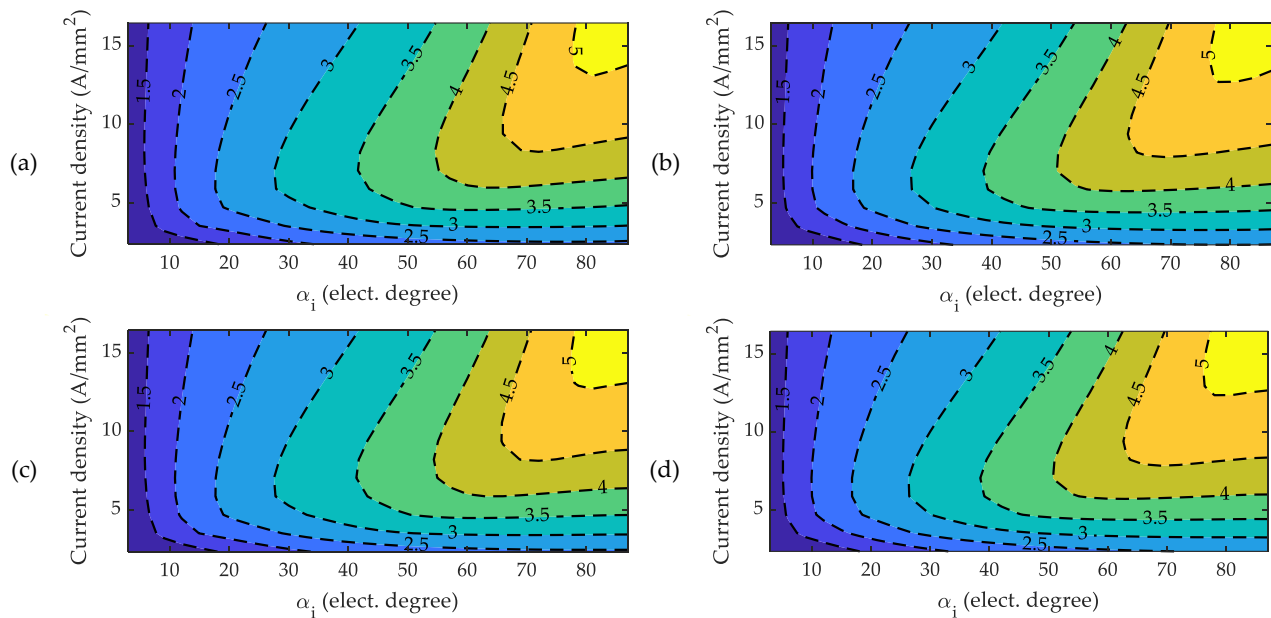


**Figure 5.8.** Saliency ratio for the symmetric and asymmetric design. (a) symmetric design counter-clockwise rotation; (b) asymmetric design counter-clockwise rotation; (c) symmetric design clockwise rotation; (d) asymmetric design clockwise rotation.

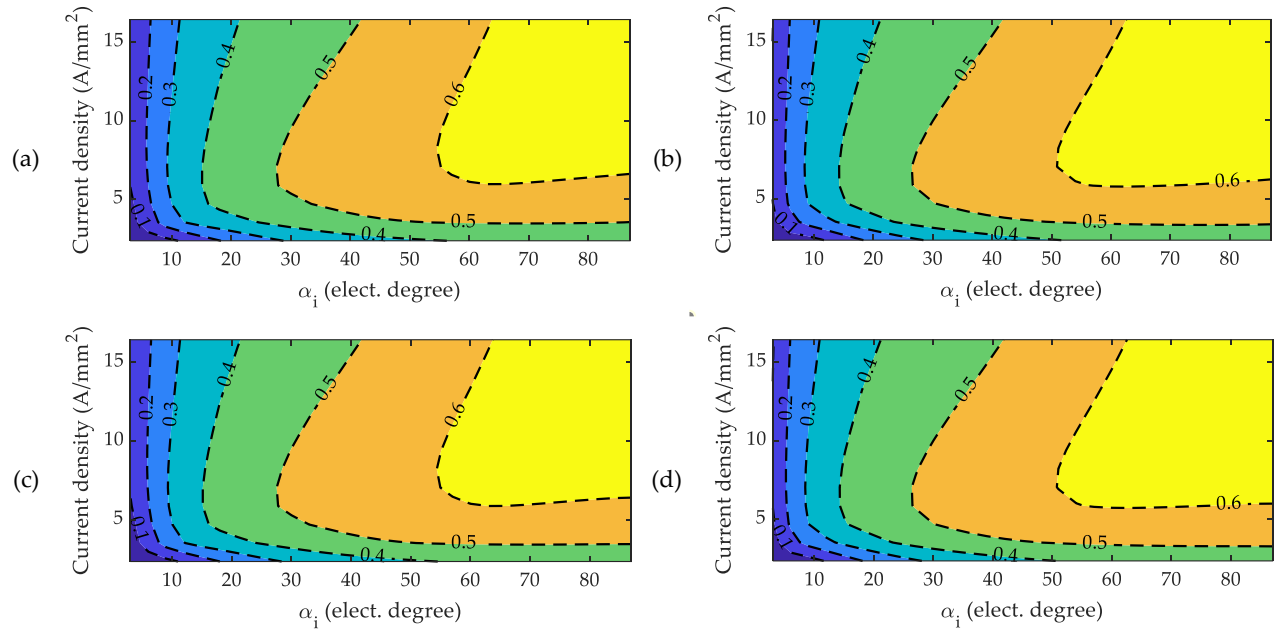


**Figure 5.9.** Internal power factor for the symmetric and asymmetric design. (a) symmetric design counter-clockwise rotation; (b) asymmetric design counter-clockwise rotation; (c) symmetric design clockwise rotation; (d) asymmetric design clockwise rotation.

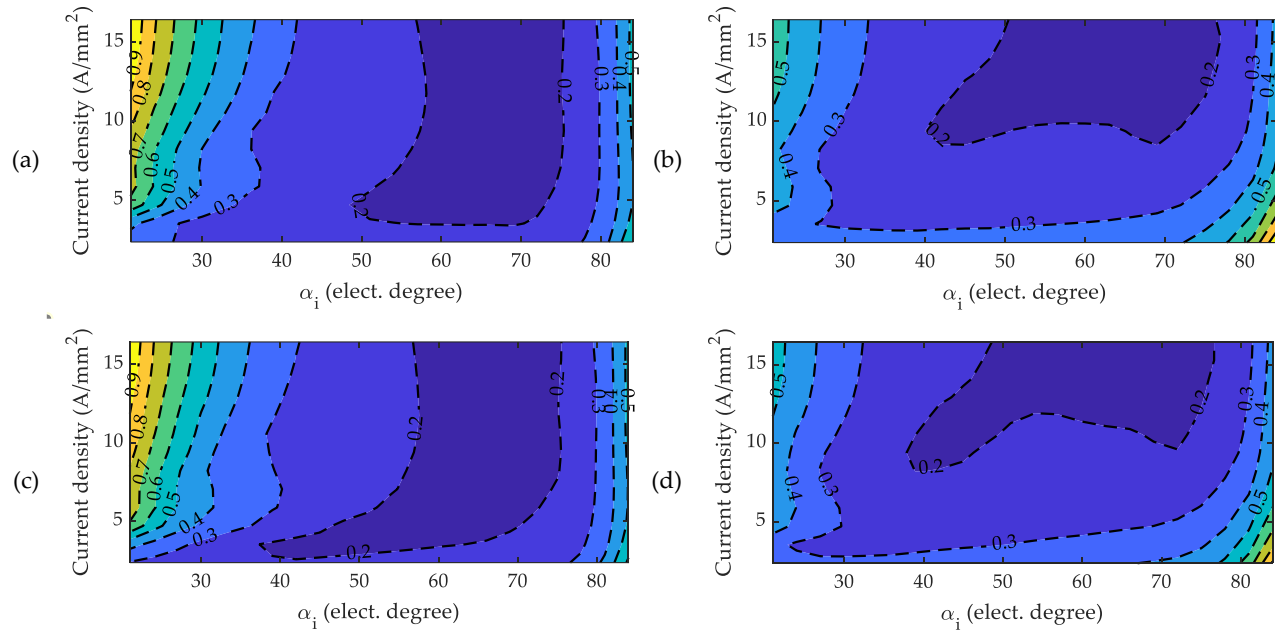


**Figure 5.10.** Torque ripple for the symmetric and asymmetric design. (a) symmetric design counter-clockwise rotation; (b) asymmetric design counter-clockwise rotation; (c) symmetric design clockwise rotation; (d) asymmetric design clockwise rotation.

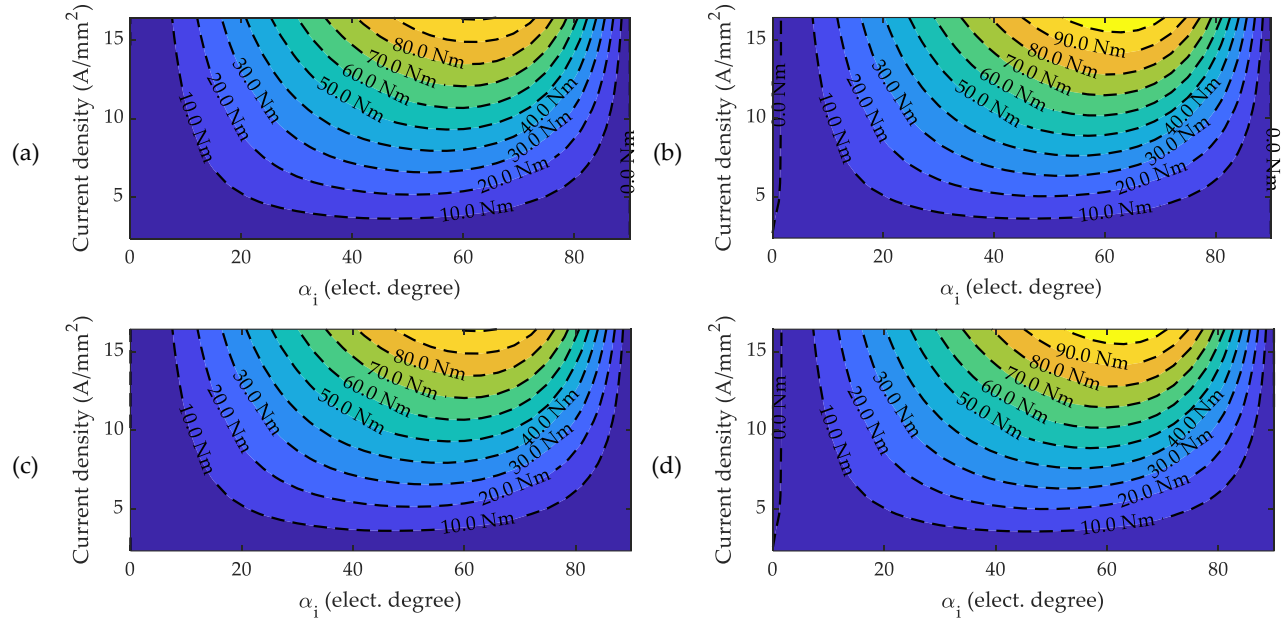


**Figure 5.11.** Mean torque for the symmetric and asymmetric design. (a) symmetric design counter-clockwise rotation; (b) asymmetric design counter-clockwise rotation; (c) symmetric design clockwise rotation; (d) asymmetric design clockwise rotation.

The greatest differences are observed in the average torque and torque ripple. The asymmetrical design presents a slightly larger zone of maximum power factor and saliency ratio, compared to the symmetrical design. However, the symmetrical design has a lower torque ripple at low current density levels. Despite both designs reaching a torque ripple of 20% in their respective areas of lowest torque ripple, for electromobility applications a ripple of less than 5% is desired [15]. To choose a suitable skew angle for reducing the torque ripple to acceptable values, a FFT was performed on the electromagnetic torque. The harmonic components of both designs under different load conditions are shown in Figure 5.12 and Figure 5.13 for counter-clockwise and clockwise rotation, respectively.

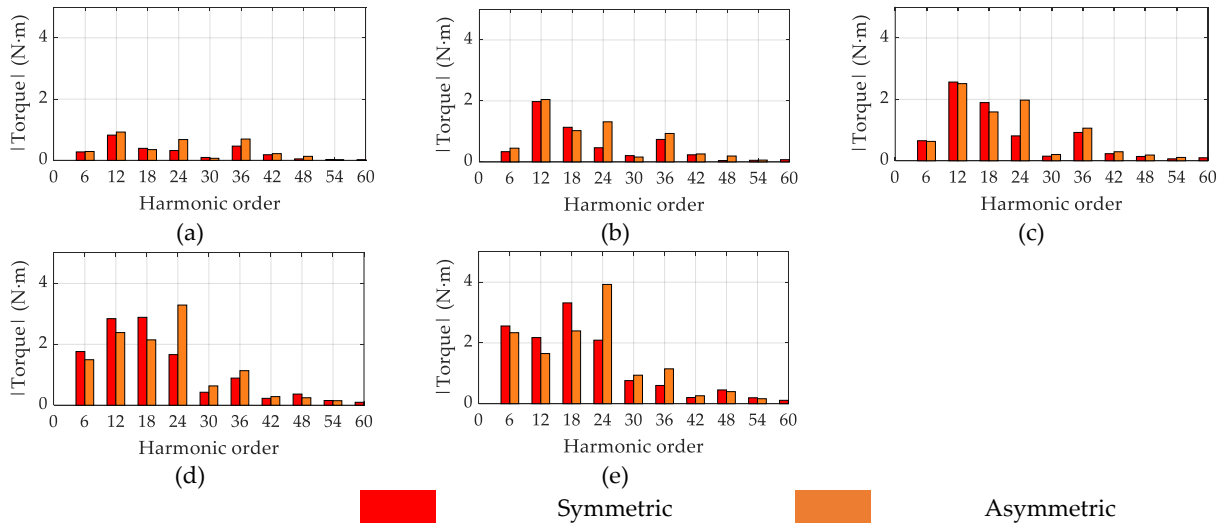


**Figure 5.12.** Harmonic components of the electromagnetic torque for the optimum symmetric and asymmetric design counter-clockwise rotation; (a) current density 5 A/mm<sup>2</sup>; (b) current density 7.5 A/mm<sup>2</sup>; (c) current density 10 A/mm<sup>2</sup>; (d) current density 12.5 A/mm<sup>2</sup>; (e) current density 15 A/mm<sup>2</sup>.



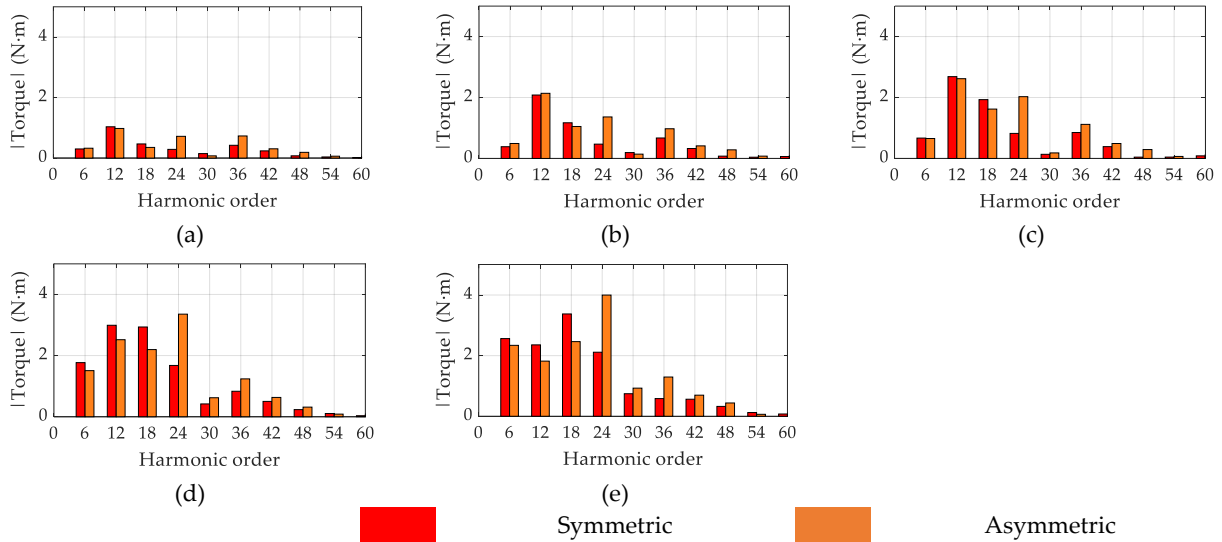


**Figure 5.13.** Harmonic components of the electromagnetic torque for the optimum symmetric and asymmetric design clockwise rotation; (a) current density 5 A/mm<sup>2</sup>; (b) current density 7.5 A/mm<sup>2</sup>; (c) current density 10 A/mm<sup>2</sup>; (d) current density 12.5 A/mm<sup>2</sup>; (e) current density 15 A/mm<sup>2</sup>.

Both rotational directions show similar magnitudes of harmonic components. When the current density is below 10 A/mm<sup>2</sup>, the 12-nd harmonic is the dominant one, which is caused by the stator slotting. When the current density is above 10 A/mm<sup>2</sup>, the 18-th harmonic is dominant in the symmetrical design and the 24-th harmonic in the asymmetrical design. Table 5.4 shows the skew angle that can be used to mitigate specific harmonics component, which was calculated using equation 4.4. This analysis considered the 6-th, 12-nd, and 18-th harmonics for mitigation using 2-step, 3-step, 4-step, and 5-step skewing.

**Table 5.4.** Skew angle to reduce a specific harmonic component of the electromagnetic torque.

Harmonic order	Mechanical angle for 2-step skew	Mechanical angle for 3-step skew	Mechanical angle for 4-step skew	Mechanical angle for 5-step skew
6 <sup>th</sup>	10°	6.66°	5°	4°
12 <sup>nd</sup>	5°	3.33°	2.5°	2°
18 <sup>th</sup>	3.33°	2.22°	1.66°	1.33°

The harmonic distribution of the electromagnetic torque increases with increasing current density, so it is desirable to apply skew to reduce these harmonics. The mitigation factor (defined in Chapter IV by equation 4.9) can be used to determine the reduction of each harmonic component. Tables 5.5, 5.6, and 5.7 report the mitigation factor when the skew is applied to the 6-th, 12-nd, and 18-th harmonics, respectively.

**Table 5.5.** Value of the mitigation factor when the first harmonic component is selected to reduce ( $w = 6$ ).

Harmonic order	$k_{rs,v}$			
	Mechanical angle for 2-step skew	Mechanical angle for 3-step skew	Mechanical angle for 4-step skew	Mechanical angle for 5-step skew
6 <sup>th</sup>	0	0	0	0
12 <sup>nd</sup>	1	0	0	0
18 <sup>th</sup>	0	1	0	0
24 <sup>th</sup>	1	0	1	0

**Table 6.6.** Value of the mitigation factor when the second harmonic component is selected to reduce ( $w = 12$ ).

Harmonic order	$k_{rs,v}$			
	Mechanical angle for 2-step skew	Mechanical angle for 3-step skew	Mechanical angle for 4-step skew	Mechanical angle for 5-step skew
6 <sup>th</sup>	0.7	0.6	0.6	0.6
12 <sup>nd</sup>	0	0	0	0
18 <sup>th</sup>	0.7	0.3	0.3	0.2
24 <sup>th</sup>	1	0	0	0

**Table 6.7.** Value of the mitigation factor when the third harmonic component is selected to reduce ( $w = 18$ ).

Harmonic order	$k_{rs,v}$			
	Mechanical angle for 2-step skew	Mechanical angle for 3-step skew	Mechanical angle for 4-step skew	Mechanical angle for 5-step skew
6 <sup>th</sup>	0.8	0.8	0.8	0.8
12 <sup>nd</sup>	0.5	0.4	0.4	0.4
18 <sup>th</sup>	0	0	0	0
24 <sup>th</sup>	0.5	0.3	0.2	0.2

The analysis shows that the best option for applying skew is to mitigate the 6-th harmonic using a 5-step skew. This eliminates the harmonic components theoretically, but in practice, the reduction is not complete. Figures 5.14 and 5.15 show the harmonic components of the optimal symmetrical and asymmetrical designs for counter-clockwise and clockwise rotation, respectively, with a 5-step skew applied.

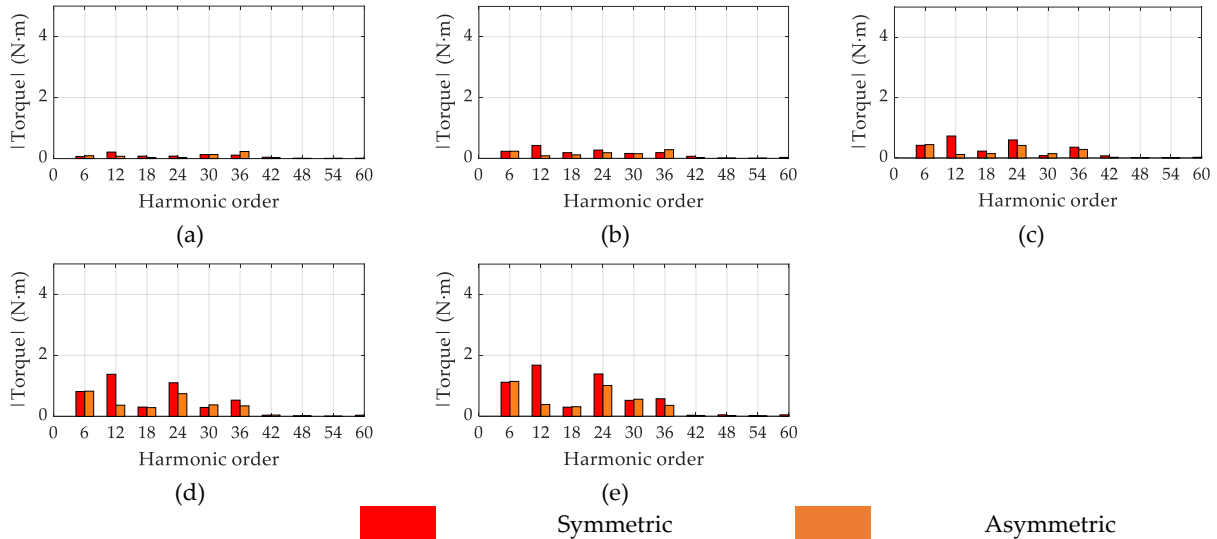


**Figure 5.14.** Harmonic components of the electromagnetic torque for the optimum symmetric and asymmetric design applying four step skew and counter-clockwise rotation; (a) current density 5 A/mm<sup>2</sup>; (b) current density 7.5 A/mm<sup>2</sup>; (c) current density 10 A/mm<sup>2</sup>; (d) current density 12.5 A/mm<sup>2</sup>; (e) current density 15 A/mm<sup>2</sup>.

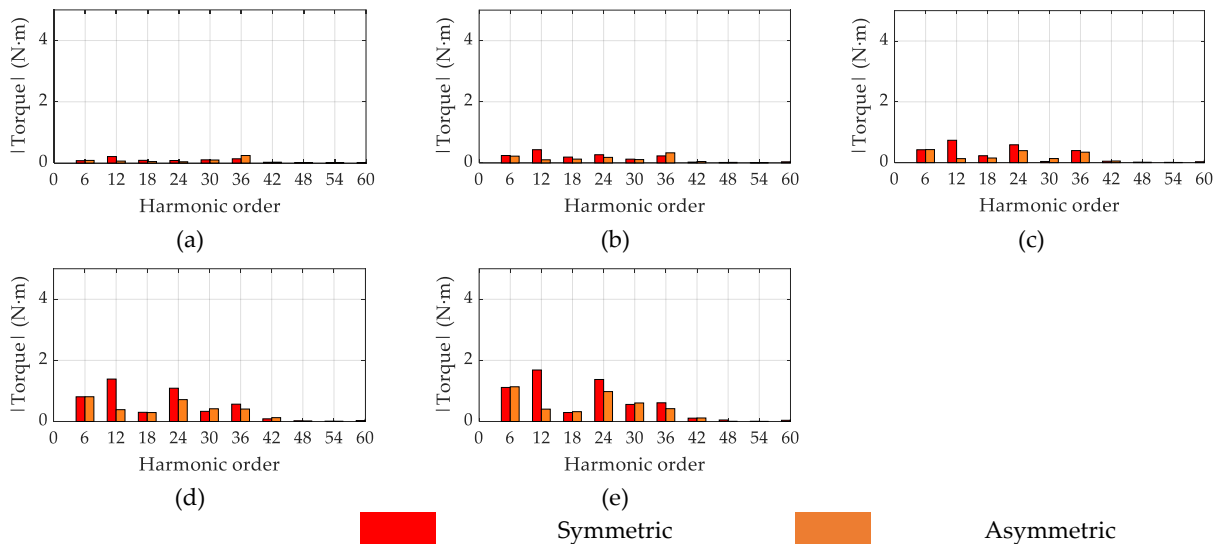


**Figure 5.15.** Harmonic components of the electromagnetic torque for the optimum symmetric and asymmetric design applying four step skew and clockwise rotation; (a) current density 5 A/mm<sup>2</sup>; (b) current density 7.5 A/mm<sup>2</sup>; (c) current density 10 A/mm<sup>2</sup>; (d) current density 12.5 A/mm<sup>2</sup>; (e) current density 15 A/mm<sup>2</sup>.

In both rotational directions, the magnitude of the harmonic components is similar when a 5-step skew is applied. When the current density is below 10 A/mm<sup>2</sup>, the predominant harmonic component is the 12-nd, corresponding to the stator slotting. However, when the current density is greater than 10 A/mm<sup>2</sup>, the predominant harmonic component remains the 12-nd, differing from the behavior of the skewless model.

Although the mitigation factor suggests that the first to fourth harmonic components should be reduced to zero, in practice this is not achieved. The reduction of the harmonic components is approximately 50%, and the reduction is greater in the asymmetric design. The greater reduction in

the harmonic component in the asymmetric design is due to the asymmetrical positioning of the flux barriers, which provides additional contribution in mitigating the spatial harmonic components in the electromagnetic torque.

Figures 5.16, 5.17, 5.18 and 5.19 show the contour maps for the optimal symmetric and asymmetric designs, respectively, for counter-clockwise and clockwise rotation, with a 5-step skew applied, for the main performance indexes.

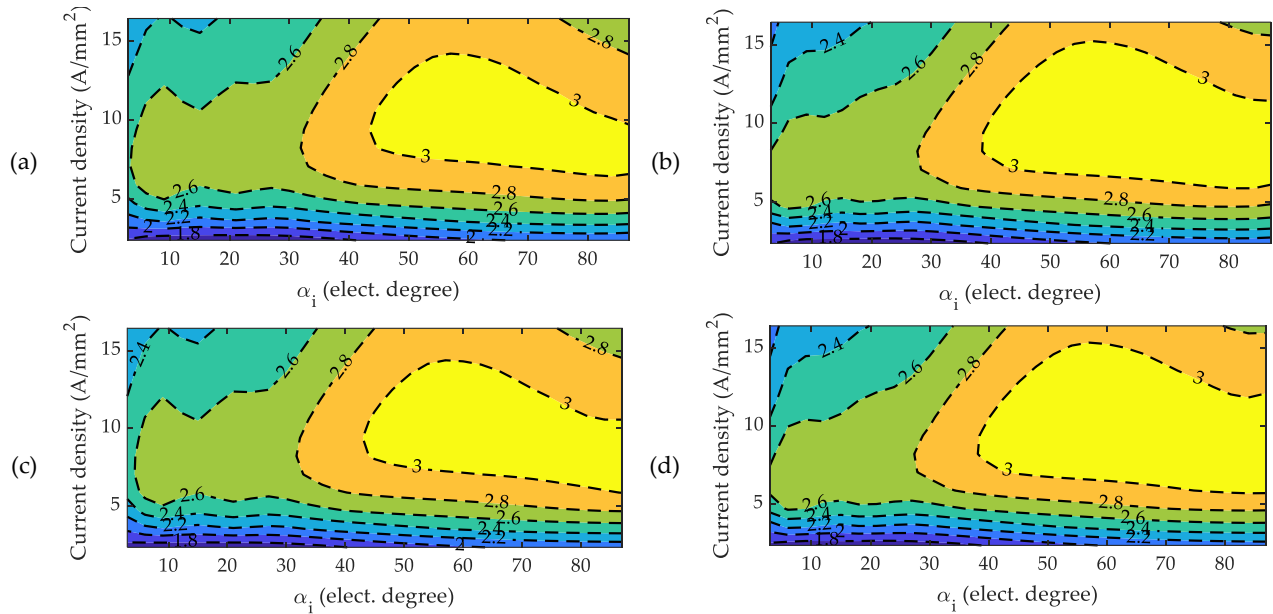


**Figure 5.16.** Saliency ratio for the symmetric and asymmetric design with four step skew is applied. (a) symmetric design counter-clockwise rotation; (b) asymmetric design counter-clockwise rotation; (c) symmetric design clockwise rotation; (d) asymmetric design clockwise rotation.

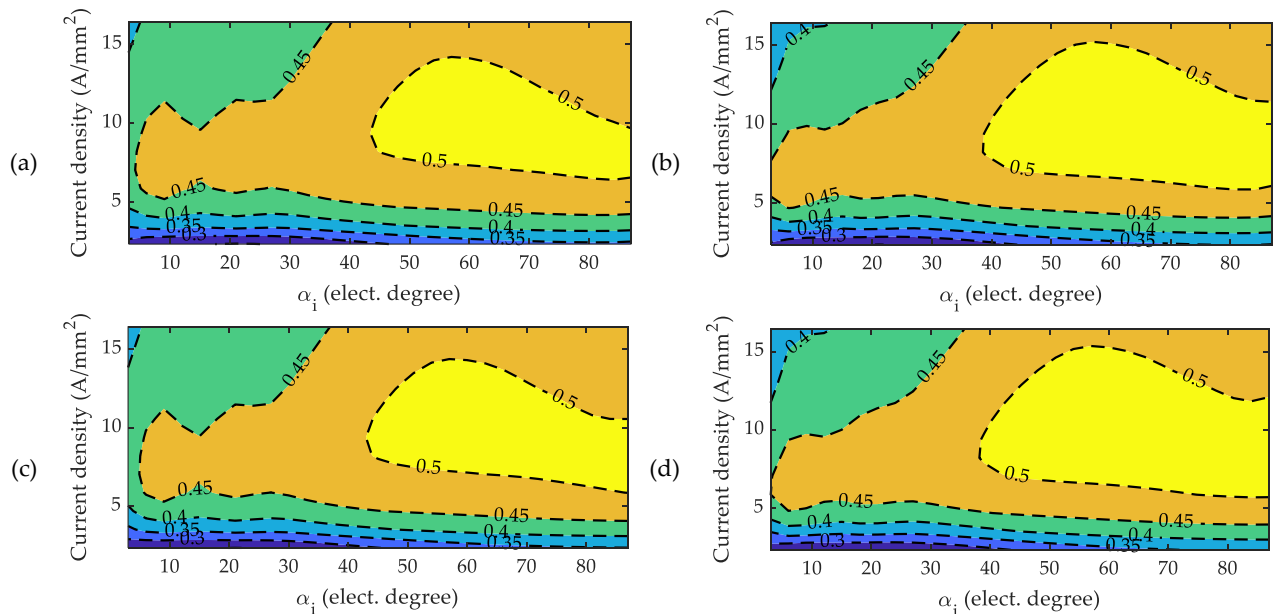


**Figure 5.17.** Internal power factor for the symmetric and asymmetric design with four step skew is applied. (a) symmetric design counter-clockwise rotation; (b) asymmetric design counter-clockwise rotation; (c) symmetric design clockwise rotation; (d) asymmetric design clockwise rotation.

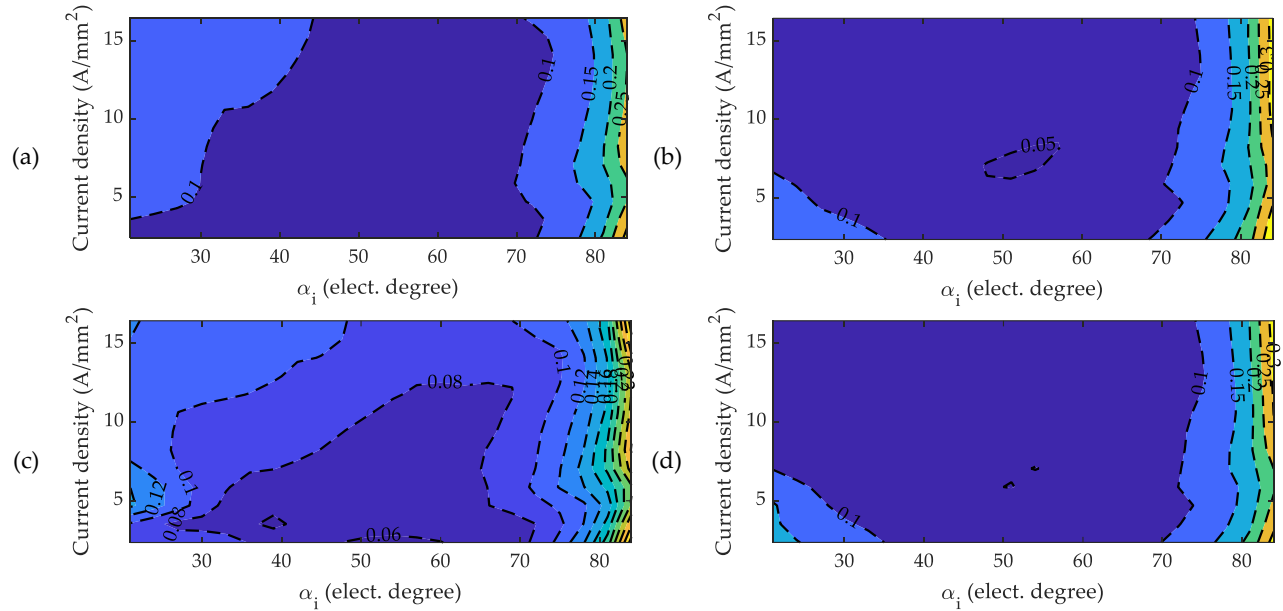


**Figure 5.18.** Torque ripple for the symmetric and asymmetric design with four step skew is applied. (a) symmetric design counter-clockwise rotation; (b) asymmetric design counter-clockwise rotation; (c) symmetric design clockwise rotation; (d) asymmetric design clockwise rotation.

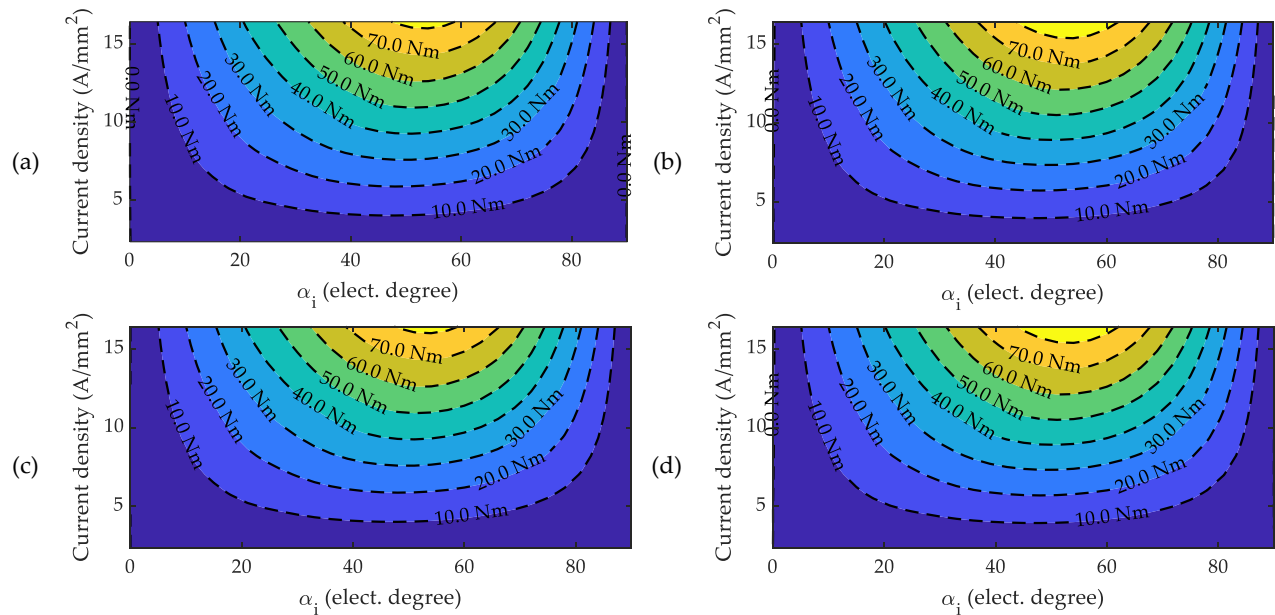


**Figure 5.19.** Mean torque for the symmetric and asymmetric design with four step skew is applied. (a) symmetric design counter-clockwise rotation; (b) asymmetric design counter-clockwise rotation; (c) symmetric design clockwise rotation; (d) asymmetric design clockwise rotation.

The greatest differences are observed in the average torque and torque ripple. The asymmetric design has a larger zone of maximum internal power factor and saliency ratio and can develop higher mean torque than the symmetrical design with lower torque ripple. In both rotational directions, the region with torque ripple less than 10% is larger in the asymmetric design, reaching less than 5% when rotated counter-clockwise.

Figure 5.20 depict the overlay of the contour curves of internal power factor, torque ripple, and mean torque over a specific range of current density and current angle for counter-clockwise rotation in symmetric and asymmetric designs, respectively. Two operating points in the MTPA trajectory corresponding to 5 A/mm<sup>2</sup> for the inverted blue triangle and 10 A/mm<sup>2</sup> for the red triangle have been highlighted in the figure. The performance indices for the defined operation points are listed in table 5.8. The internal power factor and efficiency values are comparable between the symmetric and asymmetric designs. The main difference between the symmetric and asymmetric designs is found in the average torque and torque ripple, where the asymmetric design yields a 25% reduction in torque ripple and a 5% increase in average torque compared to the symmetric design.

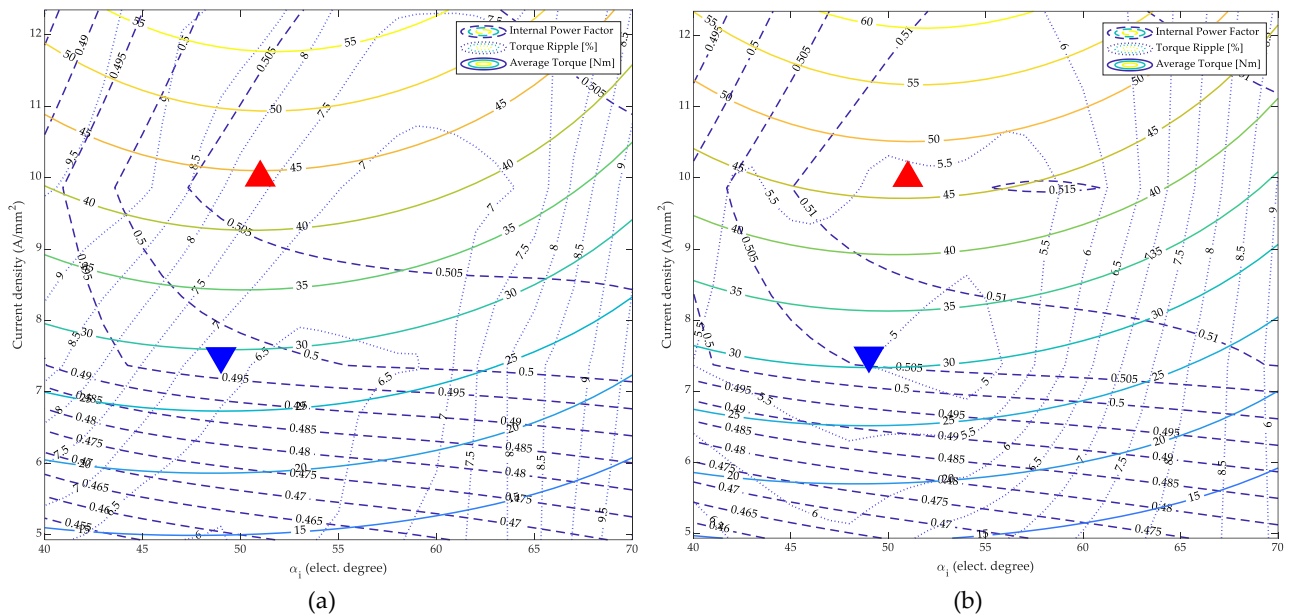


**Figure 5.20.** Superposition of the contour curves of the main performance indices over a certain range of current density and current angle with counter-clockwise rotation. Two operating points were defined for MTPA for 7.5 A/mm<sup>2</sup> and 10 A/mm<sup>2</sup>. (a) symmetric design; (b) asymmetric design.

**Table 5.8.** Performance indices for the operating points defined in Figure 5.20 for the symmetrical and asymmetrical designs when the machine rotated counter-clockwise.



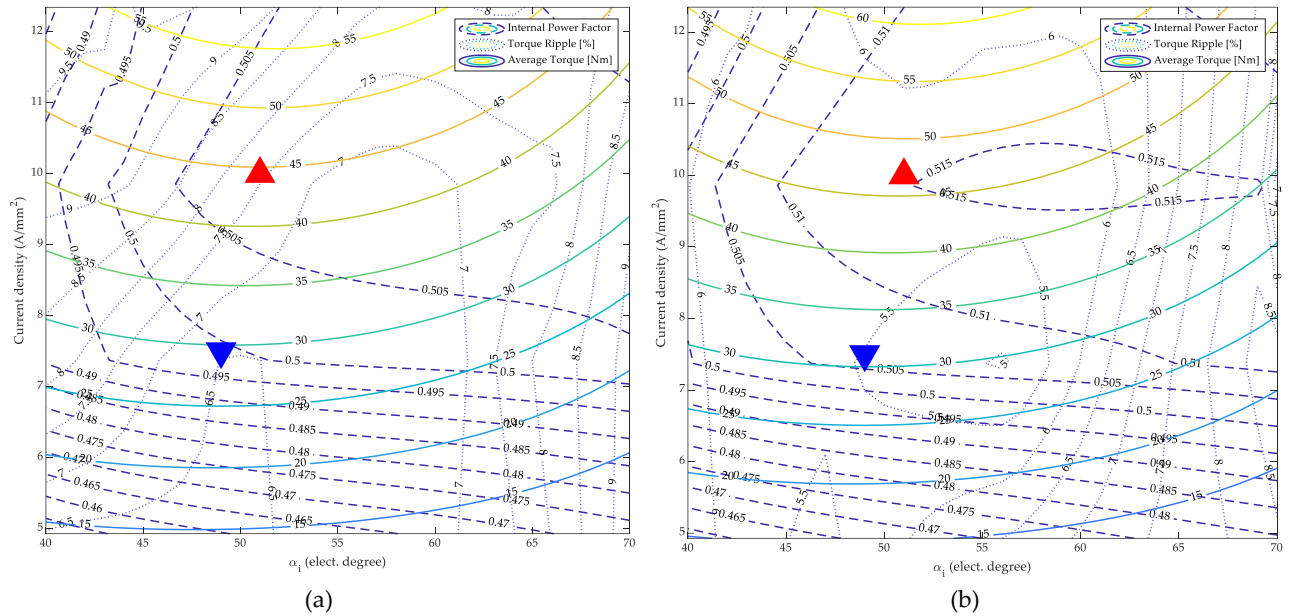
Operation point	Symmetric						Asymmetric					
	IPF	T <sub>avg</sub> [Nm]	T <sub>rp</sub> [%]	P [kW]	(P <sub>cu</sub> + P <sub>fe</sub> ) [kW]	η [%]	IPF	T <sub>avg</sub> [Nm]	T <sub>rp</sub> [%]	P [kW]	(P <sub>cu</sub> + P <sub>fe</sub> ) [kW]	η [%]
	0.49	28.7	6.7	15.0	1.7	88.3	0.51	30.2	4.9	15.8	1.8	88.4
	0.51	43.6	7.5	22.8	2.3	89.4	0.51	45.9	5.4	24.0	2.4	89.6

Figure 5.21 show the overlap of contour curves for internal power factor, torque ripple, and mean torque within a specified range of current density and current angle for the symmetric and asymmetric design for clockwise rotation, respectively. Two operating points in the MTPA trajectory corresponding to 5 A/mm<sup>2</sup> for the inverted blue triangle and 10 A/mm<sup>2</sup> for the red triangle have been highlighted in the figure. The performance indices for the defined operation points are listed in table 5.9. Similar to counter-clockwise rotation, the power factor and efficiency values are nearly equal between symmetrical and asymmetrical designs. The major distinction lies in the average torque and

torque ripple, where the asymmetrical design offers a 20% reduction in torque ripple and a 5% increase in average torque compared to the symmetrical design.



**Figure 5.21.** Superposition of the contour curves of the main performance indices over a certain range of current density and current angle with clockwise rotation. Two operating points were defined for MTPA for 7.5 A/mm<sup>2</sup> and 10 A/mm<sup>2</sup>. (a) symmetric design; (b) asymmetric design.

**Table 5.9.** Performance indices for the operating points defined in Figure 5.21 for the symmetrical and asymmetrical designs when the machine rotated clockwise.

Operation point	Symmetric						Asymmetric					
	IPF	T <sub>avg</sub> [Nm]	T <sub>rp</sub> [%]	P [kW]	(P <sub>cu</sub> + P <sub>fe</sub> ) [kW]	η [%]	IPF	T <sub>avg</sub> [Nm]	T <sub>rp</sub> [%]	P [kW]	(P <sub>cu</sub> + P <sub>fe</sub> ) [kW]	η [%]
	0.5	28.7	6.5	15.0	1.7	88.3	0.51	30.3	5.5	15.8	1.8	88.3
	0.51	43.6	7.5	22.8	2.3	89.4	0.51	45.9	5.8	24	2.4	89.6

The electromagnetic torque waveform as a function of rotor position is shown in Figure 5.22 for both symmetrical and asymmetrical designs in counter-clockwise rotation. It is evident from the figure that the asymmetric design produces a higher average torque than the symmetrical one. When skew is not applied, the torque ripple in both designs is comparable. However, with the application of skew, the asymmetric design developed lower torque ripple than the symmetrical one, but the average torque is compromised in both designs.

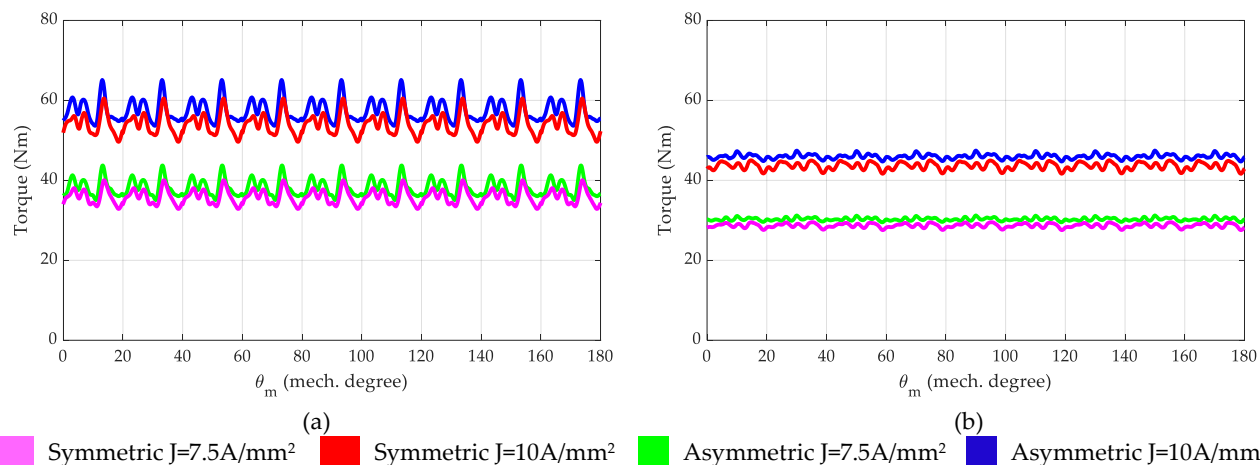


**Figure 5.22.** Symmetric and asymmetric design electromagnetic torque waveform for MTPA when the current density is  $7.5\text{ A/mm}^2$  and  $10\text{ A/mm}^2$  and the machine rotated counter-clockwise. (a) skewless designs; (b) 5-step skew designs.

The magnetic field distribution of the designs is shown in Figures 5.23 and 5.24 for  $7.5\text{ A/mm}^2$  and  $10\text{ A/mm}^2$ , respectively. It is seen that the highest levels of saturation are found in the end-point parts of the barriers and ducts what is expected in this topology of machines. In general, both machines operate near the saturation knee of the B-H curve, taking advantage of the magnetic properties of the material.

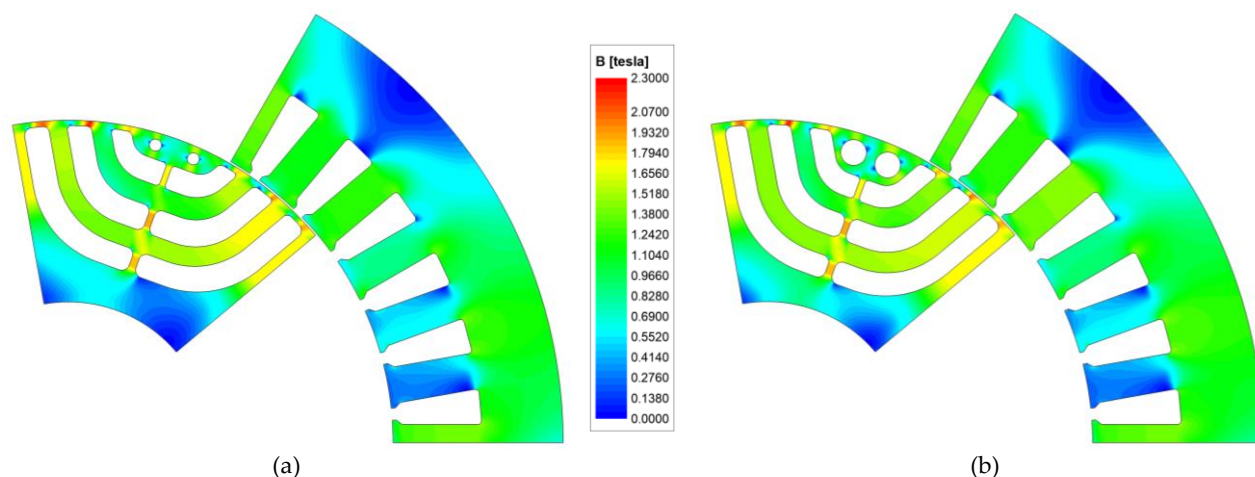


**Figure 5.23.** Magnetic flux density distribution for the optimal designs for MTPA at  $7.5\text{ A/mm}^2$ . (a) symmetric design counter-clockwise rotation; (b) asymmetric design counter-clockwise rotation.



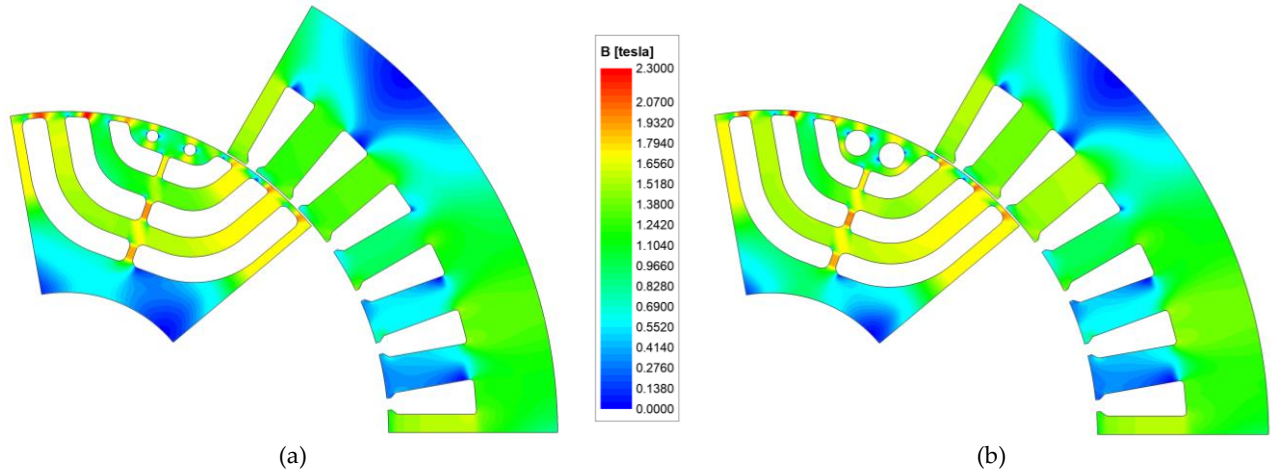


**Figure 5.24.** Magnetic flux density distribution for the optimal design for MTPA at 10 A/mm<sup>2</sup>. (a) symmetric design counter-clockwise rotation; (b) asymmetric design counter-clockwise rotation.

### 5.5. Impact of rotor skewing on the performance of the machine

Figures 5.25 and 5.26 illustrate the impact of applying skew on different performance indices of a SynRM, for both symmetric and asymmetric designs, as a function of the supply current density. The results reveal that applying skew significantly reduces all machine indices in both scenarios. In a SynRM, saliency ratio is a critical parameter that directly affects electromagnetic torque, power factor, and efficiency. However, the saliency ratio decreases by more than 20% for all current values when skew is applied to the rotor, leading to a decrease in IPF and mean torque of the machine, as shown in Figures 5.25 and 5.26 (c) and (d), respectively. Furthermore, torque ripple is significantly reduced for both designs, achieving a reduction of around 60% and 70% for the symmetric and asymmetric designs, respectively, at 10 A/mm<sup>2</sup>. The asymmetric design offers a lower torque ripple for all current density levels when skew is applied. The efficiency is also slightly affected by the application of skew in both designs.

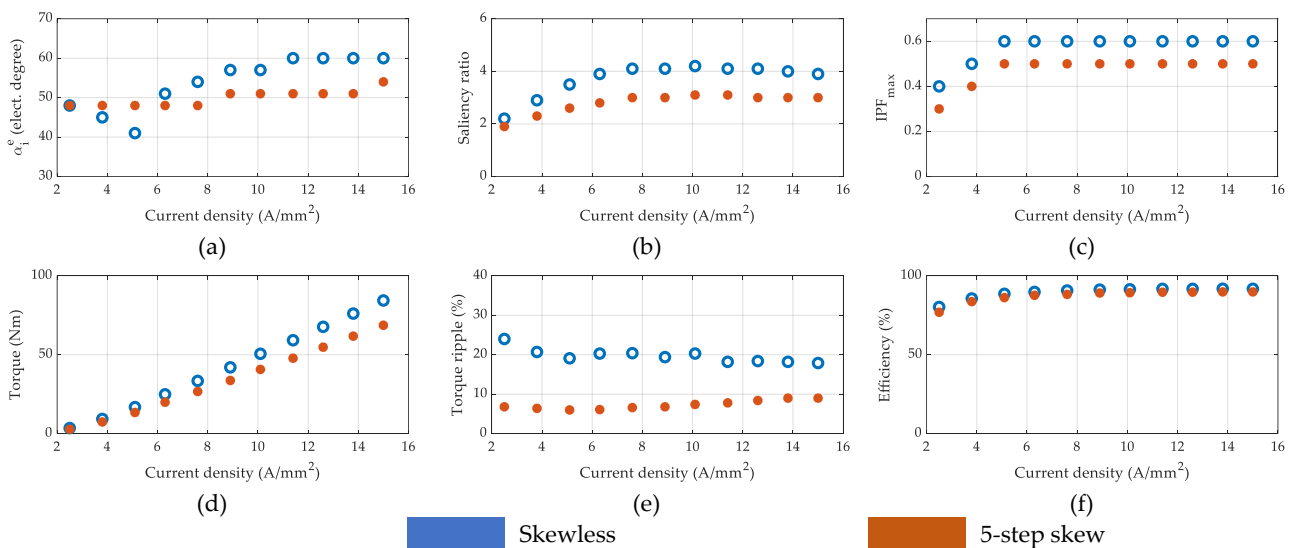


**Figure 5.25.** Performance indices for the symmetric design for MTPA for different current density levels. (a) current angle; (b) saliency ratio; (c) maximum internal power factor; (d) average torque; (e) torque ripple; (f) efficiency.

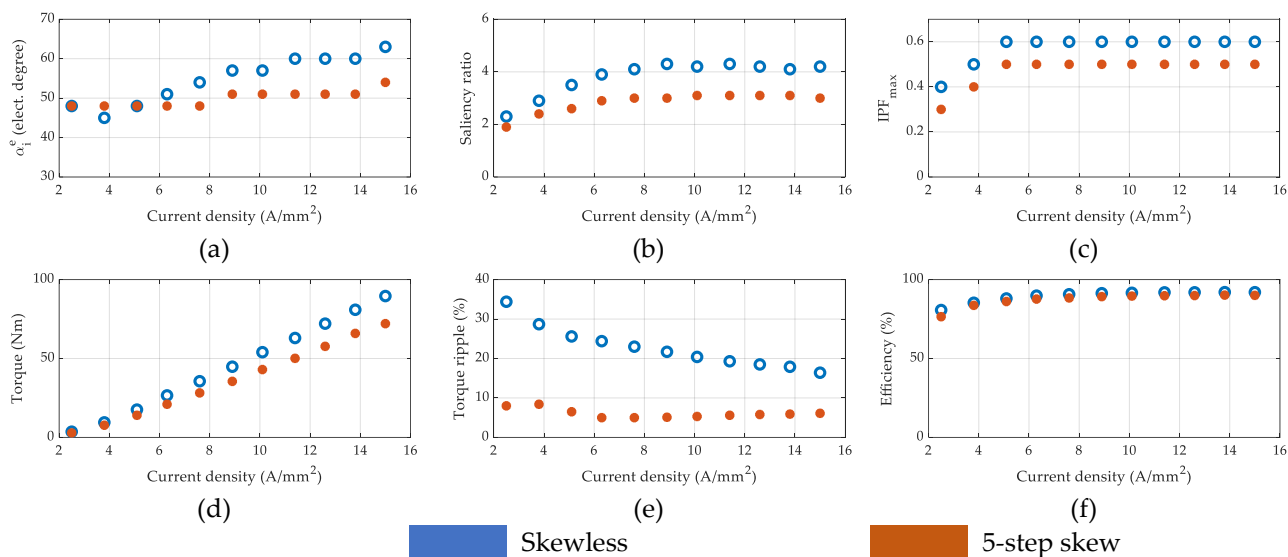


**Figure 5.26.** Performance indices for the asymmetric design for MTPA for different current density levels. (a) current angle; (b) saliency ratio; (c) maximum internal power factor; (d) average torque; (e) torque ripple; (f) efficiency.

The development of SynRM with a higher saliency ratio is a critical factor for expanding the motor's application in various fields, including electric vehicles, as it enables the development of a larger CPSR. Typically, the CPSR is dependent on the saliency ratio, which underscores the importance of designing a motor with an improved saliency ratio to broaden the application of SynRM. Figure 5.27 confirms that a decrease in the saliency ratio leads to a decrease in the CPSR. Furthermore, applying 5-step skew leads to a reduction in the machine's torque and power across all speeds.

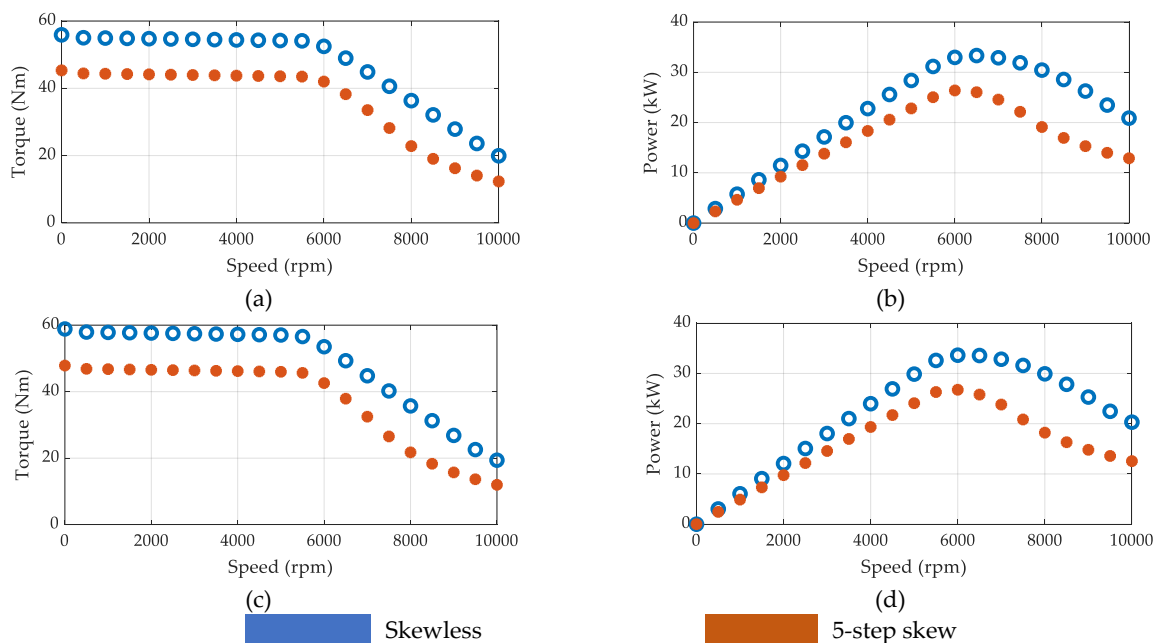


**Figure 5.27.** CPSR performance for the symmetric and asymmetric design for maximum current density of 10A/mm<sup>2</sup>. (a) torque vs. speed for the symmetric design; (b) power vs. speed for the symmetric design; (c) torque vs. speed for the asymmetric design; (d) power vs. speed for the asymmetric design.

To assess the performance strength of the studied designs, an efficiency map for each design was created using ANSYS Electronic Desktop's Machine-Toolkit. The machine was supplied with DC bus voltage of 600 V and operated for MTPA at a maximum current density of 10 A/mm<sup>2</sup>. The efficiency maps are presented in Figure 5.28 for the analyzed rotor structures for counter-clockwise rotation.

Figure 5.28 shows that the efficiency is also reduced when skewing is applied. This occurs because the machine produces less power at the shaft for a given input power, as a result of cross-coupling between the various modules and leakage between each slice. Both designs exhibit a similar behavior, reaching 96% efficiency for the skewless machine and 95% for the 5-step skew machine at the rated speed.

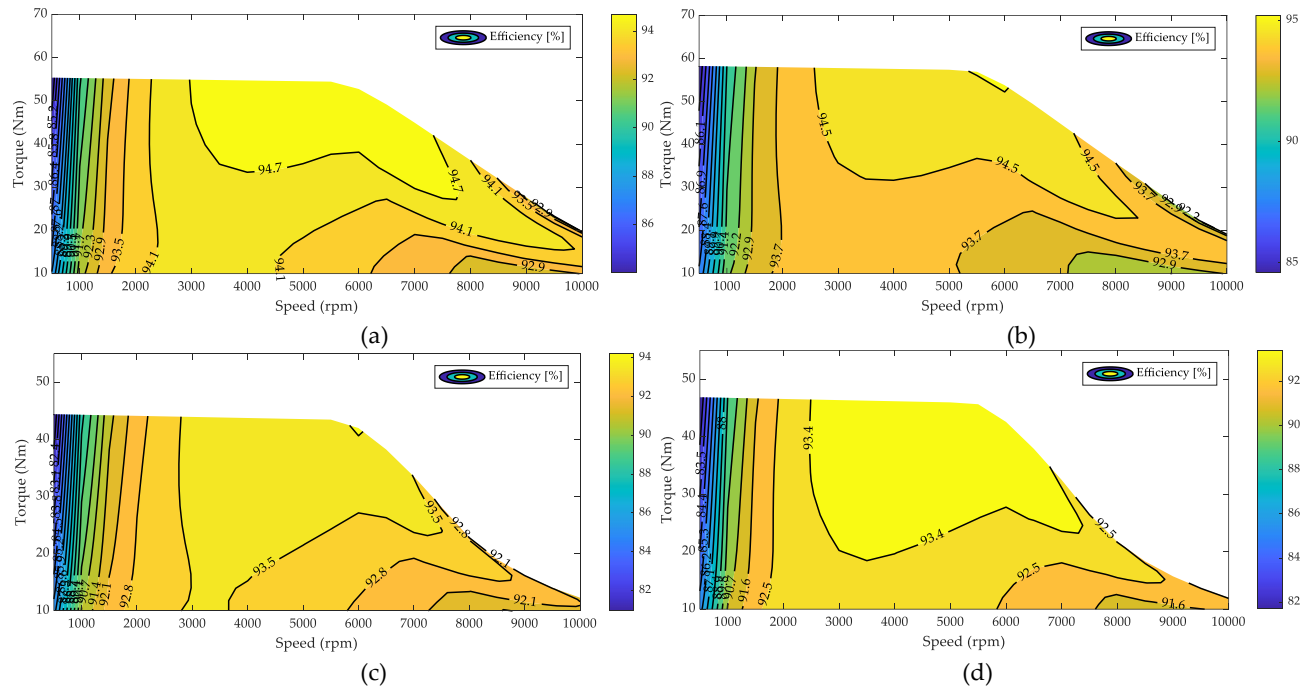


**Figure 5.28.** Efficiency map when the machine is operated a MTPA for a maximum current density of 10A/mm<sup>2</sup>. (a) skewless symmetric design; (b) skewless asymmetric design; (c) 5-step skew symmetric design; (d) 5-step skew asymmetric design.

### 5.6. Manufactured prototype

Figure 5.29 presents a view of the motor's components. The stator and rotor cores are constructed from 0.35 mm non-oriented silicon steel M350-35A laminations and feature 36 slots housing a three-phase single-layer distributed winding. The winding is configured with 6 turns, with each turn consisting of 10 parallel wires, resulting in a fill factor of ~0.45.

To maintain safe operating temperatures for the motor, the housing incorporates a spiral water jacket, ensuring efficient heat dissipation. The housing itself is constructed from aluminum, which not only enhances heat transfer capabilities but also reduces the overall weight of the motor. This combination of materials and design elements contributes to the motor's optimal performance and life-time.

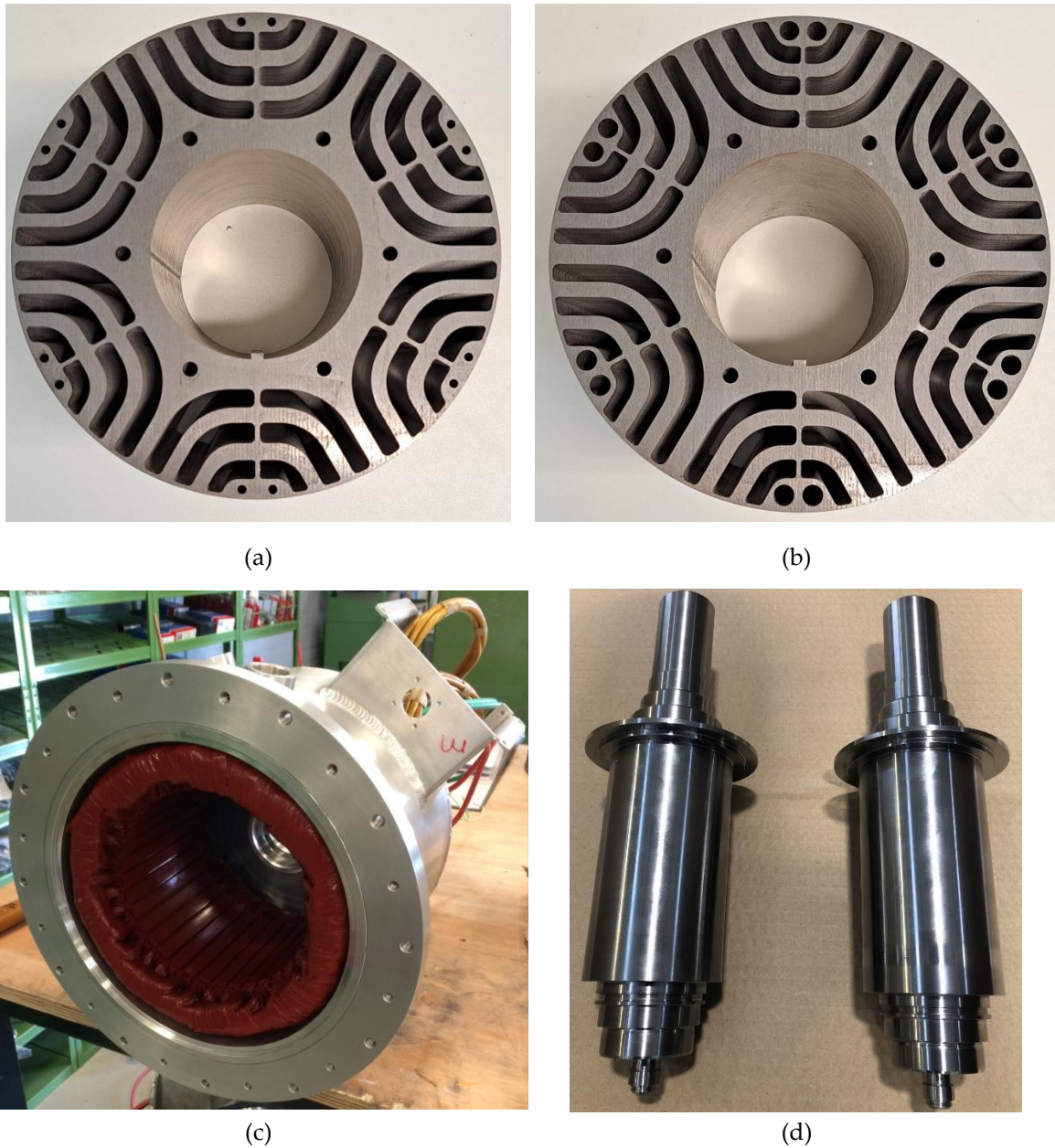


**Figure 5.29.** Exploded view of the motor assembly. (a) asymmetric rotor; (b) asymmetric rotor; (c) stator lamination and winding assembled in the housing (jacket water); (d) shaft.

### 5.7. Summary

This chapter described the design tools used to create symmetrical and asymmetrical rotor models for a SynRM using the same stator. An optimization was performed using MOGA and FEM simulations to obtain the designs, and discrete skew was applied in 5-steps to reduce torque ripple. The contour maps of the main performance indices for both designs show that the asymmetric design is superior in terms of average torque and torque ripple for specific operating points. The optimal designs were evaluated mechanically to ensure the rotor's mechanical integrity and conform to standards for a maximum speed of 10,000 rpm. The magnetic flux density was illustrated in both designs and showed that saturation levels occur in the end-point parts of the barriers and ducts. The influence of applying skew on the performance of symmetric and asymmetric models was analyzed.

It is possible to observe that most of the performance indexes decrease when skew is applied on the rotor structure, but also a reduction of more than 50% in the torque ripple is achieved. Both machines had similar efficiency, but the asymmetric design generated more torque under the torque-speed curve. Finally, a first view of the prototype is presented, highlighting its different parts and materials.

## 6. Conclusions and future work

### 6.1. Conclusion

The main aim of this thesis is to offer a comprehensive understanding of Synchronous Reluctance Machines (SynRMs), addressing both the fundamental principles of operation and the development of various design techniques. The research conducted in this thesis has successfully contributed to the enhancement of SynRMs' performance by developing design techniques and guidelines that primarily focus on increasing rotor anisotropy. Through the optimization of rotor design, the potential for significant improvements in machine efficiency and overall performance was demonstrated.

The incorporation of an analytical model in the electric machine design process is an effective means to simplifying the design and save valuable time. A significant achievement of this study is the development and validation of a precise analytical model for SynRMs. This model combines two approaches: the calculation of air-gap flux density and average torque employs the magnetic potential of both the rotor and stator, while torque ripple is determined by assessing the energy stored in the air-gap. This model is also adaptable for machines featuring multiple flux barriers.

Comparisons with Finite Element Analysis (FEA) have produced promising results, particularly in terms of air-gap flux density and electromagnetic torque. However, a harmonic analysis has revealed that the analytical model tends to overestimate air-gap flux density and torque due to certain underlying assumptions made during its development. Nevertheless, the model offers valuable functionalities, including the capacity to extract machine parameters within the  $d$ - $q$  reference frame, facilitating preliminary control strategy analysis. This model equips designers and researchers with a valuable tool for predicting the machine's performance under various operational conditions, thereby speeding up the design and analysis process.

The findings of this work demonstrate that an asymmetrical rotor structure in a SynRM provides better performance than a symmetrical rotor structure. The advantage of the asymmetric rotor structure with respect to machine behavior varies depending on the design technique employed. By selecting different machine parameters during the optimization phase, it is possible to enhance various performance indices. The position and opening of the flux barrier in the air-gap govern torque ripple, while the thickness of the flux barriers along the  $q$ -axis regulates mean torque. Combining all these parameters with the current angle improves the power factor when the maximum torque is achieved at a larger current angle. This analysis was conducted in the context of two different SynRM topologies. The first one featured a 48-slot, 2-pole pairs configuration with 2 flux barriers per pole, and the other was a 36-slot, 3-pole pairs configuration with 3 flux barriers per pole.

In both cases, the asymmetric design managed torque ripple more effectively due to its ability to cancel air-gap harmonics, while the mean torque remained relatively stable. However, in the 48-slot topology, there was only a slight improvement in the power factor since it was selected as the objective function during the optimization stage. By quantifying the impact of these asymmetries in each topology, a deeper understanding of the machine's behavior was gained, enabling more precise design decisions to be made.

The imperative of achieving less than 15% torque ripple in electromobility applications necessitated the implementation of skew in the design of the two rotor prototypes. To address this challenge, a study on the discrete-skew methodology was conducted, and a method was proposed

to gain a deeper understanding of the impact of skewing angle and its determination during the SynRM design phase. This method takes into account the influence on all torque harmonic components and offers a means to visualize the reduction of specific undesired harmonic content. A skew reduction factor was introduced, which theoretically inform the potential of the method to completely eliminate a desired harmonic component. However, in practical application, complete elimination is not feasible, and the reduction of the selected harmonic component is usually around 80%.

By applying this technique during the design phase of the prototypes, it becomes possible to ensure that torque ripple remains below 15% for nearly all the operation points analyzed. Nevertheless, a significant reduction in mean torque is observed when skewing is applied. The reduction is not limited to the desired harmonic component; rather, it extends to the other remaining components. Furthermore, the cross-coupling effect between the  $q$ -axis and  $d$ -axis is amplified, and a new phenomenon of cross-coupling effect emerges between the different sections into which the rotor is divided for skew application. For both rotor structures, the application of skewing techniques results in an approximate 20% reduction in mean torque compared to the skewless machine. The saliency ratio and the power factor are also reduced by applying skew, but the efficiency doesn't show a remarkable change. An important fact in applying this technique is that it is not necessary to use 3D FEA simulation for its application, 2D FEA is effective in predicting the optimal step skewing which allows a considerable time-saving in the design stage.

### 6.2. Future work

A critical aspect of this thesis involved analyzing and comparing the performance of SynRM with enhanced rotor anisotropy, incorporating asymmetries, against traditional designs across various operating conditions. Our findings have clearly demonstrated the superior performance of the optimized designs, highlighting the advantages of rotor asymmetries in enhancing machine efficiency.

The practical feasibility of the optimized SynRM designs, including rotor asymmetries, was rigorously validated through FEA and the next step is the experimental testing of the prototypes. Two rotor structures sharing a common stator were built for the experimental tests. This validation will confirm that the proposed design techniques are not only theoretically sound but also real-world applicable, thus offering engineers and designers reliable solutions for improving machine performance.

To validate the analytical model, a unique rotor prototype without bridges at the flux barriers was fabricated and installed on an induction machine stator. The absence of the required tools for measuring torque ripple has delayed the validation of the model through experimental testing. However, I anticipate being able to conduct this experiment in the near future. Another essential feature that is needed for improved results, particularly in the context of SynRMs, is the incorporation of saturation into the analytical model.

The incorporation of modulation techniques to eliminate combinations of harmonic components and reduce torque ripple without impacting the mean torque can be integrated as an additional feature into the skew method developed in the thesis.

## References

- [1] M. U. Naseer, A. Kallaste, B. Asad, T. Vaimann, and A. Rassõlkin, "Analytical modelling of synchronous reluctance motor including non-linear magnetic condition," *IET Electr Power Appl*, vol. 16, no. 4, pp. 511–524, Apr. 2022, doi: 10.1049/ELP2.12172.
- [2] M. N. F. Ibrahim, A. S. Abdel-Khalik, E. M. Rashad, and P. Sergeant, "An Improved Torque Density Synchronous Reluctance Machine With a Combined Star-Delta Winding Layout," *IEEE Transactions on Energy Conversion*, vol. 33, no. 3, pp. 1015–1024, Sep. 2018, doi: 10.1109/TEC.2017.2782777.
- [3] K. B. Tawfiq, M. N. Ibrahim, E. E. El-Kholy, and P. Sergeant, "Performance Improvement of Synchronous Reluctance Machines—A Review Research," *IEEE Trans Magn*, vol. 57, no. 10, pp. 1–11, Oct. 2021, doi: 10.1109/TMAG.2021.3108634.
- [4] M. Murataliyev, M. Degano, M. Di Nardo, N. Bianchi, and C. Gerada, "Synchronous Reluctance Machines: A Comprehensive Review and Technology Comparison," *Proceedings of the IEEE*, vol. 110, no. 3, pp. 382–399, Mar. 2022, doi: 10.1109/JPROC.2022.3145662.
- [5] D. Gerada, A. Mebarki, N. L. Brown, C. Gerada, A. Cavagnino, and A. Boglietti, "High-speed electrical machines: Technologies, trends, and developments," *IEEE Transactions on Industrial Electronics*, vol. 61, no. 6, pp. 2946–2959, 2014, doi: 10.1109/TIE.2013.2286777.
- [6] C. Babetto, G. Bacco, and N. Bianchi, "Analytical Power Limits Curves of High-Speed Synchronous Reluctance Machines," *IEEE Trans Ind Appl*, vol. 55, no. 2, pp. 1342–1350, Mar. 2019, doi: 10.1109/TIA.2018.2875663.
- [7] B. Wang, J. Wang, B. Sen, A. Griffio, Z. Sun, and E. Chong, "A Fault-Tolerant Machine Drive Based on Permanent Magnet-Assisted Synchronous Reluctance Machine," *IEEE Trans Ind Appl*, vol. 54, no. 2, pp. 1349–1359, Mar. 2018, doi: 10.1109/TIA.2017.2781201.
- [8] C. Babetto and N. Bianchi, "Synchronous Reluctance Motor with Dual Three-Phase Winding for Fault-Tolerant Applications," *Proceedings - 2018 23rd International Conference on Electrical Machines, IECM 2018*, pp. 2297–2303, Oct. 2018, doi: 10.1109/ICELMACH.2018.8506771.
- [9] H. Heidari *et al.*, "A Review of Synchronous Reluctance Motor-Drive Advancements," *Sustainability 2021, Vol. 13, Page 729*, vol. 13, no. 2, p. 729, Jan. 2021, doi: 10.3390/SU13020729.
- [10] M. Villani, G. Fabri, A. Credo, L. Di Leonardo, and F. Parasiliti Collazzo, "Line-Start Synchronous Reluctance Motor: A Reduced Manufacturing Cost Avenue to Achieve IE4 Efficiency Class," *IEEE Access*, vol. 10, pp. 100094–100103, 2022, doi: 10.1109/ACCESS.2022.3208154.
- [11] N. G. Ozcelik, U. E. Dogru, M. Imeryuz, and L. T. Ergene, "Synchronous Reluctance Motor vs. Induction Motor at Low-Power Industrial Applications: Design and Comparison," *Energies 2019, Vol. 12, Page 2190*, vol. 12, no. 11, p. 2190, Jun. 2019, doi: 10.3390/EN12112190.
- [12] H. Heidari *et al.*, "A Review of Synchronous Reluctance Motor-Drive Advancements," *Sustainability*, vol. 13, no. 2, p. 729, Jan. 2021, doi: 10.3390/su13020729.
- [13] A. Fratta, G. P. Togli, A. Vagati, and F. Villata, "Ripple evaluation of high-performance synchronous reluctance machines," *IEEE Industry Applications Magazine*, vol. 1, no. 4, pp. 14–22, 1995, doi: 10.1109/2943.392459.



- [14] J. Liang, Y. Dong, H. Sun, R. Liu, and G. Zhu, "Flux-Barrier Design and Torque Performance Analysis of Synchronous Reluctance Motor with Low Torque Ripple," *Applied Sciences* 2022, Vol. 12, Page 3958, vol. 12, no. 8, p. 3958, Apr. 2022, doi: 10.3390/APP12083958.
- [15] W. Zhao, Y. Sun, J. Ji, Z. Ren, and X. Song, "Phase Shift Technique to Improve Torque of Synchronous Reluctance Machines with Dual M-Phase Windings," *IEEE Transactions on Industrial Electronics*, vol. 69, no. 1, pp. 5–17, Jan. 2022, doi: 10.1109/TIE.2021.3050359.
- [16] M. N. F. Ibrahim, A. S. Abdel-Khalik, E. M. Rashad, and P. Sergeant, "An Improved Torque Density Synchronous Reluctance Machine With a Combined Star-Delta Winding Layout," *IEEE Transactions on Energy Conversion*, vol. 33, no. 3, pp. 1015–1024, Sep. 2018, doi: 10.1109/TEC.2017.2782777.
- [17] N. Bianchi, S. Bolognani, D. Bon, and M. Dai Pr e, "Rotor flux-barrier design for torque ripple reduction in synchronous reluctance motors," *Conference Record - IAS Annual Meeting (IEEE Industry Applications Society)*, vol. 3, pp. 1193–1200, 2006, doi: 10.1109/IAS.2006.256683.
- [18] C. Gallardo, J. A. Tapia, M. Degano, H. Mahmoud, and A. E. Hoffer, "Rotor Asymmetry Impact on Synchronous Reluctance Machines Performance," *2022 International Conference on Electrical Machines, ICEM 2022*, pp. 848–854, 2022, doi: 10.1109/ICEM51905.2022.9910665.
- [19] J. K. Kostko, "Polyphase reaction synchronous motors," *Journal of the American Institute of Electrical Engineers*, vol. 42, no. 11, pp. 1162–1168, Nov. 2013, doi: 10.1109/joaiee.1923.6591529.
- [20] A. Vagati, "Synchronous reluctance solution: a new alternative in a.c. drives," in *IECON Proceedings (Industrial Electronics Conference)*, IEEE, 1994, pp. 1–13. doi: 10.1109/iecon.1994.397741.
- [21] L. Xu and J. Yao, "A compensated vector control scheme of a synchronous reluctance motor including saturation and iron losses," in *Conference Record of the 1991 IEEE Industry Applications Society Annual Meeting*, IEEE, 1992, pp. 298–304. doi: 10.1109/ias.1991.178170.
- [22] A. Vagati, M. Pastorelli, and G. Franceschini, "High-performance control of synchronous reluctance motors," *IEEE Trans Ind Appl*, vol. 33, no. 4, pp. 983–991, 1997, doi: 10.1109/28.605740.
- [23] R. E. Betz, R. Lagerquist, M. Jovanovic, T. J. E. Miller, and R. H. Middleton, "Control of synchronous reluctance machines," *IEEE Trans Ind Appl*, vol. 29, no. 6, pp. 1110–1122, 1993, doi: 10.1109/28.259721.
- [24] N. G. Ozcelik, U. E. Dogru, M. Imeryuz, and L. T. Ergene, "Synchronous reluctance motor vs. Induction motor at low-power industrial applications: Design and comparison," *Energies (Basel)*, vol. 12, no. 11, p. 2190, Jun. 2019, doi: 10.3390/en12112190.
- [25] T. A. Lipo, "Synchronous reluctance machines-a viable alternative for ac drives?," *Electric Machines and Power Systems*, vol. 19, no. 6, pp. 659–671, 1991, doi: 10.1080/07313569108909556.
- [26] X. D. Xue, K. W. E. Cheng, and N. C. Cheung, "Selection of electric motor drives for electric vehicles," *2008 Australasian Universities Power Engineering Conference, AUPEC 2008*, 2008, Accessed: Sep. 27, 2020. [Online]. Available: <https://ieeexplore.ieee.org/document/4813059>
- [27] R. R. Moghaddam, F. Magnussen, C. Sadarangani, and H. Lendenmann, "New theoretical approach to the synchronous reluctance machine behavior and performance," in *Proceedings of the 2008 International Conference on Electrical Machines, ICEM'08*, IEEE, Sep. 2008, pp. 1–6. doi: 10.1109/ICELMACH.2008.4799845.

- [28] D. A. Staton, T. J. E. Miller, and S. E. Wood, "Maximising the saliency ratio of the synchronous reluctance motor," *IEE Proceedings B: Electric Power Applications*, vol. 140, no. 4, pp. 249–259, Jul. 1993, doi: 10.1049/ip-b.1993.0031.
- [29] M. J. Kamper and A. F. Volschenk, "Effect of rotor dimensions and cross magnetisation on Ld and Lq inductances of reluctance synchronous machine with cageless flux barrier rotor," *IEE Proceedings: Electric Power Applications*, vol. 141, no. 4, pp. 213–220, Jul. 1994, doi: 10.1049/IP-EPA:19941261.
- [30] T. Matsuo and T. A. Lipo, "Rotor Design Optimization of Synchronous Reluctance Machine," *IEEE Transactions on Energy Conversion*, vol. 9, no. 2, pp. 359–365, Jun. 1994, doi: 10.1109/60.300136.
- [31] J. Ahn *et al.*, "Field weakening control of synchronous reluctance motor for electric power steering," *IET Electr Power Appl*, vol. 1, no. 4, p. 565, 2007, doi: 10.1049/iet-epa:20060212.
- [32] S. M. Ferdous, P. Garcia, M. A. M. Oninda, and A. Hoque, "MTPA and field weakening control of synchronous reluctance motor," *Proceedings of 9th International Conference on Electrical and Computer Engineering, ICECE 2016*, pp. 598–601, 2017, doi: 10.1109/ICECE.2016.7853991.
- [33] A. E. Hoffer, R. H. Moncada, B. J. Pavez, J. A. Tapia, and L. Laurila, "A high efficiency control strategy for synchronous reluctance generator including saturation," *Proceedings - 2016 22nd International Conference on Electrical Machines, ICEM 2016*, pp. 39–45, 2016, doi: 10.1109/ICELMACH.2016.7732503.
- [34] V. Manzolini, D. Da Ru, and S. Bolognani, "An Effective Flux Weakening Control of a SyRM Drive Including MTPV Operation," *IEEE Trans Ind Appl*, vol. 55, no. 3, pp. 2700–2709, 2019, doi: 10.1109/TIA.2018.2886328.
- [35] Y. Zhao, L. Ren, Z. Liao, and G. Lin, "A novel model predictive direct torque control method for improving steady-state performance of the synchronous reluctance motor," *Energies (Basel)*, vol. 14, no. 8, 2021, doi: 10.3390/en14082256.
- [36] E. M. Rashad, T. S. Radwan, and M. A. Rahman, "A maximum torque per ampere vector control strategy for synchronous reluctance motors considering saturation and iron losses," *Conference Record - IAS Annual Meeting (IEEE Industry Applications Society)*, vol. 4, pp. 2411–2417, 2004, doi: 10.1109/ias.2004.1348813.
- [37] R. Morales-Caporal and M. Pacas, "A predictive torque control for the synchronous reluctance machine taking into account the magnetic cross saturation," *IEEE Transactions on Industrial Electronics*, vol. 54, no. 2, pp. 1161–1167, Apr. 2007, doi: 10.1109/TIE.2007.891783.
- [38] D. Mingardi, M. Morandini, S. Bolognani, and N. Bianchi, "On the Properties of the Differential Cross-Saturation Inductance in Synchronous Machines," *IEEE Trans Ind Appl*, vol. 53, no. 2, pp. 991–1000, 2017, doi: 10.1109/TIA.2016.2622220.
- [39] S. Tahi and R. Ibtouen, "Finite element calculation of the dq-axes inductances and torque of synchronous reluctance motor," *2014 International Conference on Electrical Sciences and Technologies in Maghreb, CISTEM 2014*, pp. 1–5, 2014, doi: 10.1109/CISTEM.2014.7076979.
- [40] A. E. Hoffer, R. H. Moncada, B. J. Pavez, and J. A. Tapia, "A Novel Method for Finite-Element Modeling of a Commercial Synchronous Reluctance Machine," *IEEE Latin America Transactions*, vol. 16, no. 3, pp. 806–812, 2018, doi: 10.1109/TLA.2018.8358659.

- [41] Jorma. Haataja, "A comparative performance study of four-pole induction motors and synchronous reluctance motors in variable speed drives," 2003.
- [42] by Reza Rajabi Moghaddam, F. Magnussen, and C. Sadarangani, "Synchronous Reluctance Machine (SynRM) Design," 2007, Accessed: Feb. 08, 2023. [Online]. Available: <http://urn.kb.se/resolve?urn=urn:nbn:se:kth:diva-153663>
- [43] H. Shao, S. Li, and T. G. Habetler, "Analytical Calculation of the Air-gap Flux Density and Magnetizing Inductance of Synchronous Reluctance Machines," *2018 IEEE Energy Conversion Congress and Exposition, ECCE 2018*, pp. 5408–5413, 2018, doi: 10.1109/ECCE.2018.8558160.
- [44] M. Pohl and D. Gerling, "Analytical Model of Synchronous Reluctance Machines with Zhukovski Barriers," *Proceedings - 2018 23rd International Conference on Electrical Machines, ICEM 2018*, pp. 91–96, 2018, doi: 10.1109/ICELMACH.2018.8506737.
- [45] S. Cai, H. Hao, M. J. Jin, and J. X. Shen, "A Simplified Method to Analyze Synchronous Reluctance Machine," *2016 IEEE Vehicle Power and Propulsion Conference, VPPC 2016 - Proceedings*, Dec. 2016, doi: 10.1109/VPPC.2016.7791597.
- [46] N. Bianchi, S. Bolognani, D. Bon, and M. D. Pr e, "Torque harmonic compensation in a synchronous reluctance motor," *IEEE Transactions on Energy Conversion*, vol. 23, no. 2, pp. 466–473, Jun. 2008, doi: 10.1109/TEC.2007.914357.
- [47] H. Mahmoud, N. Bianchi, G. Bacco, and N. Chiodetto, "Nonlinear Analytical Computation of the Magnetic Field in Reluctance Synchronous Machines," *IEEE Trans Ind Appl*, vol. 53, no. 6, pp. 5373–5382, Nov. 2017, doi: 10.1109/TIA.2017.2746560.
- [48] M. Barcaro and N. Bianchi, "Air-gap flux density distortion and iron losses in anisotropic synchronous motors," *IEEE Trans Magn*, vol. 46, no. 1, pp. 121–126, Jan. 2010, doi: 10.1109/TMAG.2009.2030675.
- [49] G. Bacco and N. Bianchi, "Choice of flux-barriers position in synchronous reluctance machines," *2017 IEEE Energy Conversion Congress and Exposition, ECCE 2017*, vol. 2017-Janua, pp. 1872–1879, 2017, doi: 10.1109/ECCE.2017.8096023.
- [50] H. Mahmoud and N. Bianchi, "Eccentricity in Synchronous Reluctance Motors—Part II: Different Rotor Geometry and Stator Windings," *IEEE Transactions on Energy Conversion*, vol. 30, no. 2, pp. 754–760, Jun. 2015, doi: 10.1109/TEC.2014.2384534.
- [51] M. Degano, H. Mahmoud, N. Bianchi, and C. Gerada, "Synchronous reluctance machine analytical model optimization and validation through finite element analysis," *Proceedings - 2016 22nd International Conference on Electrical Machines, ICEM 2016*, pp. 585–591, 2016, doi: 10.1109/ICELMACH.2016.7732585.
- [52] X. Li, Y. Wang, and R. Qu, "Design of Synchronous Reluctance Motors with Asymmetrical Flux Barriers for Torque Ripple Reduction," in *2021 IEEE 4th Student Conference on Electric Machines and Systems (SCEMS)*, IEEE, Dec. 2021, pp. 1–6. doi: 10.1109/scems52239.2021.9646121.
- [53] C. Gallardo, J. A. Tapia, M. Degano, and H. Mahmoud, "Accurate Analytical Model for Synchronous Reluctance Machine With Multiple Flux Barriers Considering the Slotting Effect," *IEEE Trans Magn*, vol. 58, no. 9, Sep. 2022, doi: 10.1109/TMAG.2022.3189483.

- [54] K. C. Kim, "A novel method for minimization of cogging torque and torque ripple for interior permanent magnet synchronous motor," *IEEE Trans Magn*, vol. 50, no. 2, pp. 793–796, 2014, doi: 10.1109/TMAG.2013.2285234.
- [55] A. Credo, M. Villani, M. Popescu, and N. Riviere, "Application of Epoxy Resin in Synchronous Reluctance motors with fluid-shaped barriers for e mobility," *IEEE Trans Ind Appl*, vol. PP, no. c, pp. 1–1, 2021, doi: 10.1109/tia.2021.3103826.
- [56] X. Zeng, L. Quan, X. Zhu, L. Xu, and F. Liu, "Investigation of an asymmetrical rotor hybrid permanent magnet motor for approaching maximum output torque," *IEEE Transactions on Applied Superconductivity*, vol. 29, no. 2, pp. 1–4, 2019, doi: 10.1109/TASC.2019.2893708.
- [57] Y. Xiao, Z. Q. Zhu, J. T. Chen, D. Wu, and L. M. Gong, "A Novel Spoke-type Asymmetric Rotor Interior PM Machine," *ECCE 2020 - IEEE Energy Conversion Congress and Exposition*, pp. 4050–4057, 2020, doi: 10.1109/ECCE44975.2020.9236321.
- [58] I. Petrov, P. Ponomarev, and J. Pyrhönen, "Asymmetrical geometries in electrical machines," *International Review of Electrical Engineering*, vol. 11, no. 1, pp. 20–27, 2016, doi: 10.15866/iree.v11i1.7739.
- [59] A. E. Hoffer, I. Petrov, J. J. Pyrhonen, J. A. Tapia, and G. Bramerdorfer, "Analysis of a tooth-coil winding permanent-magnet synchronous machine with an unequal teeth width," *IEEE Access*, vol. 8, pp. 71512–71524, 2020, doi: 10.1109/ACCESS.2020.2987872.
- [60] X. Sun, G. Sizov, and M. Melfi, "Asymmetrical design in electrical machines," *2019 IEEE Energy Conversion Congress and Exposition, ECCE 2019*, pp. 3786–3792, 2019, doi: 10.1109/ECCE.2019.8913231.
- [61] D. M. Ionel, "Interior Permanent Magnet Motor Including Rotor With Flux Barriers," US8102091B2, 2008 [Online]. Available: <http://www.freepatentsonline.com/y2008/0224558.html>
- [62] K. M. Rahman, S. Jurkovic, E. L. Kaiser, and P. J. Savagian, "Interior permanent magnet machine with pole-to-pole asymmetry of rotor slot placement," US8933606B2, 2015 [Online]. Available: <https://patents.google.com/patent/US8933606B2/en>
- [63] D. Takizawa, "Electromagnetic steel sheet formed body, rotor core, rotor, rotating electrical machine, and vehicle," US8860276B2, 2014 [Online]. Available: <https://patents.google.com/patent/US8860276B2/en>
- [64] T. Suzuki, A. Maemura, Y. Kawazoe, Y. Fukuma, and T. Inoue, "Rotor, rotating electric machine, vehicle, elevator, fluid machine, and processing machine," US8227953B2, 2012 [Online]. Available: <https://patents.google.com/patent/US8227953B2/en>
- [65] W. Zhao, F. Xing, X. Wang, T. A. Lipo, and B. il Kwon, "Design and Analysis of a Novel PM-Assisted Synchronous Reluctance Machine with Axially Integrated Magnets by the Finite-Element Method," *IEEE Trans Magn*, vol. 53, no. 6, Jun. 2017, doi: 10.1109/TMAG.2017.2662717.
- [66] F. Xing, W. Zhao, and B. il Kwon, "Design and optimisation of a novel asymmetric rotor structure for a PM-assisted synchronous reluctance machine," *IET Electr Power Appl*, vol. 13, no. 5, pp. 573–580, 2019, doi: 10.1049/iet-epa.2018.0184.

- [67] A. J. Pina and L. Xu, "Modeling of synchronous reluctance motors aided by permanent magnets with asymmetric rotor poles," *Proceedings - 2015 IEEE International Electric Machines and Drives Conference, IEMDC 2015*, pp. 412–418, 2016, doi: 10.1109/IEMDC.2015.7409092.
- [68] G. Dajaku and D. Gerling, "New methods for reducing the cogging torque and torque ripples of PMSM," *2014 4th International Electric Drives Production Conference, EDPC 2014 - Proceedings*, pp. 1–7, 2014, doi: 10.1109/EDPC.2014.6984396.
- [69] W. Zhao, T. A. Lipo, and B. il Kwon, "Optimal design of a novel asymmetrical rotor structure to obtain torque and efficiency improvement in surface inset PM motors," *IEEE Trans Magn*, vol. 51, no. 3, pp. 3–6, 2015, doi: 10.1109/TMAG.2014.2362146.
- [70] W. Zhao, F. Zhao, T. A. Lipo, and B. il Kwon, "Optimal design of a novel v-type interior permanent magnet motor with assisted barriers for the improvement of torque characteristics," *IEEE Trans Magn*, vol. 50, no. 11, pp. 18–21, 2014, doi: 10.1109/TMAG.2014.2330339.
- [71] W. Zhao, D. Chen, T. A. Lipo, and B. il Kwon, "Performance Improvement of Ferrite-Assisted Synchronous Reluctance Machines Using Asymmetrical Rotor Configurations," *IEEE Trans Magn*, vol. 51, no. 11, Nov. 2015, doi: 10.1109/TMAG.2015.2436414.
- [72] Y. Fan, C. Tan, S. Chen, and M. Cheng, "Design and analysis of a new interior permanent magnet motor for EVs," in *2016 IEEE 8th International Power Electronics and Motion Control Conference, IPEMC-ECCE Asia 2016*, IEEE, May 2016, pp. 1357–1361. doi: 10.1109/IPEMC.2016.7512487.
- [73] E. Howard, M. J. Kamper, and S. Gerber, "Asymmetric Flux Barrier and Skew Design Optimization of Reluctance Synchronous Machines," *IEEE Trans Ind Appl*, vol. 51, no. 5, pp. 3751–3760, 2015, doi: 10.1109/TIA.2015.2429649.
- [74] M. Davoli, C. Bianchini, A. Torreggiani, and F. Immovilli, "A design method to reduce pulsating torque in PM assisted synchronous reluctance machines with asymmetry of rotor barriers," *IECON Proceedings (Industrial Electronics Conference)*, pp. 1566–1571, 2016, doi: 10.1109/IECON.2016.7793919.
- [75] M. Sanada, K. Hiramoto, S. Morimoto, and Y. Takeda, "Torque ripple improvement for synchronous reluctance motor using an asymmetric flux barrier arrangement," *IEEE Trans Ind Appl*, vol. 40, no. 4, pp. 1076–1082, 2004, doi: 10.1109/TIA.2004.830745.
- [76] S. Ferrari, E. Armando, and G. Pellegrino, "Torque Ripple Minimization of PM-assisted Synchronous Reluctance Machines via Asymmetric Rotor Poles," *2019 IEEE Energy Conversion Congress and Exposition, ECCE 2019*, pp. 4895–4902, Sep. 2019, doi: 10.1109/ECCE.2019.8912470.
- [77] A. Vagati, A. Canova, M. Chiampi, M. Pastorelli, and M. Repetto, "Design refinement of synchronous reluctance motors through finite-element analysis," *IEEE Trans Ind Appl*, vol. 36, no. 4, pp. 1094–1102, 2000, doi: 10.1109/28.855965.
- [78] X. B. Bomela and M. J. Kamper, "Effect of stator chording and rotor skewing on performance of reluctance synchronous machine," *IEEE Trans Ind Appl*, vol. 38, no. 1, pp. 91–100, Jan. 2002, doi: 10.1109/28.980362.
- [79] T. Hamiti, T. Lubin, and A. Rezzoug, "A simple and efficient tool for design analysis of synchronous reluctance motor," *IEEE Trans Magn*, vol. 44, no. 12, pp. 4648–4652, 2008, doi: 10.1109/TMAG.2008.2004536.

- [80] Y. Wang, D. M. Ionel, V. Rallabandi, M. Jiang, and S. J. Stretz, "Large-Scale Optimization of Synchronous Reluctance Machines Using CE-FEA and Differential Evolution," *IEEE Trans Ind Appl*, vol. 52, no. 6, pp. 4699–4709, Nov. 2016, doi: 10.1109/TIA.2016.2591498.
- [81] J. Juergens, A. Fricasse, L. Marengo, J. Gragger, M. de Gennaro, and B. Ponick, "Innovative design of an air cooled ferrite permanent magnet assisted synchronous reluctance machine for automotive traction application," *Proceedings - 2016 22nd International Conference on Electrical Machines, ICEM 2016*, pp. 803–810, Nov. 2016, doi: 10.1109/ICELMACH.2016.7732618.
- [82] B. Ban, S. Stipetic, and T. Jercic, "Minimum Set of Rotor Parameters for Synchronous Reluctance Machine and Improved Optimization Convergence via Forced Rotor Barrier Feasibility," *Energies 2021, Vol. 14, Page 2744*, vol. 14, no. 10, p. 2744, May 2021, doi: 10.3390/EN14102744.
- [83] N. Bernard, L. Dang, L. Moreau, and S. Bourguet, "A Pre-Sizing Method for Salient Pole Synchronous Reluctance Machines with Loss Minimization Control for a Small Urban Electrical Vehicle Considering the Driving Cycle," *Energies 2022, Vol. 15, Page 9110*, vol. 15, no. 23, p. 9110, Dec. 2022, doi: 10.3390/EN15239110.
- [84] B. Ban and S. Stipetic, "Systematic Metamodel-Based Optimization Study of Synchronous Reluctance Machine Rotor Barrier Topologies," *Machines 2022, Vol. 10, Page 712*, vol. 10, no. 8, p. 712, Aug. 2022, doi: 10.3390/MACHINES10080712.
- [85] N. Bianchi, S. Bolognani, D. Bon, and M. D. Pré, "Rotor flux-barrier design for torque ripple reduction in synchronous reluctance and PM-assisted synchronous reluctance motors," *IEEE Trans Ind Appl*, vol. 45, no. 3, pp. 921–928, 2009, doi: 10.1109/TIA.2009.2018960.
- [86] N. Bianchi, E. Fornasiero, E. Carraro, S. Bolognani, and M. Castiello, "Electric vehicle traction based on a PM assisted synchronous reluctance motor," *2014 IEEE International Electric Vehicle Conference, IEVC 2014*, 2014, doi: 10.1109/IEVC.2014.7056146.
- [87] P. Lazari, J. Wang, and B. Sen, "3-D Effects of Rotor Step-Skews in Permanent Magnet-Assisted Synchronous Reluctance Machines," *IEEE Trans Magn*, vol. 51, no. 11, Nov. 2015, doi: 10.1109/TMAG.2015.2446511.
- [88] M. Hofer and M. Schroedl, "Comparison of a flux barrier and a salient pole synchronous reluctance machine for high rotational speeds in electric traction applications," *2017 20th International Conference on Electrical Machines and Systems, ICEMS 2017*, Oct. 2017, doi: 10.1109/ICEMS.2017.8056108.
- [89] T. H. Lee, J. H. Lee, K. P. Yi, and D. K. Lim, "Optimal Design of a Synchronous Reluctance Motor Using a Genetic Topology Algorithm," *Processes 2021, Vol. 9, Page 1778*, vol. 9, no. 10, p. 1778, Oct. 2021, doi: 10.3390/PR9101778.
- [90] T. H. Lee, D. K. Lim, K. Y. Moon, and K. W. Jeon, "Topology Optimization Combined with a Parametric Algorithm for Industrial Synchronous Reluctance Motor Design," *Processes 2022, Vol. 10, Page 746*, vol. 10, no. 4, p. 746, Apr. 2022, doi: 10.3390/PR10040746.
- [91] J. C. Baziruwaha, M. J. Kamper, and S. Botha, "High Pole Number Epoxy-Casted Rotor Reluctance Synchronous Wind Generator," *2022 IEEE Energy Conversion Congress and Exposition, ECCE 2022*, 2022, doi: 10.1109/ECCE50734.2022.9948139.

- [92] T. Hubert, M. Reinlein, A. Kremser, and H. G. Herzog, "Torque ripple minimization of reluctance synchronous machines by continuous and discrete rotor skewing," *2015 5th International Conference on Electric Drives Production, EDPC 2015 - Proceedings*, Nov. 2015, doi: 10.1109/EDPC.2015.7323229.
- [93] O. Ocak and M. Aydin, "An Innovative Semi-FEA Based, Variable Magnet-Step-Skew to Minimize Cogging Torque and Torque Pulsations in Permanent Magnet Synchronous Motors," *IEEE Access*, vol. 8, pp. 210775–210783, 2020, doi: 10.1109/ACCESS.2020.3038340.
- [94] O. Korman, M. Degano, M. di Nardo, and C. Gerada, "A Novel Flux Barrier Parametrization for Synchronous Reluctance Machines," *IEEE Transactions on Energy Conversion*, vol. 8969, no. c, pp. 1–11, 2021, doi: 10.1109/TEC.2021.3099628.
- [95] M. S. Islam, A. Shrestha, and M. Islam, "Effect of Step Skew in Synchronous Reluctance Machines for High Performance Applications," *2022 IEEE Energy Conversion Congress and Exposition, ECCE 2022*, 2022, doi: 10.1109/ECCE50734.2022.9947850.
- [96] C. Gallardo, C. Madariaga, J. A. Tapia, and M. Degano, "A Method to Determine the Torque Ripple Harmonic Reduction in Skewed Synchronous Reluctance Machines," *Applied Sciences 2023, Vol. 13, Page 2949*, vol. 13, no. 5, p. 2949, Feb. 2023, doi: 10.3390/APP13052949.
- [97] A. Tessarolo, M. Degano, and N. Bianchi, "On the analytical estimation of the airgap field in synchronous reluctance machine," in *Proceedings - 2014 International Conference on Electrical Machines, ICEM 2014*, 2014, pp. 239–244. doi: 10.1109/ICELMACH.2014.6960187.
- [98] A. Tessarolo, M. Degano, and N. Bianchi, "On the analytical estimation of the airgap field in synchronous reluctance machine," *Proceedings - 2014 International Conference on Electrical Machines, ICEM 2014*, pp. 239–244, 2014, doi: 10.1109/ICELMACH.2014.6960187.
- [99] C. J. Fraser, "Electrical Machines," in *Systems, Controls, Embedded Systems, Energy, and Machines*, CRC Press, 2017, pp. 217–260. doi: 10.1201/9781420037043-13.
- [100] A. Tessarolo, "Modeling and analysis of synchronous reluctance machines with circular flux barriers through conformal mapping," *IEEE Trans Magn*, vol. 51, no. 4, pp. 1–11, Apr. 2015, doi: 10.1109/TMAG.2014.2363434.
- [101] B. Gaussens, E. Hoang, O. De La Barrière, J. Saint-Michel, M. Lecrivain, and M. Gabsi, "Analytical approach for air-gap modeling of field-excited flux-switching machine: No-load operation," *IEEE Trans Magn*, vol. 48, no. 9, pp. 2505–2517, 2012, doi: 10.1109/TMAG.2012.2196706.
- [102] N. Bianchi, M. Degano, and E. Fornasiero, "Sensitivity analysis of torque ripple reduction of synchronous reluctance and interior PM motors," *IEEE Trans Ind Appl*, vol. 51, no. 1, pp. 187–195, 2015, doi: 10.1109/TIA.2014.2327143.
- [103] A. Fratta, G. P. Troglia, A. Vagati, and F. Villata, "Evaluation of torque ripple in high performance synchronous reluctance machines," in *Conference Record - IAS Annual Meeting (IEEE Industry Applications Society)*, Publ by IEEE, 1993, pp. 163–170. doi: 10.1109/ias.1993.298919.
- [104] S. Taghavi and P. Pillay, "A Novel Grain-Oriented Lamination Rotor Core Assembly for a Synchronous Reluctance Traction Motor with a Reduced Torque Ripple Algorithm," *IEEE Trans Ind Appl*, vol. 52, no. 5, pp. 3729–3738, Sep. 2016, doi: 10.1109/TIA.2016.2558162.

- [105] T. Mohanarajah, J. Rizk, A. Hellany, M. Nagrial, and A. Klyavlin, "Torque Ripple Improvement in Synchronous Reluctance Machines," in *2018 2nd International Conference On Electrical Engineering, EECon 2018*, IEEE, 2018, pp. 44–50. doi: 10.1109/EECon.2018.8541021.
- [106] M. N. F. Ibrahim, P. Sergeant, and E. Rashad, "Simple design approach for low torque ripple and high output torque synchronous reluctance motors," *Energies (Basel)*, vol. 9, no. 11, p. 942, Nov. 2016, doi: 10.3390/en9110942.
- [107] E. S. Obe, "Calculation of inductances and torque of an axially laminated synchronous reluctance motor," *IET Electr Power Appl*, vol. 4, no. 9, pp. 783–792, 2010, doi: 10.1049/iet-epa.2009.0197.
- [108] S. Taghavi and P. Pillay, "A Sizing Methodology of the Synchronous Reluctance Motor for Traction Applications," *IEEE J Emerg Sel Top Power Electron*, vol. 2, no. 2, pp. 329–340, Jun. 2014, doi: 10.1109/JESTPE.2014.2299235.
- [109] G. Bacco and N. Bianchi, "Design Criteria of Flux-Barriers in Synchronous Reluctance Machines," *IEEE Trans Ind Appl*, vol. 55, no. 3, pp. 2490–2498, 2019, doi: 10.1109/TIA.2018.2886778.
- [110] G. Pellegrino, F. Cupertino, and C. Gerada, "Barriers shapes and minimum set of rotor parameters in the automated design of Synchronous Reluctance machines," *Proceedings of the 2013 IEEE International Electric Machines and Drives Conference, IEMDC 2013*, pp. 1204–1210, 2013, doi: 10.1109/IEMDC.2013.6556286.
- [111] F. Cupertino, G. Pellegrino, and C. Gerada, "Design of synchronous reluctance motors with multiobjective optimization algorithms," *IEEE Trans Ind Appl*, vol. 50, no. 6, pp. 3617–3627, Nov. 2014, doi: 10.1109/TIA.2014.2312540.
- [112] X. Liu, H. Chen, J. Zhao, and A. Belahcen, "Research on the Performances and Parameters of Interior PMSM Used for Electric Vehicles," *IEEE Transactions on Industrial Electronics*, vol. 63, no. 6, pp. 3533–3545, Jun. 2016, doi: 10.1109/TIE.2016.2524415.
- [113] K. Wang, Z. Q. Zhu, G. Ombach, M. Koch, S. Zhang, and J. Xu, "Optimal slot/pole and flux-barrier layer number combinations for synchronous reluctance machines," in *2013 8th International Conference and Exhibition on Ecological Vehicles and Renewable Energies, EVER 2013*, IEEE, Mar. 2013, pp. 1–8. doi: 10.1109/EVER.2013.6521583.
- [114] M. Fitouri, Y. Bensalem, and M. N. Abdelkrim, "Comparison between 2D and 3D Modeling of Permanent Magnet Synchronous Motor Using FEM Simulations," *Proceedings of the 17th International Multi-Conference on Systems, Signals and Devices, SSD 2020*, pp. 681–685, Jul. 2020, doi: 10.1109/SSD49366.2020.9364256.
- [115] H. Mahmoud, M. Degano, G. Bacco, N. Bianchi, and C. Gerada, "Synchronous Reluctance Motor Iron Losses: Analytical Model and Optimization," *2018 IEEE Energy Conversion Congress and Exposition, ECCE 2018*, pp. 1640–1647, Dec. 2018, doi: 10.1109/ECCE.2018.8558292.
- [116] K. Wang, Z. Q. Zhu, G. Ombach, M. Koch, S. Zhang, and J. Xu, "Optimal slot/pole and flux-barrier layer number combinations for synchronous reluctance machines," *2013 8th International Conference and Exhibition on Ecological Vehicles and Renewable Energies, EVER 2013*, 2013, doi: 10.1109/EVER.2013.6521583.



- [117] M. Degano *et al.*, "Optimised Design of Permanent Magnet Assisted Synchronous Reluctance Machines for Household Appliances," *IEEE Transactions on Energy Conversion*, 2021, doi: 10.1109/TEC.2021.3076675.
- [118] M. Barcaro, G. Meneghetti, and N. Bianchi, "Structural analysis of the interior PM rotor considering both static and fatigue loading," *IEEE Trans Ind Appl*, vol. 50, no. 1, pp. 253–260, 2014, doi: 10.1109/TIA.2013.2268048.